Acetate metabolism

in drug resistance and malignancy

of cancer

암의 약제 내성 및 악성도에서

아세테이트 대사 연구

2021년 2월

서울대학교 대학원

약학과 천연물과학전공

이 수 진

Acetate metabolism
in drug resistance and malignancy of cancer

암의 약제 내성 및 악성도에서
아세테이트 대사 연구

지도교수 박 성 혁

이 논문을 약학박사학위논문으로 제출함

2020년 12월

서울대학교 대학원
약학과 천연물과학전공
이 수 진

이 수 진의 박사학위논문을 인준함
2021년 1월

위 원 장 _____이 상 국_____ (인)

부위원장 _____노 민 수_____ (인)

위   원 _____홍 순 선_____ (인)

위   원 _____이 도 영_____ (인)

위   원 _____박 성 혁_____ (인)

Abstract

Acetate metabolism

in drug resistance and malignancy

of cancer

LEE SU JIN

Natural Products Science Major

College of Pharmacy

The Graduate School

Seoul National University

Acetate metabolism has become a popular topic in cancer research, as cancer metabolic dependence on acetate has been reported in relation to cancer bioenergy, macromolecular synthesis, and epigenetics. However, researches on the effects of acetate metabolism on acquired resistance to cancer drug and the changes in tumor grade are still lacking. Therefore, I investigated the metabolic characteristics of acetate with regards to cisplatin resistance in bladder cancer and the tumor grade of liver cancer, and the clinical significance of these characteristics.

First, with the recent recognition of lipid metabolic alterations in bladder cancers, I studied the metabolic implications of cisplatin resistance using cisplatin-sensitive (T24S) and resistant (T24R) bladder cancer cells. Real-time live metabolomics revealed that T24R cells consume more glucose, leading to a higher production of glucose-derived acetate and fatty acids. Along with the activation of general metabolic regulators, enzymes involved in acetate usage (ACSS2) and fatty acid synthesis (ACC), as well as a precursor for fatty acid synthesis (acetyl-CoA), were elevated in T24R cells. Consistently, metabolic analysis with ^{13}C isotope revealed that T24R cells preferred glucose to acetate as the exogenous carbon source for the increased fatty acid synthesis, in contrast to T24S cells. In addition, acetyl-CoA synthetase 2 (ACSS2), rather than the well-established ATP citrate lyase (ACLY), was the key enzyme supplying acetyl-CoA in T24R cells through glucose-derived endogenous acetate. The relevance of ACSS2 in cisplatin resistance was further confirmed by the abrogation of resistance by an ACSS2 inhibitor and, additionally, by the higher expression of ACSS2 in patient tissues with cisplatin resistance than tissues without resistance. Second, the relationships among acetate uptake, metabolic characteristics, and tumor malignancy were comprehensively studied in liver cancer. Among the cell lines used, HepG2 avidly utilized acetate, even in a glucose-sufficient environment, whereas Hep3B did not. These characteristics correlated with ACSS2 expression levels in the cells. Metabolomic isotope tracing showed high-ACSS2 HepG2 cells exhibited higher acetate incorporation and enhanced lipid anabolic metabolism than Hep3B cells, which was consistent with the separate gene expression profiles. These metabolic characteristics were confirmed by knockdown and inhibition studies of *ACSS2*, a master anabolic gene (*mTOR*), and a lipid

catabolic gene (*CPT1*). Upon in vivo ^{13}C isotopic tracing, orthotopic mouse liver tumors from HepG2 exhibited higher anabolism and less malignancy. Consistently, normal human liver tissue showed higher ACSS2 levels than cancerous tissues. Patients with lower ACSS2 expression, particularly those in the lower ~13th percentile (13VLA group), had notably poorer prognoses in the analysis of two independent large cohorts (total n = 486) than those with higher expression. The 13VLA patients also exhibited decreased lipid anabolic pathways, increased glycolysis, and enhanced hypoxia, which were associated with higher *ACSS2* promoter methylation. Finally, positron emission tomography-computed tomography (PET-CT) imaging of liver cancer patients showed that lower-grade cancer had higher ^{11}C-acetate but lower ^{18}F-FDG uptake, and this was reversed in higher-grade cancer. Overall, acetate uptake seems to be independent of nutrient depletion and contributes to lipid anabolic metabolism and better prognosis in liver cancer. This research can help to improve the treatment options for bladder and liver cancers and provide vulnerability targets for customized treatment.

Table of Contents

This appendix includes reprints of four published papers. I have participated as the first author for two of the papers, and as a co-first author for the other two. These works were done during my doctoral course in Seoul National University under my supervisor, Professor Sunghyouk Park.

List of Figures

List of Tables

1. General introduction

Metabolomics is the large-scale study of all metabolites involved in the chemical processes in cells, tissues, biofluids, or organisms [1]. While genomic and proteomic researches have steadily developed, the progress of metabolic research has been relatively stagnant [2]. However, more research is beginning to be conducted with the recent advancements in nuclear magnetic resonance (NMR) spectroscopy and mass spectrometry (MS) technologies, two major analysis techniques for the study of metabolomics [3, 4]. Biological systems are vast and complex, thus high-resolution, accurate, and sophisticated analysis methods are required [5]. With the advancement of technology, the application of non-radioactive isotope tracers to metabolomics has enabled individual tracking and pathway analyses, thereby broadening the scope of metabolic studies [6].

As metabolic research progresses, it is becoming clear that metabolites are not simply used for bioenergy but can also function as intracellular signaling molecules or gene regulators and are associated with some diseases [7]. In particular, metabolic research in the field of cancer began in earnest when Otto Warburg proposed the idea of aerobic glycolysis [8], which is a change in respiratory metabolism. Even in the presence of oxygen, cancer cells focus on glycolysis rather than oxidative phosphorylation [8]. In addition to enhancing glycolysis, cancer reprograms various metabolic pathways to acquire nutrients, synthesize macromolecules, and meet redox needs [9]. This cancer reprogramming is essentially accompanied by changes in metabolic enzymes and cancer-related gene expression and leads to cancer-specific metabolic profiles [10, 11]. These

characteristics of cancer cells, which are distinguishable from normal cells, can not only be used for the detection, diagnosis, prognosis, etc., of cancer but also as direct targets for treatment [12].

The major nutrients required for cancer metabolism include glucose, acetate, glutamine, and fatty acids [13]. Acetate, in particular, is activated as acetyl-CoA and functions as a basic unit for energy metabolism and biosynthesis [14, 15]. In the 1950s, Sidney Weinhouse proposed the opposite relationship between cancer formation and acetate metabolism, suggesting that when normal liver tissues become cancerous, fatty acids are not effectively produced from acetate [16]. In recent years, there have been reports of cancer cell dependence on acetate metabolism. Since acetyl-CoA is supplied by acetate through the ACSS2 enzyme, tumor size is affected by the expression of ACSS2 [17]. In addition, functional genomics studies have shown that the activity of ACSS2 contributes to cancer cell growth in hypoxia and nutrient-depleted conditions in breast and prostate cancers [18]. Liver cancer has also been reported to cause de novo lipid synthesis by increasing the expression of ACACA and FASN under hypoxia, and ACSS2 is known to be related to FASN expression [19]. Various studies to date have shown there is an association between cancer and acetate metabolism, but the research models and tools were different, which has led to controversies, and an definite conclusion has not been reached [20]. In addition, because of the lack of metabolic studies taking cancer drug resistance acquisition and the differences among tumor grades into account, the application of acetate metabolism in cancer treatment has been limited. Therefore, an integrated study on cancer metabolism that considers the changing process in cancer will provide the basis for developing customized treatments for cancer patients.

2. Part I

Glucose-derived acetate and ACSS2 as key players

in cisplatin resistance in bladder cancer

I. Introduction

Bladder cancer (BC) usually arises in the bladder epithelial lining and is the seventh most common cancer of men worldwide [21-23]. The majority of BC cases (~90%) are classified as transitional cell carcinoma (TCC), which can be further categorized into non-muscle-invasive BC (NMIBC) or muscle-invasive BC (MIBC) according to the extent of invasion into the muscular layer. NMIBC exhibits better prognoses and survival rates, but about 20% of NMIBC patients progress to MIBC [24, 25]. Radical cystectomy is the standard treatment for MIBC; however, within two years after treatment, approximately 50% of patients develop distant metastases. For metastatic BC, cisplatin-based chemotherapy with or without radiotherapy is the current gold standard, and those who do not respond well to this treatment generally have a poor prognosis [26].

It is well established that cisplatin kills rapidly proliferating cancer cells, mostly through DNA damage [27]. Cisplatin generates intra- and inter-strand purine crosslinks that interfere with DNA replication, eventually leading to apoptosis. The toxicity mechanism, especially in the kidney, has also been reported to involve the generation of reactive oxygen species (ROS) and oxidative stress [28]. However, the

biochemical processes underlying resistance to cisplatin are complex and may involve various signaling pathways, such as p53, PI3K/AKT, and ROS detoxification [29]. The contributions of these individual mechanisms may differ according to the particular types of tumors involved.

Recent study results suggested that not only these well-established cell-signaling mechanisms but also metabolic activities are involved in cisplatin-induced cell death [30]. For example, differences in the succinate-dehydrogenase-mediated production of NADPH may be responsible for the pharmacometabonomic heterogeneity of cisplatin-induced kidney toxicity [31]. In addition, levels of UDP-GlcNAc, the metabolite involved in N-acetylglucosamine glycosylation, were shown to correlate with the cisplatin sensitivity of cancer cells [32]. As metabolism is increasingly recognized as being involved in cancer initiation and progression [33], the metabolic study of cisplatin resistance may lead to improvements in therapies for refractory BC.

Among the key metabolites that fuel cancer cell proliferation, acetate has not drawn as much attention as glucose and glutamine [14]. Recent studies, however, have found acetate to be a key substrate for cancer bioenergetics and macromolecular synthesis [15, 17]. In addition, the increased usage of ^{11}C-acetate positron emission tomography in clinics has provided proof-of-concept evidence for the importance of acetate metabolism in cancer [34]. At the heart of acetate's involvement in cancer pathology is the enzyme ACSS2, which is responsible for converting acetate to acetyl-CoA. The production of acetyl-CoA is critical for the upkeep of fatty acid synthesis in cancer cells [14]. Fatty acid metabolism is a critical aspect of cancer metabolism, as the proliferation of cancer cells requires a large amount of biomass.

4

Interestingly, BC may also have altered lipid or fatty acid metabolism [35-38]. Despite the interesting connections among acetate, fatty acid, and cancer metabolism, the exact source of acetate in cancer cells remains debatable, as the concentration of acetate in the blood is low.

In this study, I employed real-time live metabolomics in the identification of metabolic reprogramming in cisplatin-resistant BC cells and verified the results in patient-derived tissues. I aimed to investigate aspects of acquired chemoresistance and potential vulnerabilities that can be exploited to overcome the resistance.

II. Materials and methods

1. Chemicals and reagents

The stable isotope-labeled D-Glucose (U-$^{13}C_6$, 99%) and acetate (1,2-$^{13}C_2$, 99%) were purchased from Cambridge Isotope Laboratories (Andover, MA, USA). The standard compounds, including pyruvate, lactate, alanine, acetate, succinate, glucose, palmitate, glycine, glutamate, isoleucine, valine, leucine, and glutathione (reduced) were obtained from Sigma-Aldrich (St. Louis, MO, USA). The ACSS2 inhibitor, 1-(2,3-di(thiophen-2-yl)quinoxalin-6-yl)-3-(2-methoxyethyl)urea, was purchased from ChemBridge (San Diego, CA, USA), and the ACLY inhibitor, 3,5-dichloro-2-hydroxy-N-(4-methoxy-[1,1'-biphenyl]-3-yl)-benzenesulfonamide (BMS-303141), was purchased from Bio-Techne (Minneapolis, MN, USA). The following antibodies, β-actin antibody (A1978, 1:5000) from Sigma-Aldrich (St. Louis, MO, USA), ACSS2 antibody (PA5-52059, 1:1000) from Thermo Fisher Scientific (Waltham, MA, USA), were used. All other antibodies, ACC (3676, 1:750), FAS (3180, 1:750), EGFR (2232; 1:1000), phospho-EGFR (Tyr1068) (3777; 1:1000), Src (2108; 1:750), phospho-Src (Tyr527) (2105; 1:1000), mTOR (2983; 1:1000), phospho-mTOR (Ser2448) (5536; 1:1000), and horseradish peroxidase (HRP) conjugated secondary antibodies (7074, 1:1000; 7076, 1:1000) were obtained from Cell Signaling Technology (Danvers, MA, USA).

2. Cell culture and biochemical assays

T24S and T24R urothelial carcinoma cells were cultured in DMEM supplemented with 10% fetal bovine serum (FBS), 2 mM L-glutamine, and 1% antibiotic solution (all from Invitrogen, Carlsbad, CA, USA). All cells were maintained in a humidified incubator (37°C and 5% CO_2). Cisplatin-resistant bladder cancer cells (T24R) were obtained through chronic treatments of cisplatin at low doses over six months [39, 40]. Briefly, the final cell viability was $\leq$ 40% for T24S cells and nearly 100% for T24R cells upon 10 μM cisplatin treatment for 12 h. Cell viability assay was performed using MTS (Promega, Inc., Madison, WI) according to the manufacturer's protocol. Western blot analysis was performed following routine procedures with β-actin as normalization control.

3. Sample preparation for live NMR metabolomics

Six plates (100 mm) of 70% confluent cultured cells were harvested with centrifugation. After the re-suspension of the cells with 5 mL DPBS, cells were counted, and 3×10^7 cells were moved into a new tube. After centrifugation, the harvested cells were re-suspended with 500 μl glucose-free DMEM (Gibco, Grand Island, NY, USA) supplemented with 10% dialyzed FBS (Welgene, Daegu, Korea), 25 mM $^{13}C_6$-labeled glucose, and 10% D_2O. The cells were spun in an NMR tube with a weak centrifugal force (30 g for 100 s) to allow sedimentation, enough to cover the active region of the NMR detection coil. The NMR tubes with the cells were inserted into NMR magnet and the spectra were acquired as usual.

4. Isotope incorporation analysis for fatty acids

The T24S and T24R cells were counted (5×10^6) and seeded in 6-well plates. After 24 h adaptation, cells were treated with glucose-free DMEM supplemented with 10% dialyzed FBS, and 5 mM non-labeled glucose. For the ^{13}C-acetate and ^{13}C-glucose treatment, 0.5 mM 1,2-^{13}C$_2$-acetate and 20 mM U-^{13}C$_6$-glucose was added, respectively. For the inhibitor treatment, the ACSS2 inhibitor (15.6 μM) and the ACLY inhibitor (32 μM) were also added to the cell media. After a 24 h treatment, the fatty acids were extracted from the counted (9.05×10^6) cells using the two-layer methanol-chloroform extraction method as previously described [41].

5. NMR measurement

^{1}H-^{13}C Heteronuclear Single Quantum Coherence (HSQC) NMR spectra were measured on an 800 MHz Bruker Avance spectrometer (Bruker BioSpin, Billerica, MA, USA) equipped with a cryogenic triple resonance probe at Seoul National University, Korea. The dataset comprises 1024×128 points for the direct and indirect dimensions, respectively. The time course spectral measurement was obtained at 310 K for 24 time-points, with each experiment lasting for 288 sec. Each of the metabolites was identified by spiking the standard compounds. Metabolites were quantified as described previously [42]. Non-uniform sampling (NUS) HSQC data were obtained as described previously [43].

6. Quantification of acetyl-CoA

The levels of acetyl-CoA were measured from cell lysates using PicoProbe™ Acetyl-CoA Assay Kit (BioVision, Milpitas, CA, USA), following the protocol provided by the manufacturer. Briefly, free CoA was quenched, and then Acetyl-CoA was converted to CoA. The CoA was then reacted to form a reduced nicotinamide adenine dinucleotide (NADH), which interacts with PicoProbe, resulting in the fluorescence. The reading was done with Ex = 535 / Em = 587 nm.

7. Immunohistochemistry (IHC) analysis

To stain the slides of bladder tumor tissues obtained from BC patients showing complete remission (CR) or progressive disease (PD), the ACSS2 antibody (1:100, LifeSpan Biosciences, Inc, Seattle, WA) was utilized. A high pH was used for the antigen retrieval and an Ultraview DAB Detection Kit from Ventana Medical Systems was used for counterstaining. To acquire the digital images, stained slides were scanned using an Aperio Turbo Scanscope AT machine (Leica Biosystems, Wetzlar, Germany). High-resolution images of each slide were uploaded onto the Leica Biosystems cloud drive for further annotations and analysis. Digitized images were analyzed with the Tissue IA Optimiser (Leica Biosystems, Wetzlar, Germany) software installed on the Leica Digital Image Hub. Following pathological annotations, the Measure Stained Cells Algorithm option on the Leica Tissue IA software was used. Each annotated slide had a minimum threshold of 100,000 cells to be analyzed. After analysis, data for the nuclear h-score, % of positive nuclei, and % of positive nuclear area in tissue were collected and used for comparative graphing.

8. Routine statistics

All functional validation experiments were repeated at least three times. Data were compared using Student's *t*-tests. $P < 0.05$ was considered to be statistically significant.

III. Results

A. Live metabolomic comparison between cisplatin-sensitive and -resistant BC cells

Several metabolomics studies have shown that BCs may have abnormalities in the metabolites involved in lipid usage [35, 38]. Furthermore, perturbed metabolism has been implicated in cancer drug resistance and cancer aggressiveness or progression [44]. I hypothesized that there are differences in metabolism and metabolism-associated pathways between cisplatin-sensitive and -resistant BC cells. To test this, I applied live metabolomics approach [41] to the isogenic BC cell lines, T24S (cisplatin-sensitive) and T24R (cisplatin-resistant) [39]. The metabolites generated from ^{13}C-glucose tracer were monitored with 2D ^{1}H-^{13}C heteronuclear single quantum coherence (HSQC) NMR in real-time (Fig. 1A and B). By spiking the spectra with standard compounds, I obtained the peak assignments for those with significant changes (Table 1). Along with the peaks for the metabolites involved in glycolysis, pyruvate metabolism, and the TCA cycle, I readily identified those corresponding to fatty acids. This was possible through the live metabolomics method, as lipid-soluble fatty acids and water-soluble polar metabolites are not usually quantifiable in a single analysis with conventional cell lysate metabolomics [43].
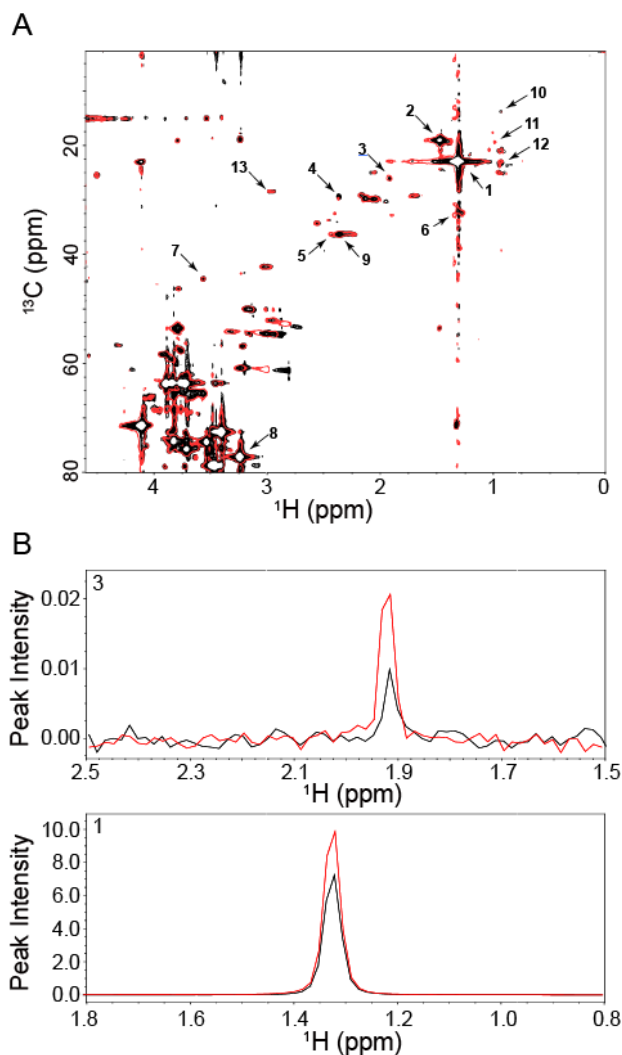
Figure 1. Live NMR metabolomic comparison between cisplatin-sensitive and -resistant cells

(A) The first (black) and last (red) spectra obtained from cisplatin-sensitive (T24S) cancer cells over 1 h 56 min after the addition of $^{13}C_6$-glucose. (1: lactate, 2: alanine, 3: acetate, 4: pyruvate, 5: succinate, 6: fatty acid, 7: glycine, 8: glucose, 9: glutamate, 10: isoleucine, 11: valine, 12: leucine, 13: glutathione (reduced); see Table 1). Assignments were obtained by spiking with standard compounds. (B) One-dimensional spectra for two compounds were extracted for comparison (1 and 3).

12

No.	METABOLITE	^{1}H	^{13}C
1	Lactate	1.32	22.9
2	Alanine	1.48	19.0
3	Acetate	1.92	26.1
4	Pyruvate	2.37	29.3
5	Succinate	2.43	36.3
6	Fatty acid	1.31	32.1
7	Glycine	3.56	44.5
8	Glucose	3.25	77.0
9	Glutamate	2.36	36.3
10	Isoleucine	0.93	13.8
11	Valine	0.99	19.4
12	Leucine	0.94	22.9
13	Glutathione (reduced)	2.97	28.3

Table 1. Metabolites identified by spiking with standard compounds

The signal numbers (see Fig. 1A) and chemical shifts are indicated.

B. Cisplatin resistance may be linked to increased glucose consumption and acetate production

The time-dependent changes in these metabolites revealed that T24R cells exhibited specific metabolic characteristics distinct from T24S cells. Glucose consumption was greater in T24R cells, indicating a higher rate of glycolysis (Fig. 2A). The levels of pyruvate, the last glycolytic metabolite prior to the TCA cycle, became almost equal in the two cell types immediately after an initial brief period of increased consumption in the T24R cells (Fig. 2B). Lactate, alanine, and acetate all exhibited net production in both cells, but there was an intriguing difference. T24S cells accumulated lactate and alanine faster and to higher levels compared with T24R cells (Fig. 2C and D), while T24R cells accumulated acetate much faster and maintained much higher levels throughout (Fig. 2E). In addition, despite the greater consumption of glucose in T24R cells, lactate production was significantly lower (Fig. 2C). These findings suggest that the preferred metabolic route for the increased glucose consumption in T24R cells is not lactate formation, as occurs in Warburg-type metabolism; rather, it may be other metabolites generated through acetate. One possible destination may be fatty acids because fatty acid levels were also higher in T24R cells, as estimated by their mid-chain CH_2 peak intensities (Fig. 2F). There were no significant differences between the two cell types for the metabolites glycine, a possible indicator of one-carbon metabolism, or glutamate, an important anaplerotic metabolite in TCA (Fig. 2G and H).
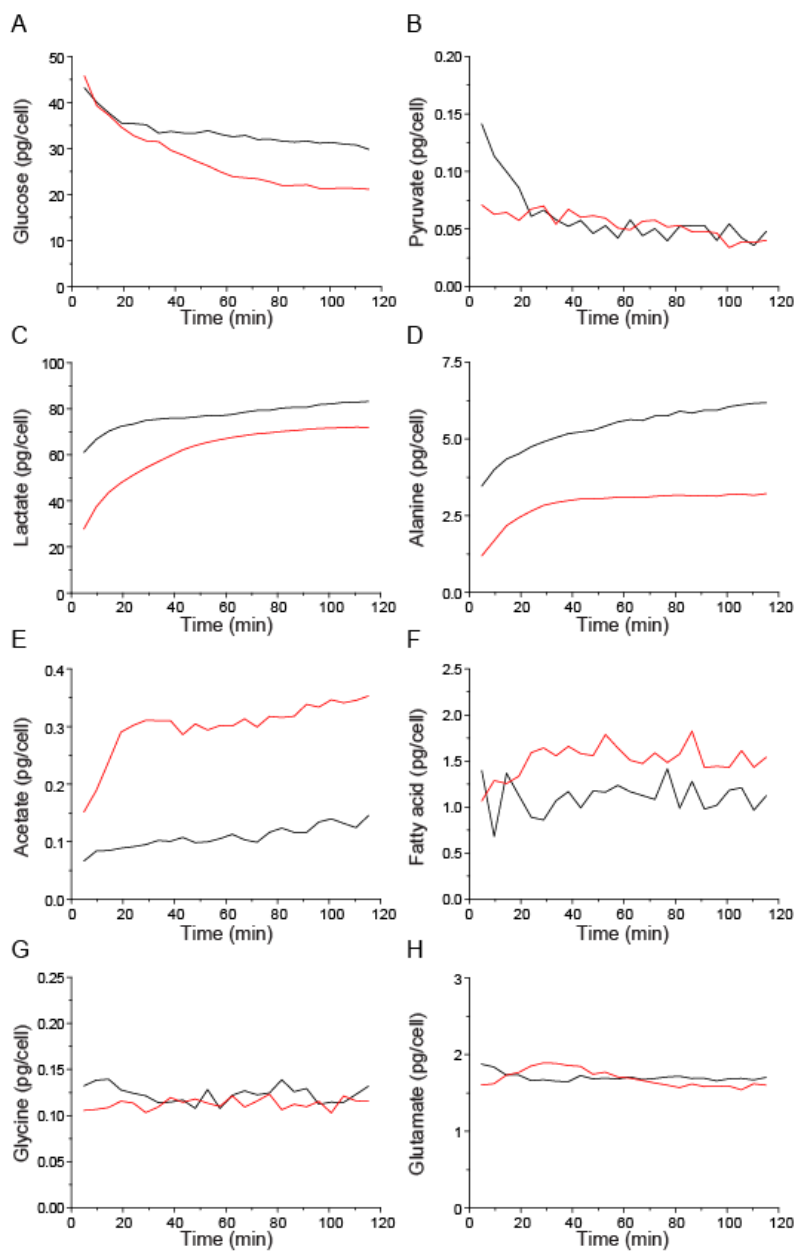
Figure 2. Time-dependent metabolic changes between cisplatin-sensitive and -resistant cells

(A through H) Time-dependent metabolic changes between T24S (black) and T24R (red) cells were obtained in real-time with a live NMR metabolomics approach. The metabolites were quantified as described previously [41].

C. Two-carbon pathway involving acetate that leads to fatty acid synthesis is enhanced in cisplatin-resistant T24 cells

I noted the differential patterns of changes in acetate levels compared with lactate and alanine levels between the T24S and T24R cells. These three metabolites downstream from pyruvate exhibited similar changes in previous live metabolomics studies with liver cells [41]. Lactate and alanine retain all three carbons from pyruvate, whereas acetate is formed through the loss of one carbon from pyruvate. With these unique characteristics of acetate and the higher ^{13}C-fatty acid levels in T24R cells, I hypothesized that there might be alterations in the pathways of fatty acid metabolism involving acetate. To test this hypothesis, I first looked at the levels of upstream signaling molecules that can affect fatty acid metabolism. A significant increase in phosphorylated EGFR and mTOR in T24R, without much increase in their total levels, suggested that cisplatin resistance is associated with the activation of upstream metabolic regulators (Fig. 3A). When I examined further downstream enzymes, I found that acetyl-CoA carboxylase (ACC), a key enzyme synthesizing malonyl-CoA from acetyl-CoA, is expressed at much higher levels in T24R than T24S cells (Fig. 3B). Malonyl-CoA is a direct substrate of fatty acid synthase (FAS), which was present at similar levels in both cells (Fig. 3B). To investigate the involvement of acetate in fatty acid synthesis, I measured the levels of ACSS2, as it is a key enzyme in pathways incorporating acetate into fatty acids. The ACSS2 levels were much higher in T24R cells (Fig. 3C), and this was corroborated by the higher level of acetyl-CoA generated from acetate by ACSS2 (Fig. 3D). Given that ACC and ACSS2 are two major enzymes that incorporate acetate into fatty acids, my results suggest that T24R may have enhanced fatty acid synthesis via two-carbon

metabolism involving acetate.
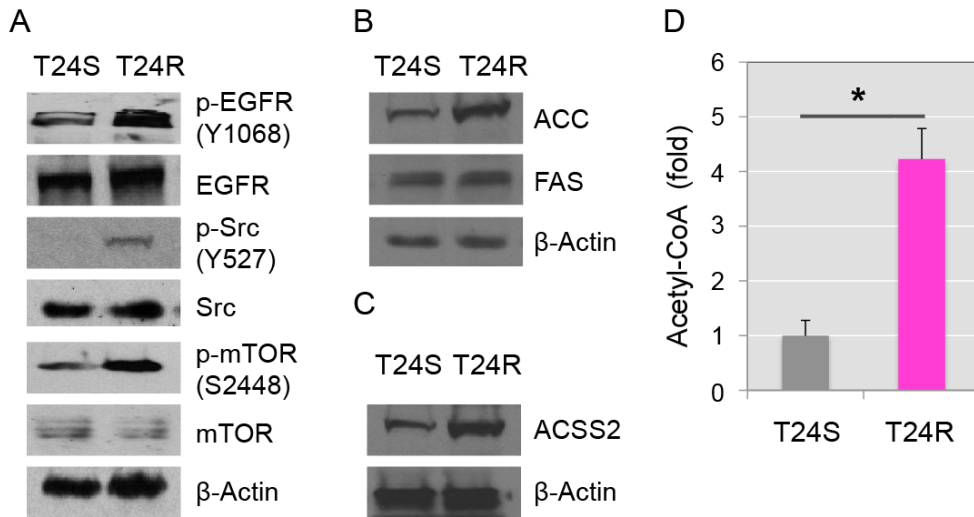
Figure 3. Expression levels of metabolic regulators and enzymes in T24S and T24R cells

Western blot analysis of (A) upstream regulators of metabolism (EGFR, Src, and mTOR) and their phosphorylated forms, (B) acetyl-CoA carboxylase (ACC) and fatty acid synthase (FAS) involved in fatty acid synthesis, and (C) acetyl-CoA synthetase 2 (ACSS2) for acetate utilization in T24S and T24R cells. The expression levels of β-actin were used as a control for western blot analysis. (D) Acetyl-CoA levels were measured as described in the method section. Statistical analysis was performed using Student's t-test, and the asterisk indicates $p < 0.05$. The error bars represent the standard deviation (N = 5).

D. Glucose-derived endogenous acetate contributes to enhanced de novo fatty acid synthesis in T24R cells

Metabolic flux through a particular step can increase significantly, even when enzyme levels are constant, providing there is an increased supply of substrate. I observed the activation of acetate-involving two-carbon metabolism leading to the FAS step in T24R cells, despite T24S and T24R cells having similar FAS levels (Fig. 3B). Therefore, I tested if there was a corresponding increase in de novo fatty acid synthesis and its correlation with the activation of acetate-involving two-carbon metabolism in T24R cells. De novo fatty acid synthesis was assessed by measuring the signal for the splitting of the omega methyl carbon arising from ^{13}C-^{13}C coupling in the HSQC spectra using a ^{13}C-glucose tracer. This is possible because ^{13}C labels from a glucose-derived two-carbon unit are incorporated into the omega methyl group during de novo fatty acid synthesis (Fig. 4A). In comparison, fatty acid chain elongation of a pre-existing fatty acyl chain occurs only at the carboxyl-terminal end. The intensities of the splitting doublet of the omega methyl group of fatty acids, derived from the tracer glucose, were much higher in T24R (Fig. 4B), indicating elevated de novo fatty acid synthesis from glucose in these cells. This finding, combined with the increased acetate production from glucose and higher levels of ACSS2, ACC, and acetyl-CoA, indicates that an acetate-involving two-carbon unit from glucose contributes to the enhanced fatty acid synthesis in T24R cells.

Because previous studies have emphasized the roles of blood-borne exogenous acetate, rather than glucose-derived endogenous acetate, in bioenergetics and lipid biosynthesis [15, 17], I also investigated de novo fatty acid synthesis from exogenous ^{13}C-acetate added to the medium. The incorporation of acetate into the

terminal methyl was much lower in T24R cells, indicating that exogenous acetate is not a major source for the increased de novo fatty acid synthesis in these cells (Fig. 4C). The lower production of glucose-derived fatty acids in T24S cells is also consistent with the higher excretion of lactate from glucose (Fig. 5). By comparison, the higher consumption of glucose in T24R cells may contribute to the higher de novo fatty acid synthesis through acetate production.
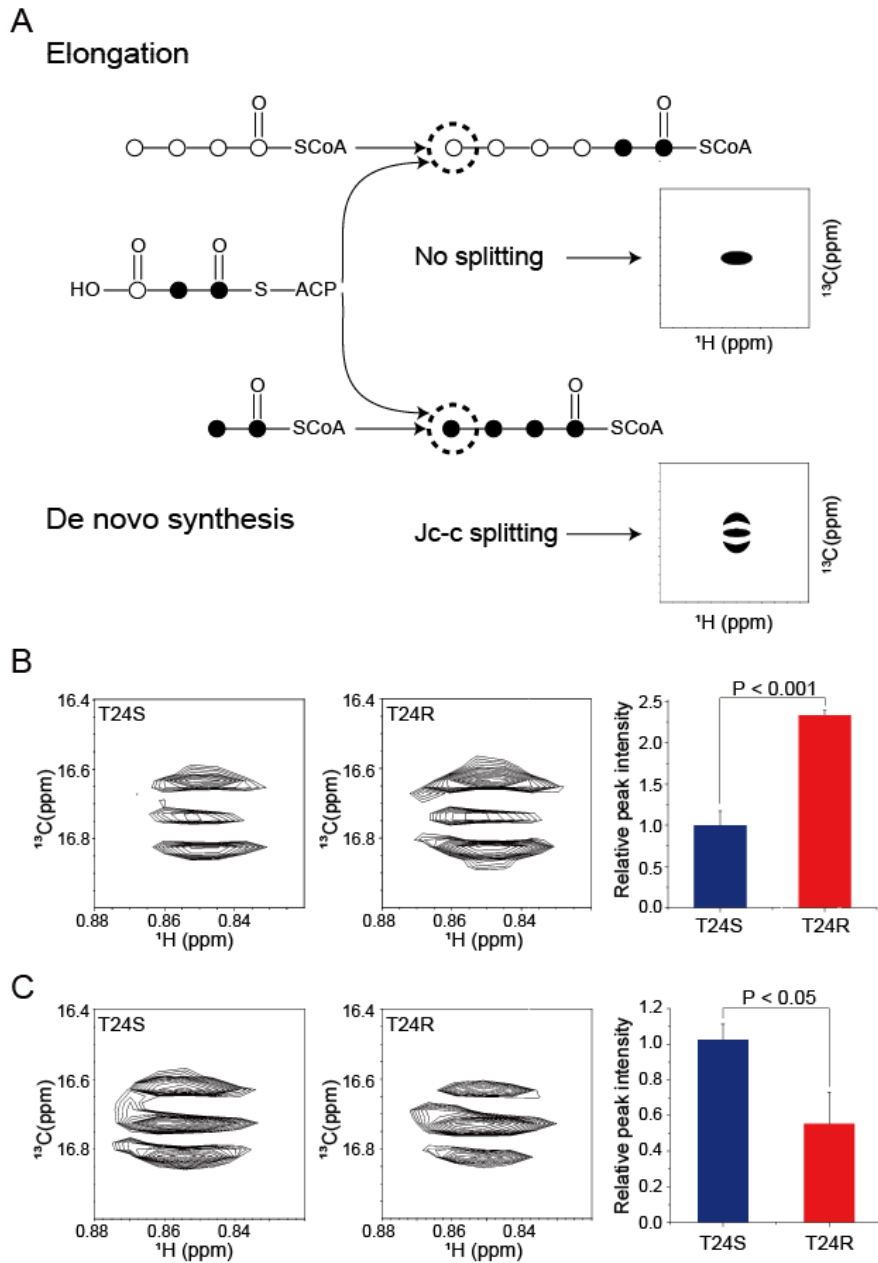
Figure 4. De novo fatty acid synthesis from glucose and acetate

(A) Schematic representation of NMR signal splitting patterns by ^{13}C-acetyl-CoA

for fatty acid elongation and de novo synthesis steps. Filled circles represent ^{13}C

isotopes and open circles represent unlabeled carbons. (B) Incorporation of ^{13}C

isotope into the omega position of the fatty acid alkyl chain with U-^{13}C$_6$-glucose. Left and middle, NUS HSQC spectra for the omega carbon in fatty acid alkyl chains from T24S and T24R cells, respectively. Right, the peak areas for the doublet of the omega carbon from the spectra. The peak areas were normalized to the number of harvested cells. (C) Incorporation of ^{13}C isotope as in (B) with U-^{13}C$_6$-acetate. T24S and T24R cells were cultured in media containing 5 mM non-labeled glucose supplemented with 20 mM ^{13}C-glucose (B) or 0.5 mM ^{13}C-acetate (C) for 24 h. Statistical analysis of data from three independent experiments was performed using the Student's *t*-test, and the resulting P-values are indicated. The error bars represent the standard deviation. Abbreviations: coenzyme A (CoA), acyl carrier protein (ACP).
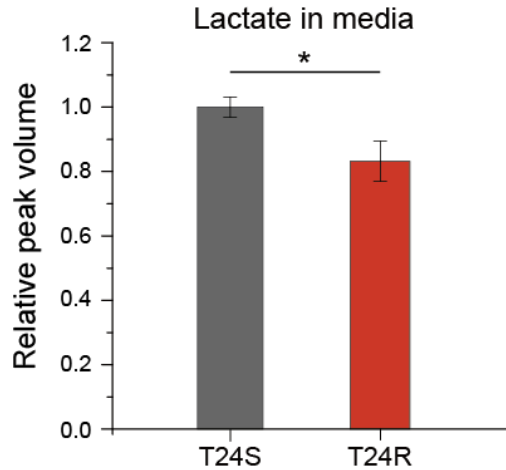
Figure 5. Lactate excreted by T24S and T24R cells

Lactate levels in T24S and T24R cell culture media were evaluated by NMR peak volumes. The cells were cultured in DMEM for 24 h. The cultured media were mixed with extraction solvent (methanol-acetonitrile-distilled water), dried, and resuspended in NMR buffer. 1D ^{1}H NMR data were obtained, and the peak volumes were measured with Bruker-provided Topspin software. Statistical analysis was performed using Student's *t*-test, and the asterisk indicates p < 0.05. The error bars represent the standard deviation.

E. ACSS2 inhibition decreases fatty acid synthesis and cell viability of T24R cells

The above data suggest a possible link between glucose and fatty acid synthesis through endogenous acetate derive from glucose; therefore, I aimed to obtain further details of the pathways. Theoretically, a glucose-derived two-carbon unit can be incorporated into fatty acids either via acetate or citrate, with the former mediated by ACSS2 and the latter by ACLY (Fig. 6A). The ACLY-mediated pathway is considered the major pathway for fatty acid synthesis in various cancers [45]; whereas the ACSS2-mediated pathway, which uses glucose-derived endogenous acetate, has been explored very little. Therefore, I selectively inhibited the two pathways using specific inhibitors and measured the de novo fatty acid synthesis with NMR as described above.

Inhibition of the ACSS2 pathway by 1-(2,3-di(thiophen-2-yl)quinoxalin-6-yl)-3-(2-methoxyethyl)urea decreased the de novo synthesis of fatty acids in T24R cells by more than 60%, whereas no significant change was observed in T24S cells (Fig. 6B). In contrast, ACLY inhibition by BMS-303141 led to a significant decrease in de novo synthesis in T24S cells but not in T24R cells. Importantly, the same ACSS2 inhibitor led to inhibition of the growth of T24R cells under cisplatin-resistance conditions (Fig. 6C). I did not add any acetate to the medium; therefore, these results confirm that the incorporation of glucose-derived endogenous acetate into fatty acids via ACSS2 is important in the cisplatin-resistance phenotype of T24R cells. I obtained further consistent data using an siRNA approach. ACSS2 siRNA treatment of T24R cells induced a substantial decrease in acetyl-CoA, whereas the levels did not change with ACLY siRNA treatment (Fig. 7A). The data also show

24

that ACSS1 has a much more minor role in acetyl-CoA production in T24R cells. Furthermore, ACLY siRNA induced a larger decrease in fatty acid synthesis in T24S than T24R cells (Fig. 7B).
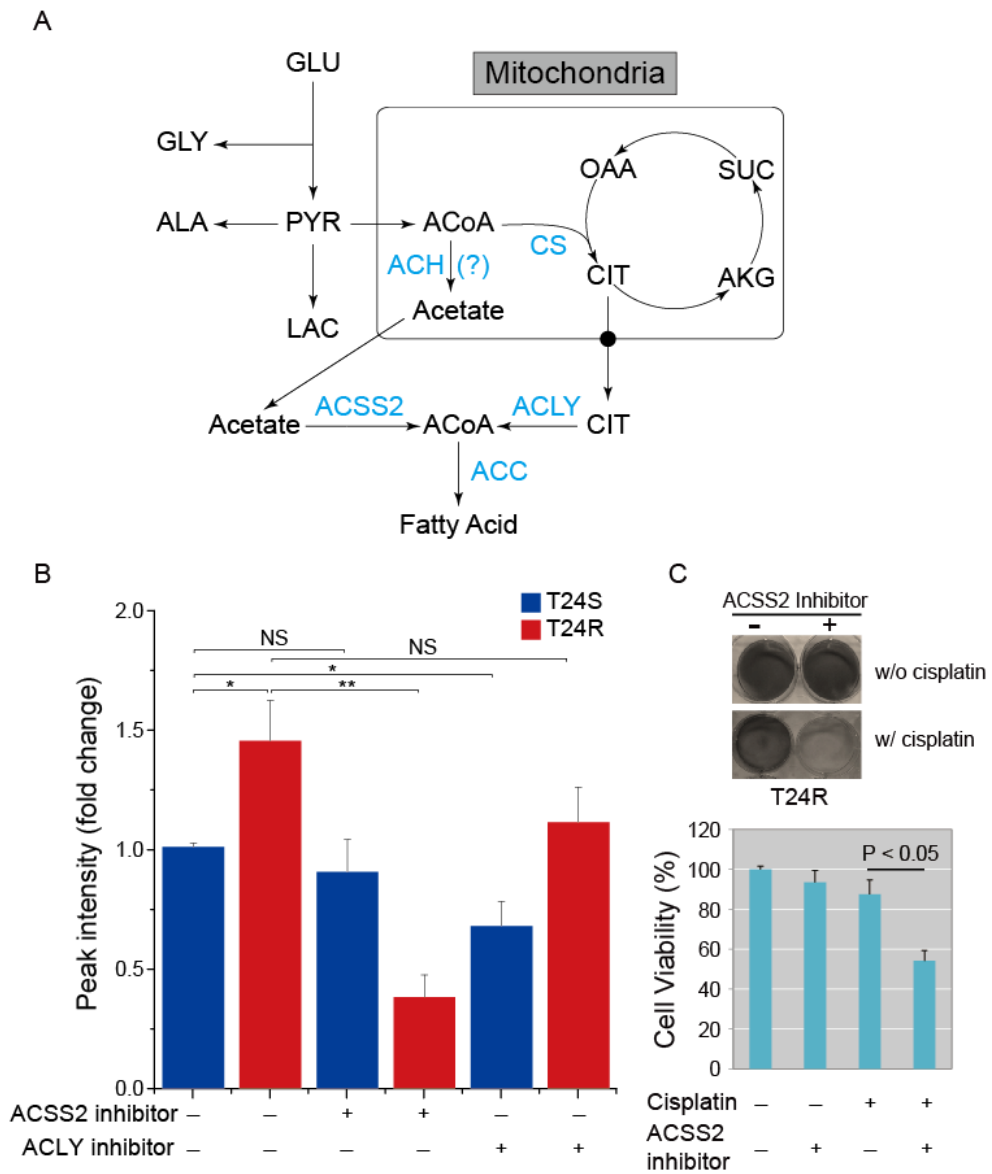
Figure 6. The involvement of ACSS2 in de novo fatty acid de synthesis and survival of T24R cells

(A) Schematic pathways for fatty acid synthesis from glucose. Pathways involving ACSS2 or ACLY are described. The question mark beside ACH indicates that the exact mechanism of acetate generation from pyruvate in mitochondria has yet to be firmly established. (B) The effects of ACSS2 and ACLY inhibitors on de novo fatty

26

acid synthesis in T24S (blue) and T24R (red) cells. The de novo synthesis was estimated as in Fig. 4 and normalized against that of T24S cultured without inhibitors. Either ACSS2 (15.6 μM) or ACLY (32 μM) inhibitors were added to the culture media. See the methods section for the chemical names of the inhibitors. Statistical analysis was performed using Student's t-test. **$P < 0.001$; *$P < 0.05$; NS, not significant ($P > 0.05$). The error bars represent the standard deviation. (C) The effect of the ACSS2 inhibitor on the cell survival of T24R cells in the presence of cisplatin. Upper: The T24R cells were seeded onto a 6-well plate 1 day before the experiment, and cells were treated with ACSS2 inhibitor or vehicle 1 h before the addition of cisplatin (10 μM). Cells were stained with crystal violet solution 48 h after cisplatin treatment. Lower: Bar graph for the cell viability obtained from photometric analysis of the upper samples. Abbreviations: glucose (GLU), glycine (GLY), alanine (ALA), pyruvate (PYR), lactate (LAC), acetyl-CoA (ACoA), oxaloacetate (OAA), succinate (SUC), a-ketoglutarate (AKG), citrate (CIT), acetyl-CoA hydrolase (ACH), citrate synthase (CS), acetyl-CoA synthetase 2 (ACSS2), ATP citrate lyase (ACLY), acetyl-CoA carboxylase (ACC).
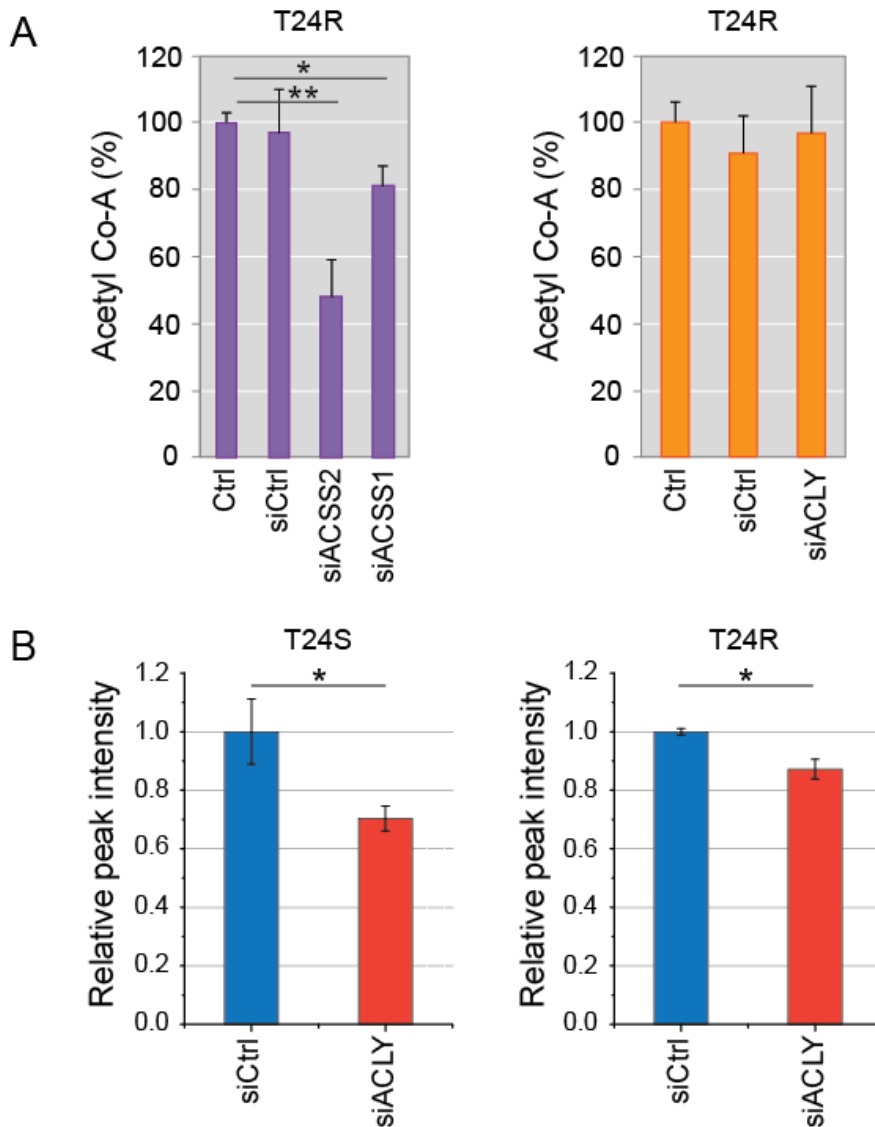
Figure 7. The effects of siRNA for ACSS2, ACSS1, and ACLY

(A) Knockdown of ACSS1, ACSS2, or ACLY was performed by transfection of T24R cells with siRNA duplex oligoset (ON-TARGETplus SMARTpool L-008549, L-010396, L-004915; Dharmacon, Lafayette, CO, USA) using Lipofectamine 2000 (11668019; Thermo Fisher Scientific, Waltham, MA, USA) according to the manufacturer's protocol. Acetyl-CoA was measured as described in the methods

section. (B) Knockdown of ACLY in T24S and T24R cells was performed by transfection of AccuTarget Genome-wide Predesigned siRNA for ACLY (1001365; Bioneer, Daejeon, Korea) using Lipofectamine RNAiMAX transfection reagent from Thermo Fisher Scientific according to the manufacturer's protocol. Fatty acid synthesis was measured as described for Fig. 4B.

F. ACSS2 expression increased in cisplatin-resistant patient tissue

To evaluate the relevance of the above results to the clinical setting, I investigated ACSS2 using patient tissues. I measured the expression of ACSS2 in bladder tumor tissues from patients who had undergone a series of cisplatin-based chemotherapies. Bladder tumor tissues obtained from BC patients with complete remission (CR) upon chemotherapies exhibited low levels of ACSS2, while those from patients with progressive disease (PD) had much higher levels of ACSS2 expression (Fig. 8A and B). Representative immunohistochemistry (IHC) images are also provided in Fig. 8C. These results confirmed the relevance of ACSS2 in the cisplatin resistance of BC. As cisplatin-resistant BCs are often more aggressive, I also performed IHC analysis using tissue microarrays (TMA) of BC of varying aggressiveness. The results showed that the levels of ACSS2 protein expression were significantly associated with the aggressiveness of BC (Fig. 9).
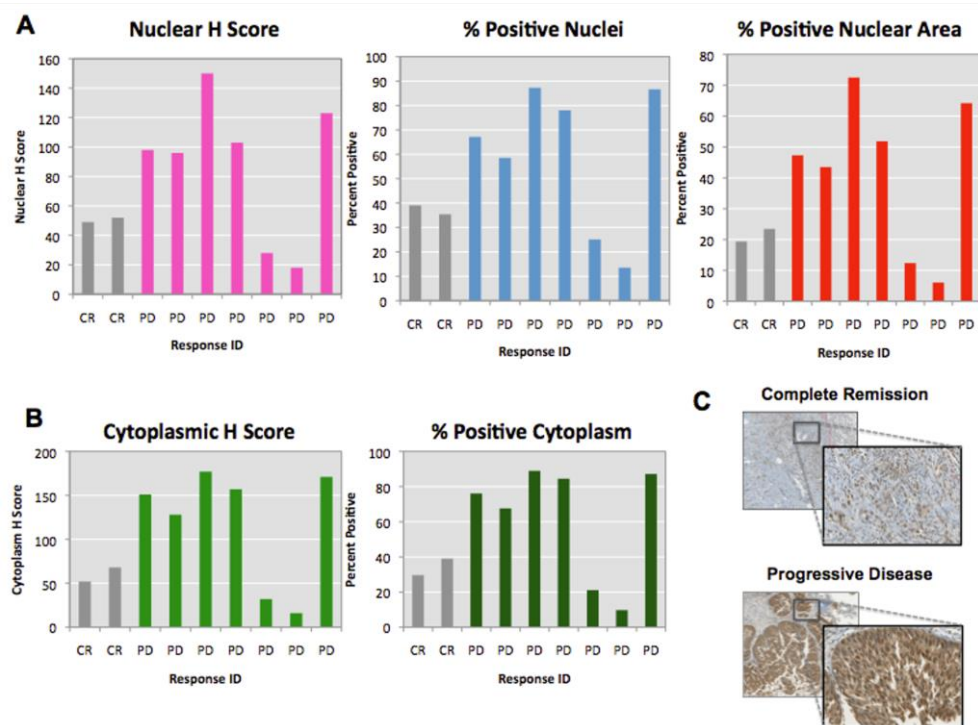
Figure 8. The expression levels of ACSS2 in tissues from cisplatin-sensitive and -resistant BC patients

(A) Quantitative analysis of annotated nuclear regions from the IHC results; the nuclear H-score, percentage positive nuclei, and percentage positive nuclear area in BC tumors are presented. (B) Quantitative analysis of annotated cytoplasmic regions from the IHC results; the cytoplasmic H-score and percentage positive cytoplasm are presented. (C) Representative digitalized IHC images. Complete remission (CR: cisplatin-sensitive) or progressive disease (PD: cisplatin-resistant) groups. An anti-ACSS2 antibody was used for IHC staining.
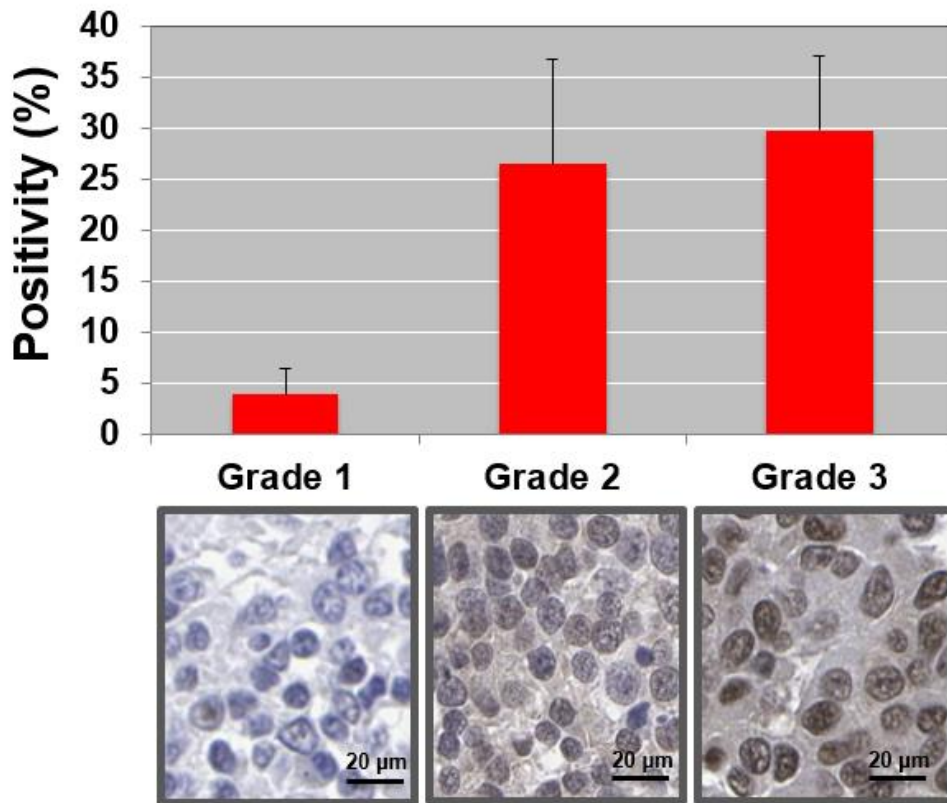
Figure 9. ACSS2 protein expression in tissue samples from patients with BC of various aggressiveness

IHC analysis was performed on the commercial BC tissue microarray (TMA) using anti-ACSS2 antibody. Positivity was calculated in at least 500 cells in 20 cores in the TMA. Representative images for each grade are shown.

IV. Discussion

By employing a live metabolomics and biochemical approach, I showed that glucose-derived endogenous acetate contributes to fatty acid synthesis in cisplatin-resistant cells. Like DNA, fatty acids are required components of proliferating cells and, therefore, it is unsurprising that cisplatin-resistant cells have alternative machinery for making fatty acids in the presence of the toxic drug. However, the use of endogenous acetate in fatty acid synthesis may require more explanation. The most well-established pathway for fatty acid synthesis utilizes citrate as an intermediate for acetyl-CoA, whether it is from glucose or glutamine [46]. Citrate formed in the mitochondria is broken down in the cytosol by ACLY to give oxaloacetate and acetyl-CoA, which can be used for fatty acid synthesis. Another pathway for fatty acid synthesis involves exogenous acetate and requires ACSS2 to generate acetyl-CoA in the cytosol [17]. Although ACSS2 involvement is the same for exogenous and endogenous acetate use in fatty acid synthesis, I showed that there is less ^{13}C incorporation into fatty acids from exogenous ^{13}C-acetate in cisplatin-resistant cells than cisplatin-sensitive cells. Therefore, endogenous acetate seems to be the preferred source of the two-carbon units needed for fatty acid synthesis in the cisplatin-resistant cancer cells. Actually, the formation of endogenous acetate in cancers is not unprecedented. It was first documented about 80 years ago [47], but its roles in cancer metabolism have been little considered. For general fatty acid synthesis, too, endogenous acetate was proposed as an intermediate around 50 years ago [48], but it has been largely neglected compared with citrate as the main intermediate [14, 46]. Now, my data suggest a novel implication of

endogenous acetate from glucose in fatty acid synthesis in cisplatin-resistant cells. Through the currently available state-of-the-art analytical techniques, I expect more roles of endogenous acetate in cancer metabolism to be revealed.

My data suggest that endogenous acetate is derived from glucose, most probably through pyruvate, and it was shown that acetate can be generated from pyruvate in the mitochondria [49]. I also observed a decrease in acetate production when T24R cells were treated with UK5099, an inhibitor of mitochondrial pyruvate carrier (MPC) (Fig. 10). Pyruvate uptake through MPC is lower in some cancer cells, but many cancers still import pyruvate into the mitochondria. For example, glioblastomas generate about half of their cellular glutamate using the glucose-driven TCA cycle that goes via pyruvate [15]. In osteosarcoma cells, glucose-derived citrate via pyruvate accounted for ~60% of total the citrate pool [50]. The simultaneous enhancement of the Warburg effect and TCA cycle using glucose-derived pyruvate was also observed in small cell lung cancer [51]. Therefore, despite the pronounced Warburg effect that can reduce pyruvate uptake into cancer cell mitochondria and reduced MPC functions in some cancer cells, pyruvate can still contribute to acetate generation in the mitochondria. The higher oxygen consumption rate of T24R cells is also evidence for functional mitochondria activity in T24R cells (Fig. 11).

An interesting question is raised as to how increased fatty acid synthesis affects cisplatin chemosensitivity. There have been several reports linking fatty acid synthesis to cancer drug resistance. First, de novo fatty acid synthesis may lead to plasma membrane remodeling by changing its fatty acid and lipid compositions. This can lead to alterations of drug uptake and intracellular drug concentrations, which

affect chemosensitivity [52, 53]. Second, increased de novo fatty acid synthesis has been reported to lower the proportions of unsaturated fatty acids in plasma membranes [53]. Lower unsaturated fatty acid levels have been implicated in the reduced efficacy of anti-cancer drugs, as unsaturated fatty acids are important sources of reactive oxygen free radicals [53]. In addition, the production of ROS is an important mechanism in the cytotoxicity of many anti-cancer drugs, including cisplatin. Third, increased fatty acid synthesis by FASN overexpression may protect cancer cells from apoptosis. The increased FASN reduces the biosynthesis of pre-apoptotic lipid molecules, which has been suggested as a new chemoresistance mechanism [54]. As the above mechanisms are not mutually exclusive, the increased cisplatin resistance associated with elevated fatty acid synthesis from glucose-derived acetate may involve all the above or further yet-to-be-identified pathways.

By implicating ACSS2 in the chemosensitivity of cells and patient tissues, my results provide two key opportunities for translating the research to the clinical setting. As elevated levels of ACSS2 were observed in cisplatin-resistant patient tissues, which are often more invasive and refractory, ACSS2 levels could be used to stratify patients who would require more aggressive treatment from the beginning. In addition, ACSS2 levels may be helpful in deciding whether cisplatin should be administered to particular patients. Furthermore, inhibitors of ACSS2, along with other treatment modalities, may be used to treat cisplatin-resistant BC patients. Although the inhibitor used in the current study may be unsuitable for use in the clinical setting, the development of more inhibitors is expected because of the importance of ACSS2 in the tumorigenesis of glioblastoma and hepatocellular carcinoma [15, 17]. In addition, other enzymes in the fatty acid synthetic pathway

involving endogenous acetate may be novel targets for cisplatin-resistant BC treatment, e.g., acetyl-CoA thioesterase, which is needed for acetate transport across the mitochondrial membrane.
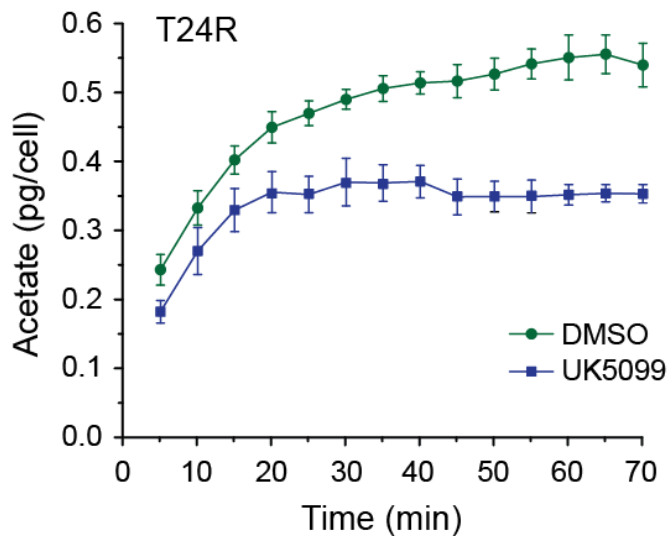
Figure 10. The effects of mitochondrial pyruvate carrier inhibitor, UK5099, on acetate production in T24R cells

3×10^7 T24R cells were harvested and resuspended in culture medium containing 0.2 mM UK5099 (PZ0160; Sigma-Aldrich, ST. Louis, MO, USA). After incubation for 30 min, final 25 mM ^{13}C-glucose was added to the medium. Then real-time 2D ^{1}H-^{13}C HSQC NMR spectra were obtained, and the acetate level was measured from the calibrated peak intensity.
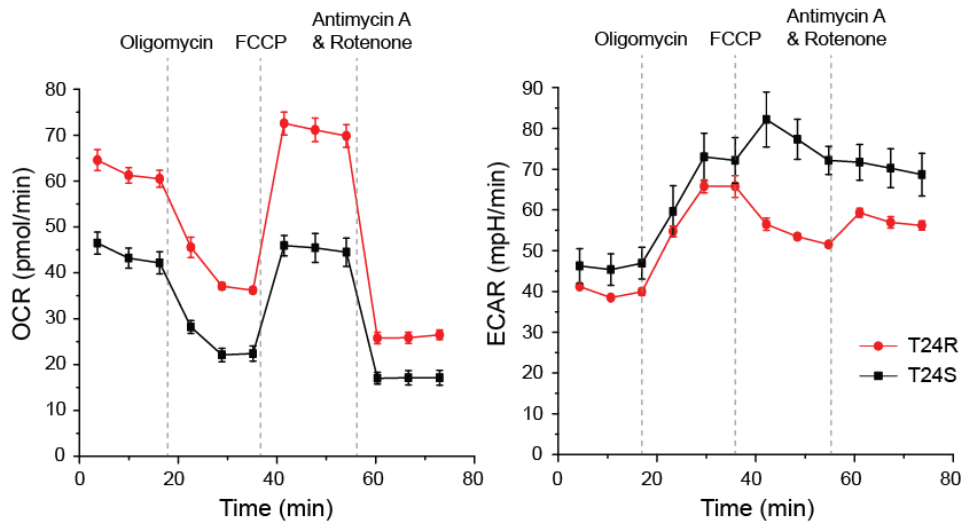
Figure 11. Oxygen consumption rate (OCR) and extracellular acidification rate (ECAR) of T24S and T24R cells

OCR (left) and ECAR (right) were measured in an XFp Analyzer (Seahorse Bioscience, North Billerica, MA, USA) using the manufacturer's protocol. Briefly, 10,000 T24S and T24R cells were plated onto XFp cell culture mini-plates 24 h prior to the assay. The media were changed to serum-free XF assay media with 25 mM glucose, 1 mM pyruvate, and 2 mM glutamine, and the culture plates were placed into a 37°C non-CO_2 incubator 1 h prior to the assay. The XFp Cell Mito Stress Test Kit (Seahorse Bioscience, 103010) was used, and the media were injected with 1 μM oligomycin, 1 μM FCCP, and 0.5 μM antimycin A & rotenone at 18, 36, 54 min time-points.

3. Part II

Acetate metabolism characterizes

malignancy, metabolic nature, and prognosis

of liver cancer

I. Introduction

Glucose has been thought of as the preferred nutrient for cancer cells since Otto Warburg described the aerobic glycolytic properties of all growing cancer cells [8]. Nevertheless, other nutrients, such as glutamine, lactate, and acetate, can be utilized by tumors according to their innate or environmental conditions [14, 55, 56]. Among them, acetate usage is dependent upon acetyl-CoA synthetase 2 (ACSS2) [17], and its use by cancer cells seems to occur in mostly nutrient-deplete or hypoxic conditions [14, 17, 57]. Another aspect of acetate uptake is its relationship with tumor malignancy. Higher levels of ACSS2 were found to be associated with a shorter survival time and metastases of brain, breast, and prostate cancers [15, 18]. For liver cancer, bioinformatic analyses suggested links between increased acetate utilization and higher malignancy under hypoxic conditions [58, 59]. Furthermore, in animal liver cancer models, much higher tumor burdens were observed in the presence of intact *ACSS2* genes [17].

Although the above studies suggest the existence of positive correlations among hypoxia/nutrient depletion, higher acetate uptake, and cancer malignancy, there is also evidence against these associations. It is established that high levels of glucose uptake, which may limit acetate uptake, are induced under hypoxic conditions by hypoxia-inducible factors that are associated with a higher cancer malignancy [60, 61]. Acetate metabolism through ACSS2 seems to be important in leukemogenesis [62], although blood cancer cells are exposed to a nutrient- and oxygen-rich environment. Positron emission tomography (PET) imaging showed that well-differentiated liver cancer is more effectively detected with ^{11}C-acetate, whereas poorly-differentiated liver cancer is effectively detected with ^{18}F-fluorodeoxyglucose [63]. Therefore, many controversies exist regarding the relationships among acetate uptake, nutrient availability, and cancer malignancy, and these may differ according to cancer type and stage.

The nutrient usage and metabolic characteristics of the liver may differ from, or are even opposite to, those of other organs, as exemplified by glucose and cholesterol synthesis in the liver and their consumption in other organs [64]. Given the unique metabolic nature of the liver and the controversies stated above, the relationships among acetate uptake, metabolic characteristic, and the malignancy of liver cancer may not be extrapolated from other tumors and are far from established. In this study, I comprehensively studied the above relationships in liver cancer at the cell, animal model, and patient levels using isotopic tracing, molecular biology, transcriptomics, clinical analysis, and PET-CT imaging of patients.

II. Materials and methods

1. Chemicals and reagents

The stable isotope labeled sodium acetate (CLM-440-1, 1,2-^{13}C$_2$, 99%) and D-glucose (CLM-1396-5, U-^{13}C$_6$, 99%) were purchased from Cambridge Isotope Laboratories (Andover, MA, USA). The inhibitor for ACSS2, 1-(2,3-di(thiophen-2-yl)quinoxalin-6-yl)-3-(2-methoxyethyl)urea was purchased from ChemBridge (San Diego, CA, USA). The inhibitors for LDH (Galloflavin) and for mTOR (Torin1) were purchased from Tocris Bioscience (Minneapolis, MN, USA). The inhibitor for CPT1 (Etomoxir) was purchased from Cayman Chemical (Ann Arbor, MI, USA). The ACSS2 antibody (PA5-52059) from Thermo Fisher Scientific (Waltham, MA, USA) and β-actin antibody (sc-47778) from Santa Cruz Biotechnology (Santa Cruz, CA, USA) were used. N-Nitrosodiethylamine (DEN) was purchased from Sigma-Aldrich (St. Louis, MO, USA).

2. Cell culture and isotope labeling

HepG2 and Hep3B liver cancer cell lines were cultured in DMEM (Welgene, Daegu, Korea) supplemented with 10% fetal bovine serum (FBS; Welgene, Daegu, Korea) and 1% penicillin-streptomycin solution (Gibco, Grand Island, NY, USA). For isotope labeling, cells were cultured for 16 h in D-glucose-free DMEM (Gibco, Grand Island, NY, USA) supplemented with 10% dialyzed FBS (Welgene, Daegu, Korea), 1% penicillin-streptomycin solution, 5 mM U-^{13}C$_6$-D-glucose (in the presence of unlabeled 0.2 mM acetate), and/or 0.2 mM 1,2-^{13}C$_2$-

sodium acetate (in the presence of unlabeled 5 mM glucose), as necessary.

3. Glucose and acetate uptake by cell liens

The cells were incubated for 6 h with either 0.2 mM 1,2-^{13}C$_2$-acetate (with unlabeled 5 mM glucose) or 5 mM U-^{13}C$_6$-glucose (with unlabeled 0.2 mM acetate) in the media. The medium was collected and spun down at 21,000g for 10 min. The supernatants were mixed with 10% buffer composed of 2 mM Na$_2$HPO$_4$ and 5 mM NaH$_2$PO$_4$ in D$_2$O with 0.025% TSP. The NMR spectra were obtained with an 800 MHz NMR machine using 1D heteronuclear single quantum coherence (HSQC) (TD 16384) experiment. The uptake was evaluated by measuring the peak intensities of the remaining 1,2-^{13}C$_2$-acetate or U-^{13}C$_6$-glucose in the media with 1D heteronuclear NMR. The intensities were compared with the initial intensities of the isotopic metabolite peaks.

4. Glucose and acetate metabolism in orthotopic liver cancer and normal mice

Following Institutional Animal Ethics Committee permission at Inha University (INHA-181120-600-1), four-week-old, male BALB/c nude mice were purchased from Orient Bio (Seoul, Korea). The human liver cancer orthotopic nude mouse models with Hep3B and HepG2 cells were established, as previously described [65]. A midline incision of the anterior abdominal wall was made, and 1×10^6 cells in a total volume of 30 µl of a 50:50 solution of PBS and matrigel were directly injected into the left lobe of the liver under anesthesia by pentobarbital

sodium. After 2 months, mice were fasted for at least 12 h, and were orally administered U-^{13}C$_6$-D-glucose (5g/kg, 300 µl) or 1,2-^{13}C$_2$-sodium acetate (3g/kg, 300 µl) for orthotopic xenograft models. Animals were euthanized at 30 min and 120 min after the administration of the U-^{13}C$_6$ glucose and 1,2-^{13}C$_2$-acetate, respectively. Tissues were collected and rapidly frozen to quench metabolism, and stored at −80°C for further analysis. The normal mice were orally administered U-^{13}C$_6$ glucose (5 g/kg, 300 µl) or 1,2-^{13}C$_2$-acetate (5 g/kg, 300 µl) and euthanized at 30 min and 60 min after the administration, respectively. The different times of euthanasia were chosen so that each isotopic metabolite may have maximum incorporation, as revealed in preliminary experiments.

5. Metabolite extraction

2×10^7 cells were harvested with Trypsin-EDTA (Gibco, Grand Island, NY, USA) and centrifugation. The harvested cells were resuspended with 900 µl methanol-chloroform solution (2:1, v/v). After 3 cycles of liquid nitrogen-thaw-shaking (20 min), 300 µl chloroform and 300 µl distilled water were added to the cell lysates. The samples were centrifuged at 21,000g for 10 min at 4°C. The lipid layer and the water layer were dried separately with a vacuum centrifugator (Vision, Seoul, Korea). For NMR measurement, the pellet was resuspended with 500 µl of buffer composed of 2 mM Na$_2$HPO$_4$ and 5 mM NaH$_2$PO$_4$ in D$_2$O with 0.025% TSP. For liquid chromatography-mass spectrometry (LC-MS) measurement, the pellet was reconstituted with 40 µl acetonitrile:distilled water (1:1, v/v) and 2 µl was introduced after centrifuging at 21,000g for 10 min at 4°C. Mouse tissues were cut

to a size of 100 mg and extracted in the same way as the cell extraction method after homogenization with a disposable homogenizer (BioMasher, Nipi, Tyoko, Japan).

6. NMR measurement

The data were obtained with an 800 MHz Bruker Avance III HD spectrometer equipped with a 5 mm CPTCI CryoProbe (Bruker BioSpin, Billerica, MA, USA). 2D HSQC spectra were obtained with a Bruker pulse sequence hsqcetgpsisp2.2. The dataset comprises 1024 × 512 complex points. Each experiment had 5 scans per T1 increment, which took 1 h 35 min. If applicable, the number of non-uniform sampling (NUS) points was 128 complex points (25% sampling density of 512 points) using the nuslist provided by Topspin software. The non-uniform sampling NMR experiment was performed as described previously [43].

7. LC-MS measurement for isotopomer distribution

The samples were analyzed by an Acquity ultra-performance liquid chromatography (UPLC; Waters Corp., Milford, MA, USA) using a SeQuant® ZIC®-pHILIC polymeric beads PEEK column (150 x 2.1 mm, 5 μm; Merck, Darmstadt, Germany). 10 mM ammonium carbonate (pH = 9) in distilled water (A) and acetonitrile (B) were used as the mobile phase, and the flow rate was 0.15 ml/min. The gradient was as follows: 20% A at 0 min, 20% A at 2 min, 80% A at 19 min, 80% A at 30 min, 20% A at 30.5 min, and 20% A at 35 min. The hydrophobic sample separation was performed on a Kinetex C18 column (100 x 4.6 mm, 2.6 μm; Phenomenex, Torrance, CA, USA). 60:40 (v/v) acetonitrile:distilled water with 10 mM ammonium acetate (A) and 90:10 (v/v) isopropanol:acetonitrile with 10 mM

ammonium acetate (B) were used as the mobile phase, and the flow rate was 0.4 ml/min. The gradient was as follows: 85% A at 0 min, 70% A at 3.25 min, 52% A at 4 min, 18% A at 16.75 min, 1% A at 17.5 min, 1% A at 18.25 min, 85% A at 18.40 min, and 85% A at 23 min. The MS data were obtained with a Q Exactive™ Focus Hybrid Quadrupole-Orbitrap™ Mass Spectrometer (Thermo Scientific, Waltham, MA, USA). The isotopomer distribution was obtained from the LC-MS peak intensities after natural abundance correction and the relative abundance was expressed as a percentage relative to the sum of all the isotopomers intensities including M+0.

8. Immunohistochemistry (IHC) with human liver cancer tissues

Human liver cancer tissue microarrays with normal (n = 22), liver cirrhosis (n = 28), hepatocellular carcinoma (HCC; n = 69), and metastatic HCC (n = 15) patients were purchased (US Biomax, Rockville, MD, USA) and used to detect the expression of the ACSS2 levels. Tissue array slides were deparaffinized with xylene and dehydrated with ethanol. Antigen retrieval was performed by microwave heating methods in citrate solution for 20 min. Blocking solution was used to prevent nonspecific binding of antibodies. The tissue sections were incubated with polyclonal ACSS2 antibody (1:50 dilution) for overnight at 4°C. HRP Detection System (HRP streptavidin label and polyvalent biotinylated link) and diaminobenzidine (DAB) Substrate Kit were used as detecting reagents (Vector Laboratories, Burlingame, CA, USA). After counterstaining with hematoxylin, the sections were dehydrated and mounted. All ACSS2-stained slides were scanned

using the ScanScope System (Leica Biosystems, Wetzlar, Germany). A pathologist with subspecialty training in HCC pathology assured that areas selected for automated image analysis represented appropriate tissues. Staining intensity was graded with: none as 0, weak as 1+ (< 30%), moderate as 2 (+30–60%), and strong as 3+ (> 60%).

9. Fluorescent signal quantification

Equal number of cells were plated onto confocal dishes (200350; SPL Life Sciences, Gyeonggi-do, Korea). The cells were stained with Hoechst 33342, MitoTracker™ Red CMXRos, and Bodipy™ FL C_{12} from Thermo Fisher Scientific (Waltham, MA, USA) for 15 min. The stained cells were washed with DPBS and fixed with 4% paraformaldehyde solution for 30 min at RT. The fluorescent signals were measured by a Confocal Scope TCS8 (Leica Microsystems, Wetzlar, Germany).

10. Wound healing and clonogenic assay

Wound healing assay was conducted to assess cell migration. Lines were made with a sterile 1 ml pipette tip. At 0, 24, 48, and 72 h, images were taken with an AmScope microscope digital camera MD800E (Irvine, CA, USA). Wound healing area was measured by the ImageJ software program. HepG2 or Hep3B cells (800 per well) were seeded into a 6-well plate and cultured in DMEM supplemented with 10% FBS for 2 weeks. Then, the cells were fixed and stained with crystal violet (0.5% w/v) solution in 20% methanol. The colonies were counted.

11. Knockdown experiments with siRNA

The predesigned siRNAs targeting *ACSS2* (55902-1), *LDH* (3939-1), *mTOR* (2475-1), and *CPT1* (1374-1) were purchased from Bioneer (Daejeon, Korea). The cells were transfected with 100 nM siRNA with Lipofectamine RNAiMAX for 48 h (Thermo Fisher Scientific, Waltham, MA, USA). The media were changed with fresh media and CCK8 proliferation assays were conducted with D-PlusTM CCK after 24 h (Dongin Biotech, Seoul, Korea). The cellular viability was measured for absorbance at 450 nm by a microplate reader (Molecular Devices, San Jose, CA, USA).

12. DEN-induced rat liver cancer model

For rat liver cancer model, male Sprague-Dawley rats weighing 150-180 g were administered DEN in their drinking water (100 mg/l) and then, DEN-administered rats were sacrificed at indicated times.

13. PET-CT imaging

The Institutional Review Board of Yonsei university approved this retrospective study, and the requirement to obtain informed consent was waived (Yonsei IRB number: 4-2015-0904). Patients with blood glucose concentrations of less than 140 mg/dl were fasted for at least 6 h before the intravenous injection of ^{18}F-FDG. Approximately 5.5 MBq of ^{18}F-FDG per kg of body weight was administered. 60 min after the injection, PET-CT scanning was performed from the skull base to the mid-thigh in a three-dimensional mode at 2 min per bed position on

a dedicated PET/CT scanner (Discovery 600; General Electric Medical Systems, Milwaukee, WI). Low-dose CT was performed using the following parameters: a scout view at 10 mA and 120 kVp, followed by a spiral CT scan with a 0.8 sec rotation time, 60 mA, 120 kVp, 3.75 mm section thickness, 1.25 mm collimation, and 27.5 mm table feed per rotation with arms raised. CT images were reconstructed onto a 512×512 matrices and were converted into 511 keV equivalent attenuation factors for attenuation correction. PET images were reconstructed onto a 128×128 matrices using ordered subset expectation maximization and corrected for random and scatter coincidences. In addition, a separate PET-CT scan was obtained on the same scanner 20 min after intravenous injection of 370–555 MBq of ^{11}C-acetate at 2 min per bed position. The same attenuation correction and image reconstruction were done for ^{11}C-acetate images. The comparison for the higher and lower grade cancer was made for those patients who had their tumor resected for surgical treatments and their tissues evaluated by histological examination. Due to the rare indication of surgical treatments for very highly malignant cancer (grade IV), the comparison was made between grade II and grade III tumor cases.

14. Gene Set Enrichment Analysis (GSEA)

For GSEA between HepG2 and Hep3B cell lines, the signal values of GSE21955 dataset were downloaded, and an offset of 34.1226 was added to the whole dataset values in order to make them all positive. The data were log2 transformed and probes were collapsed to gene symbols. When running GSEA, only gene sets related with metabolism were used. These gene sets were obtained by downloading all pathways from Reactome (www.reactome.org, downloaded in April 2019), and extracting only pathways under "Metabolism" hierarchy. For GSEA between high ACSS2 and low ACSS2 patient groups, the same metabolism gene sets were used. For GSEA used in the Fig. 20, the same GSEA method between HepG2 and Hep3B cell lines used in Fig. 15 was used, except that the gene set used was "h.all.v7.1.symbols.gmt" in MSigDB (Molecular Signatures Database).

15. Survival analysis

Kaplan-Meier analysis was performed with "survival" and "survminer" package in R, and OriginPro 8 software. The same method was applied to GSE76427 dataset. The best risk separation followed the strategy described previously [66] using an in-house built R script.

16. Clinical data sources

The mRNA expression levels (RSEM normalized counts) were obtained from TCGA Pan-Cancer Atlas (https://gdc.cancer.gov/about-data/publications/pancanatlas, downloaded in February 2020). The survival information was obtained from TCGA-CDR. Tumor grade information was obtained from TCGA GDC portal (http://portal.gdc.cancer.gov/, downloaded in February 2020). Disease-free status information was obtained from cBioportal (www.cbioportal.org, (Cerami et al., 2012; Gao et al., 2013), downloaded in May 2020). The hypoxia score was downloaded from cBioportal (www.cbioportal.org, downloaded in March 2020).

17. Methylation analysis

The beta values of TCGA-LIHC were obtained from TCGA Pan-Cancer Atlas (https://gdc.cancer.gov/about-data/publications/pancanatlas, downloaded in April 2020). For each probe, the difference of medians of beta values from the high ACSS2 group to the low ACSS2 group was calculated. The P-value was calculated by Wilcoxon rank-sum test and False Discovery Rate (FDR) by Benjamini-Hochberg method. Then, for each probe, -log10(FDR) multiplied by the sign of the difference of the medians of the beta values was obtained and plotted. Among the multiple probes for *ACSS2* or *FASN* gene, the probe which was the most negatively correlated (by Spearman's rank correlation) with the gene expression was selected and marked as diamond (*ACSS2* gene) and square (*FASN* gene) in Fig. 25F. For *ACSS2* gene, the probe was "cg09801828", and for *FASN* gene, the probe was "cg25068915".

18. Statistical analysis

Statistical analysis between two groups was performed using R 3.6.2. Except for the hypoxia scores and methylation analysis, where Wilcoxon rank-sum test was used, Student's t-test or Welch's t-test was used, depending on the P-value of F-test (threshold of 0.05). Error bars in the bar graphs represent the standard deviation.

III. Results

A. Acetate uptake and its association with cancer cell growth under varying glucose concentrations

Despite reports showing acetate uptake occurring in primarily glucose-depleted or hypoxic environments [17, 18], such conditions would also limit acetate usage. This led me to hypothesize that if tissues use acetate at all, nutrient depletion is not always pre-requisite for the use of acetate. Therefore, I first tested if acetate can be used in normal liver tissues where nutrients and oxygen are replete. Mice were given the same amounts of ^{13}C-acetate or ^{13}C-glucose orally, and their liver tissues were analyzed for the isotope incorporation into glutamate [15]. The ratios of the ^{13}C-labeled glutamate isotopomers and the M+2 isotopomer, formed from the first cycle of acetate incorporation, were similar in both groups (Fig. 12A). These data show that the livers can utilize acetate carbons as efficiently as glucose carbons in normal conditions. Then, I compared acetate uptake among various liver cell lines in the presence of both physiological acetate and glucose. The cell line with the highest acetate uptake, HepG2, exhibited an approximately 4-fold higher acetate consumption than Hep3B, whereas Hep3B consumed much more glucose than HepG2 (Fig. 12B). Additionally, both mRNA and protein levels of ACSS2, critical in acetate utilization [15, 17, 64], were significantly higher in HepG2 cells (Fig. 12C). These data show that liver cancer cells with high ACSS2 levels, such as HepG2, can efficiently take up acetate even in a glucose-replete condition.

To test if differential acetate uptake affected the cell phenotypes, I measured cell growth. In the presence of 0.2 mM acetate, lowering the glucose concentration from 5 to 1 mM significantly inhibited the growth of Hep3B cells but not HepG2 cells (Fig. 12D). An even lower concentration of glucose (0.2 mM) further suppressed the growth of Hep3B cells, but the inhibition was significantly ameliorated in HepG2 cells by acetate. In these conditions, a high concentration of acetate (4 mM) significantly rescued the growth of HepG2 cells but not Hep3B cells. Overall, acetate uptake in normal physiological conditions seems to be an inherent property of liver tissue, and there is heterogeneity in acetate uptake among liver cancer cells. Therefore, I further investigated the heterogeneity of acetate metabolism and related cell physiology in liver cancer using HepG2 and Hep3B cells.
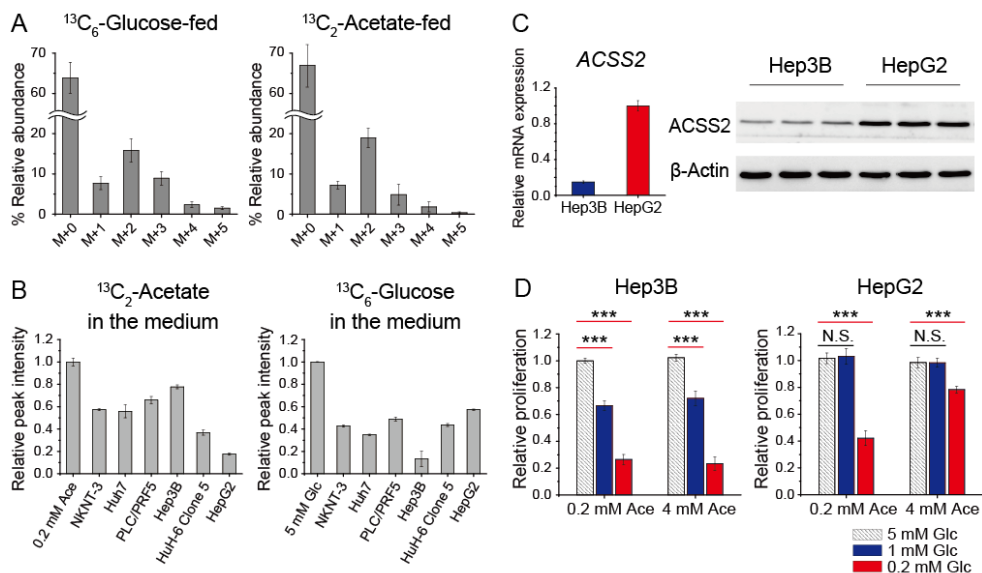
Figure 12. Acetate uptake in normal mouse liver tissue and cancer cells and its relationship with cell growth

(A) Glutamate isotopomer distribution in normal liver tissue of mice fed U-$^{13}C_6$-glucose (left) or 1,2-$^{13}C_2$-acetate (right) (both 5 g/kg) as measured with LC-MS (UPLC-Q Exactive Focus). (B) Uptake of 1,2-$^{13}C_2$-acetate (left, 0.2 mM) or U-$^{13}C_6$-glucose (right, 5 mM) by various liver cell lines as measured by NMR intensities of the remaining tracers in the media compared with their initial intensities (bars on the far left of each graph). (C) qRT-PCR (left) and western blot analysis (right) of acetyl-CoA synthetase 2 (*ACSS2*) expression in total cell extracts of Hep3B and HepG2 cells. (D) Hep3B (left) and HepG2 (right) growth measured using the CCK8 method with the indicated concentrations of acetate (Ace) and glucose (Glc). N.S.: not significant; *P < 0.05; **P < 0.01; ***P < 0.001 (n = 3, unless otherwise stated) from Student's *t*-test with standard deviations.

54

B. Differential metabolic fates of acetate and differential gene expression in high- and low-ACSS2 cells

For the high- and low-ACSS2 cells, I measured ^{13}C-acetate incorporation into the cellular metabolites using high-resolution 2D HSQC NMR (Fig. 13) [43]. HepG2 utilized ^{13}C-acetate in diverse biosynthetic pathways, leading to its incorporation into various amino acids, TCA intermediate succinate, acetylated amino acid N-acetyl aspartate, and even nucleic acid base (NAB) uridine (Fig. 14A). In comparison, Hep3B cells did not show appreciable incorporation of ^{13}C-acetate for most of these metabolites, consistent with the minimal effects of acetate on Hep3B growth. Acetate incorporation was also measured for hydrophobic lipids using omega methyl NMR peak splitting [64]. HepG2 exhibited higher de novo fatty acid synthesis from ^{13}C-acetate than Hep3B cells (Fig. 14B), and, interestingly, even from ^{13}C-glucose (Fig. 14C). Consistently, ^{13}C incorporation from ^{13}C-glucose into glycerol 3-phosphate, a substrate of the rate-limiting enzyme of lipid synthesis (GPAM), was higher in HepG2 (Fig. 14D). Conversely, glycerophosphocholine, an end-product of catabolic glycerophospholipid lipases, was highly labeled by ^{13}C-glucose in Hep3B cells. In addition, the higher incorporation of ^{13}C-glucose into lactate suggested more active catabolic glycolysis in Hep3B cells. Further measurement of lipid droplets via fluorescence showed significantly higher lipid contents in HepG2 cells than Hep3B cells (Fig. 14E). These results suggest that high-ACSS2 HepG2 cells have a higher anabolic capacity using both acetate and glucose, whereas Hep3B cells appear to be more catabolic, especially in terms of lipid metabolism.

To determine if the above differential metabolic characteristics are reflected

at the gene expression level, the transcriptomic profiles of the cells were analyzed using the GSE21955 dataset. The Gene Set Enrichment analysis (GSEA) results for metabolic genes showed that HepG2 cells exhibited significant enrichment in anabolic pathways for lipids and amino acids and pathways for a master regulator of lipid synthesis (SREBP) (Fig. 15). In addition, the individual expressions of several genes that are key to diverse lipid biosynthetic pathways, such as *ACACA*, *FASN*, and *GPAM*, were consistently upregulated in HepG2 cells (Fig. 16A and B). These results support the idea that HepG2 cells, with higher ACSS2 levels and acetate uptake, have more anabolic characteristics.
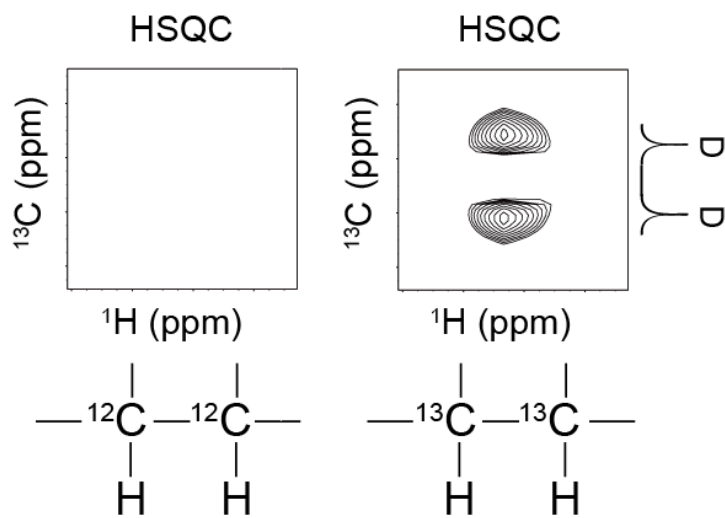
Figure 13. 2D HSQC NMR spectrum showing peak splitting by ^{13}C-^{13}C J-coupling
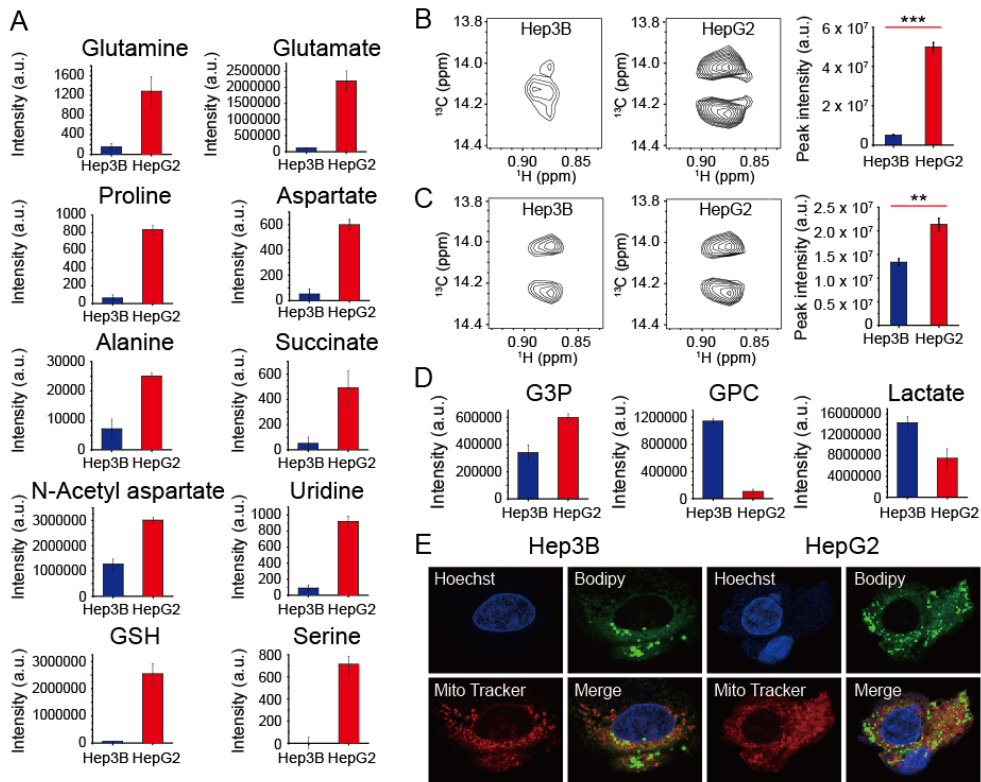
Figure 14. Different metabolic fates of acetate in high- and low-ACSS2 cells

(A) Isotopic incorporation of 0.2 mM 1,2-$^{13}C_2$-acetate into various metabolites in Hep3B and HepG2 cells, as measured with ^{13}C-^{13}C J-split peaks in 2D NMR spectra. (B and C) De novo fatty acid synthesis by 0.2 mM 1,2-$^{13}C_2$-acetate (B) or 5 mM U-$^{13}C_6$-glucose (C) in Hep3B and HepG2 cells, as measured by the intensities of omega methyl splitting from high-resolution NMR spectra (left and middle spectra) [43]. Peak intensity averages (right bar graphs). (D) Isotopic incorporation of 5 mM U-$^{13}C_6$-glucose as in (A). (E) Lipid droplet levels (Bodipy FL C_{12}; green) measured with confocal microscopy. Nucleus (Hoechst 33342; purple) and mitochondria (MitoTracker Red CMXRos; red). $**P < 0.01$; $***P < 0.001$ (n = 3, unless otherwise stated) from Student's t-test with standard deviations. Abbreviations: glutathione (GSH), glycerol 3-phosphate (G3P), glycerophosphocholine (GPC).
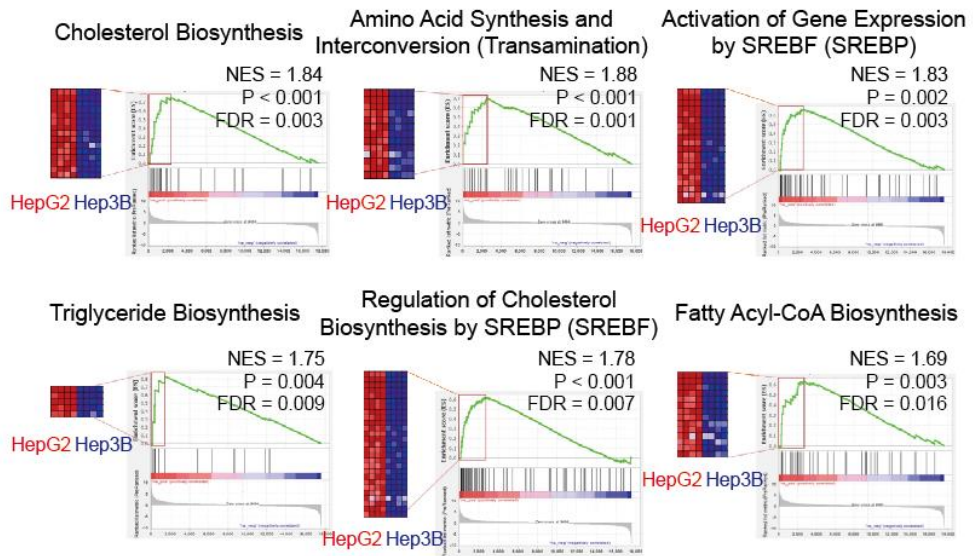
Figure 15. GSEA results of gene expression related to lipid synthesis pathways in Hep3B and HepG2 cells from GSE21955 dataset

Control groups with negative control siRNA treatment of both cells were used in the analysis.
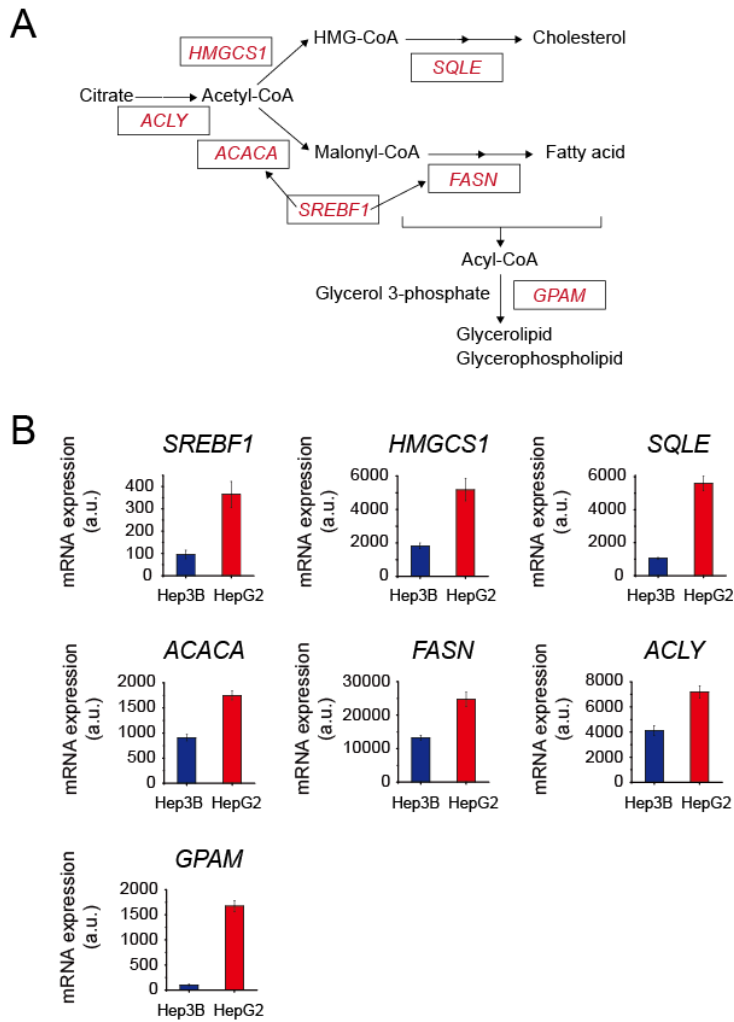
Figure 16. Major lipid synthesis pathways and individual genes

(A) Major metabolites and genes for various lipid synthesis pathways. (B) Differential expressions of individual genes in (A) from the GSE21955 dataset. The error bars represent standard deviations. Abbreviations: sterol regulatory element binding transcription factor 1 (*SREBF1)*, 3-hydroxy-3-methylglutaryl-CoA synthase 1 (*HMGCS1*), squalene epoxidase (*SQLE*), acetyl-CoA carboxylase alpha (*ACACA*), fatty acid synthase (*FASN*), ATP citrate lyase (*ACLY*), glycerol-3-phosphate acyltransferase, mitochondrial (*GPAM*).

C. Modulation of ACSS2 activity affects HepG2 phenotypes with high acetate usage

To study the phenotypic implication of the acetate metabolism, I carried out siRNA experiments. Lowering ACSS2 expression led to a significant decrease in the growth of HepG2 cells but not Hep3B cells (Fig. 17A). The knockdown also led to a decrease in ^{13}C-acetate incorporation into some of the metabolites that had exhibited higher incorporation in HepG2 (Fig. 17B). Importantly, the knockdown of ACSS2 reduced ^{13}C-acetate-derived de novo fatty acid synthesis and the lipid droplet content of HepG2 cells (Fig. 17C and D). Interestingly, the knockdown of ACSS2 increased lactate production from ^{13}C-glucose in HepG2 cells (Fig. 17E). As Hep3B cells are more glycolytic, ACSS2 downregulation may induce Hep3B-like metabolic states in HepG2 cells. Further knockdown of a master regulator of anabolism, *mTOR*, decreased the growth of HepG2 cells more than Hep3B cells, whereas knockdown of catabolic genes, *LDH* of glycolysis and *CPT1* of fatty acid oxidation, resulted in the opposite effects (Fig. 17F).

I also tested the effects of ACSS2 modulation on cells treated with an ACSS2-specific inhibitor [17]. In terms of metabolism, the inhibitor decreased de novo fatty acid synthesis from acetate in HepG2 cells (Fig. 17G). From a phenotypic viewpoint, it slowed the growth of HepG2 cells more than that of Hep3B cells (Fig. 17H), which is consistent with the knockdown results. This sensitivity of HepG2 was significantly weakened by a high concentration of acetate (4 mM) at normal glucose levels, which was not observed for the Hep3B cells. In comparison, lower glucose (1 mM) with 0.2 mM acetate did not affect the sensitivity of HepG2 cells, indicating HepG2's higher dependence on ACSS2 and lower dependence on glucose

availability. The latter is also consistent with HepG2's insensitivity to a glycolysis LDH inhibitor that effectively inhibited Hep3B cells (Fig. 17I). Similar to the siRNA results, the findings showed HepG2 cells were more sensitive to the mTOR inhibitor, while Hep3B cells were more sensitive to the CPT1 inhibitor (Fig. 17I). Therefore, these data corroborate the above isotope incorporation results and suggest that high-ACSS2 HepG2 cells are more highly dependent on acetate-driven anabolic lipid metabolism than Hep3B cells.
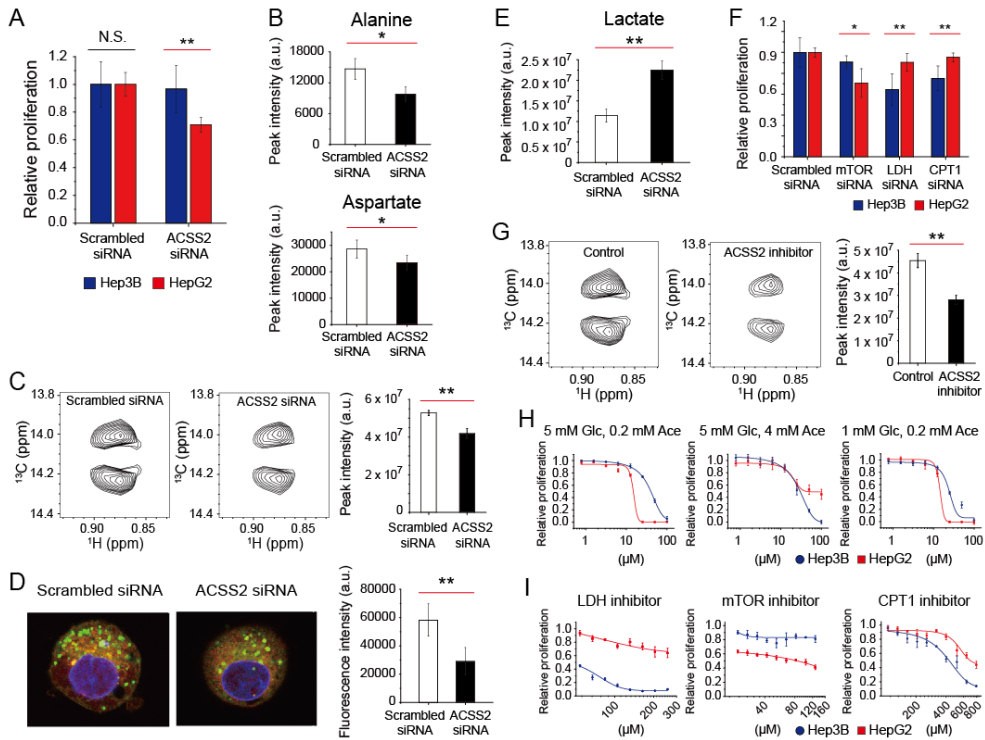
Figure 17. Modulation of ACSS2 affects phenotypes of high-ACSS2 HepG2

(A) Inhibition of cell growth by ACSS2 knockdown as measured with CCK8. (B) ^{13}C-alanine and ^{13}C-aspartate labeled with 1,2-$^{13}C_2$-acetate in HepG2 cells after ACSS2 knockdown was measured as in Fig. 14A. (C and D) Inhibition of fatty acid synthesis in HepG2 cells by ACSS2 knockdown, measured as described in Fig. 14B (C) and Fig. 14E (D). (E) ^{13}C-labeled lactate from 5 mM U-$^{13}C_6$-glucose in HepG2 cells upon ACSS2 knockdown, measured as described in Fig. 14A. (F) Inhibition of cell growth by knockdown of mTOR, LDH, and CPT1. (G) Inhibition of fatty acid synthesis from 0.2 mM 1,2-$^{13}C_2$-acetate in HepG2 cells by ACSS2 inhibitor (10 μM). (H and I) Cell growth inhibition by ACSS2 inhibitor (H), LDH inhibitor (galloflavin; I, left), mTOR inhibitor (Torin1; I, middle), and CPT1 inhibitor (etomoxir; I, right), as measured with CCK8. N.S.: not significant; *P < 0.05; **P < 0.01; (n = 3, unless

63

otherwise stated) from Student's *t*-test with standard deviations. Abbreviations: mammalian target of rapamycin (mTOR), lactate dehydrogenase (LDH), carnitine palmitoyltransferase 1 (CPT1).

D. High-ACSS2 HepG2 cells form anabolic and less malignant tumors in vivo

To validate the above results in vivo, I performed isotope tracing with ^{13}C-acetate or ^{13}C-glucose and phenotypic characterization using mouse orthotopic liver tumors derived from HepG2 or Hep3B cells. Compared with HepG2 tumors, U-^{13}C$_6$-glucose administration led to a much higher M+6 isotopomer ratio in Hep3B tumors, demonstrating their higher glucose uptake (Fig. 18A). However, the M+1, +2, and +3 isotopomers of glucose, formed only through the re-synthesis of glucose (gluconeogenesis), were higher in the HepG2 tumors, indicating that anabolic gluconeogenesis is more active in these tumors. In comparison, catabolic glycolytic activity was higher in Hep3B tumors than HepG2 tumors, as estimated by the M+3 lactate production from ^{13}C-glucose (Fig. 18B). Following ^{13}C-acetate administration, HepG2 tumors exhibited higher levels of ^{13}C incorporation into various amino acids (Fig. 18C) and glucose (Fig. 19). HepG2 tumors again showed greater incorporation of ^{13}C-acetate into fatty acids, as indicated by the high-molecular-weight isotopomers of palmitate (Fig. 18D).

Regarding cancer malignancy phenotypes, the tumor frequency, tumor sizes (Fig. 18E), and frequency of metastasis to either peritoneum or ascites (Fig. 18F) were all lower or smaller in the HepG2 tumors, showing that the acetate-using HepG2 cells were less tumorigenic and formed less malignant tumors. Consistent results were obtained in vitro using wound healing and clonogenic assays (Fig. 18G and H). In addition, "lower epithelial-mesenchymal transition" was the top biological process differentiating HepG2 from Hep3B cells according to hallmark gene set analysis (Fig. 20) [67]. Taken together, the in vivo results confirm that

acetate-using tumors with higher ACSS2 exhibit anabolic characteristics and lower malignancy.
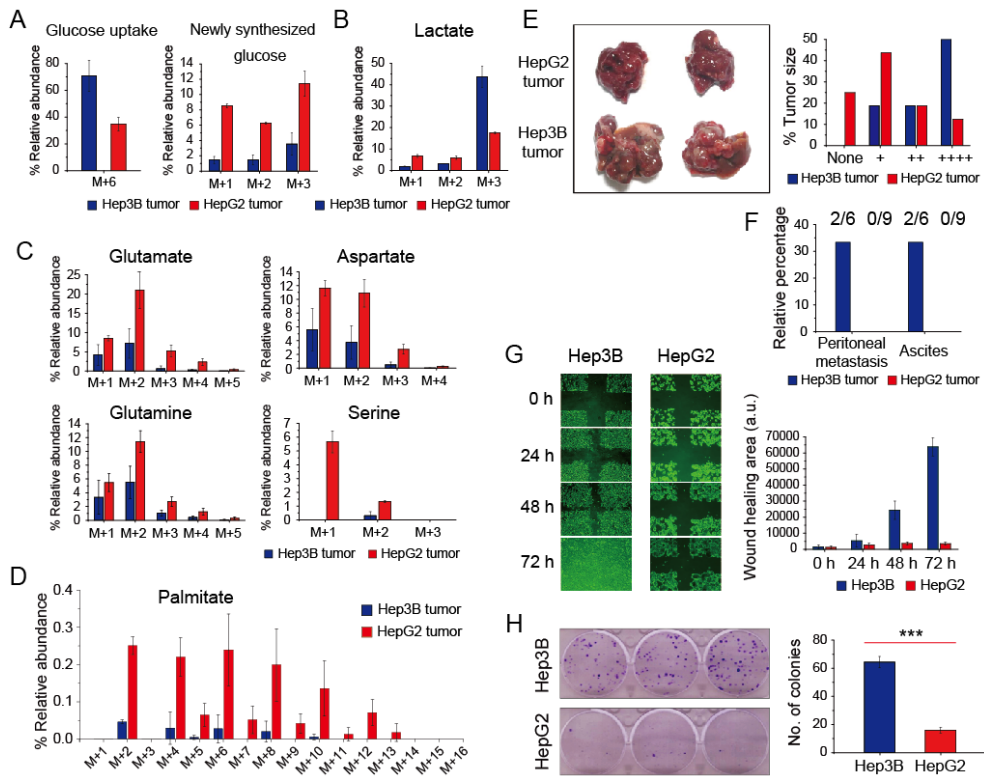
Figure 18. High-ACSS2 cells from anabolic and less malignant tumors of HepG2 and Hep3B orthotopic mouse liver xenograft models

(A) U-^{13}C$_6$-glucose uptake (left) and newly synthesized glucose (right) from the liver cancer tissues of mice orally administered 5 g/kg U-^{13}C$_6$-glucose, as measured with LC-MS. (B) ^{13}C-lactate generation from U-^{13}C$_6$-glucose in liver cancer tissues. (C) Isotopic incorporation into various metabolites in livers of mice fed 1,2-^{13}C$_2$-acetate (3 g/Kg), as measured with LC-MS. (D) Isotopic incorporations into palmitate from 1,2-^{13}C$_2$-acetate in liver tissues, as measured with LC-MS. (E) Representative mouse liver tumors (left) and the tumor size distribution (right) after 2 months (number of + signs: overall visible sizes). (F) The frequency of peritoneal or ascites metastasis. (G and H) Scratch wound healing (G) and clonogenic (H) assays for Hep3B and

HepG2 cells (left) and their image quantitation and colony numbers (right). ***P <

0.001 (n = 3, unless otherwise stated) from Student's *t*-test with standard deviations.
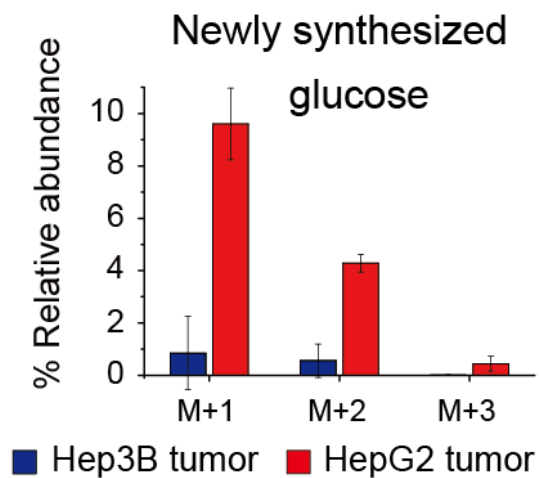
Figure 19. Newly synthesized glucose in liver cancer tissues of mice

Mice were orally administered 3 g/kg 1,2-$^{13}C_2$-acetate. Glucose isotopomers were measured with LC-MS.
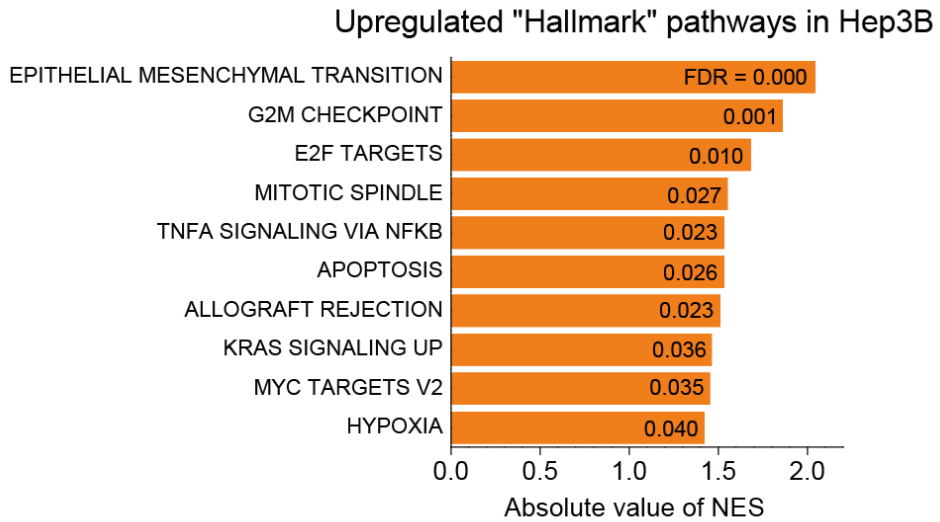
Figure 20. Top 10 "Hallmark" pathways upregulated in Hep3B cell line compared with HepG2 cell line from GSE21955 dataset

The pathways were ordered by absolute value of Normalized Enrichment Score (NES) in GSEA. The "Hallmark" pathways were retrieved from the Molecular Signatures Database (MSigDB).

E. Clinical manifestation of high- and low-ACSS2 cancer patients

To form a picture of ACSS2 expression during the course of human liver tumorigenesis, I compared the ACSS2 levels of tissues from normal, cirrhosis, hepatocellular carcinoma, and metastatic liver cancer patients. Immunohistochemical staining showed that ACSS2 levels were significantly higher in normal tissues than hepatocellular carcinoma and metastatic liver cancer tissues (Fig. 21A and B), indicating that ACSS2 level is lower in malignant tumors than normal tissue.

Then, the ACSS2-malignancy relationship was further tested using a larger TCGA liver cancer cohort. ACSS2 expression was found to be higher in the lower-grade tumors (grade I and II) than the higher-grade tumors (grade III and IV) (Fig. 21C). Patients with cancer recurrence and/or progression had lower ACSS2 levels than those that achieved a disease-free status (Fig. 21D). Furthermore, the high-ACSS2 group had significantly longer progression-free intervals (PFI) and disease-free intervals (DFI) (Fig. 21E and F) when I analyzed similarly-sized high- and low-ACSS2 groups at the 2352 RSEM cut-off value. Initial analysis of patient survival using this cut-off value did not reveal significant differences. A relationship between high-ACSS2 and higher liver tumor burden was previously observed in mouse models but not in humans [17]. Therefore, I re-analyzed the patient data with the best risk separation approach [66] and found a close and highly significant association. It found a subset of the low-ACSS2 patient group belonging in the lower ~13th percentile of the ACSS2 expression levels, which was thus classified as a "very-low" ACSS2 group (13VLA group). Compared with the other 87% group (the rest group),

this 13VLA group exhibited particularly poor prognoses for all available survival-related variables (Fig. 21G through J): overall survival (OS), disease-specific survival (DSS), DFI, and PFI. The results were confirmed in another large, independent cohort (GSE76427), where patients in the lower ~17th percentile exhibited much shorter OS and relapse-free survival (RFS) (Fig. 21K and L). Consistent results, showing lower ACSS2 levels in malignant tumors than in normal tissue, were also obtained in a chemically induced rat liver cancer model (Fig. 22). In comparison, ACSS1 levels, which were found to be elevated in a high malignancy group in a previous report (~30% of the cohort) [59], were the same between the 13VLA and the rest groups (Fig. 23). Overall, these confirm the link between lower ACSS2 expression and higher-malignancy liver cancer at the human level.
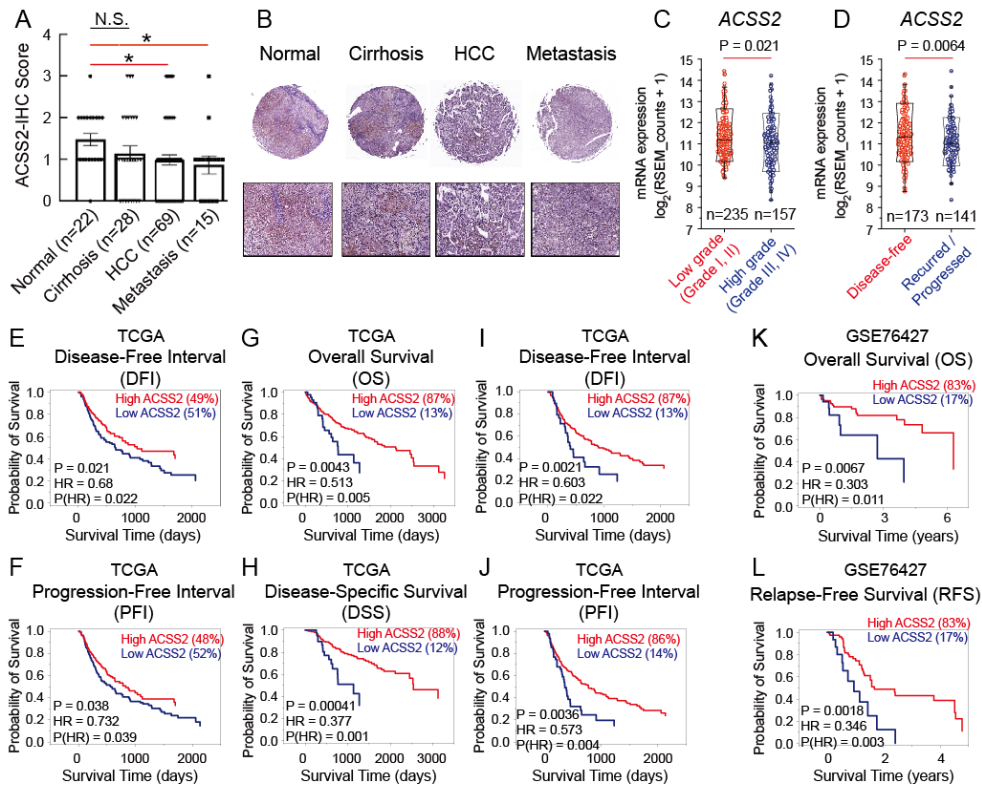
Figure 21. Clinical manifestation of high and low-ACSS2 liver cancer patients

(A and B) Immunohistochemistry of ACSS2 in human liver tissue microarray. (A) Staining intensity grading was as follows: none, 0; weak, 1+ (< 30%); moderate, 2 (+30–60%); and strong, 3+ (> 60%). N.S.: not significant; *P < 0.05 (n = 3, unless otherwise stated) from Student's *t*-test with standard deviations. (B) Representative images. (C and D) *ACSS2* mRNA expression levels in low- (I and II) vs. high- (III and IV) grade tumors (C) or disease-free vs. recurred/progressed patients (D) in the TCGA LIHC cohort. (E through J) Kaplan-Meier analysis of prognostic variables for patients from the TCGA LIHC cohort. (E and F). DFI and PFI curves based on the 2352 RSEM cut-off. (G, H, I, and J) OS (G), DSS (H), DFI (I), and PFI (J) for the low-ACSS2 (13VLA) and high-ACSS2 (the rest) groups. HR: hazard ratio. (K and

L) OS (K) and RFS (L) curves for the bottom 17% and top 83% of ACSS2 levels in the GSE76427 dataset.
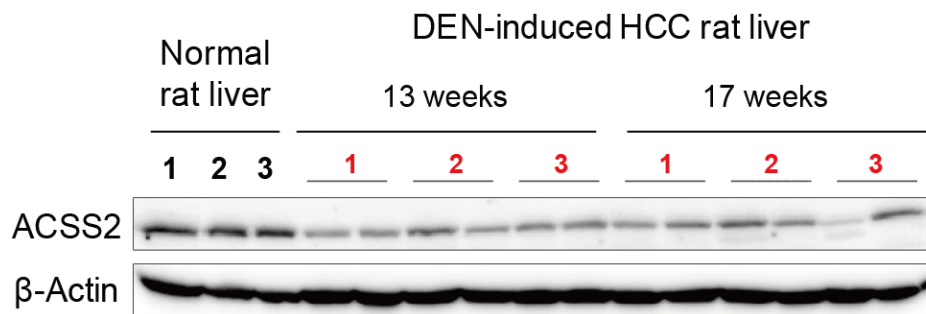
Figure 22. ACSS2 protein expression in liver tissues of normal and N-nitrosodiethylamine (DEN)-induced hepatocellular carcinoma (HCC) rats

Western blotting was used to show relative ACSS2 and β-actin control protein expression in liver tissues of normal and DEN-induced HCC rats 13 and 17 weeks post-treatment.
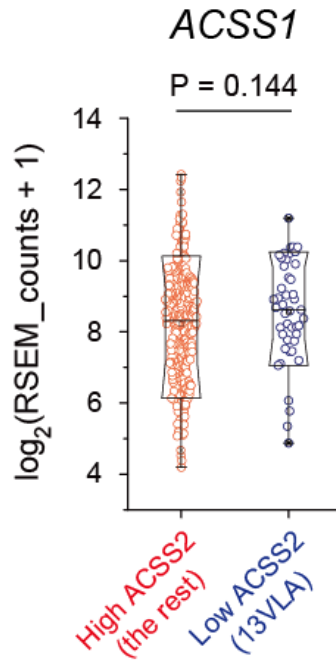
Figure 23. Acetyl-CoA synthetase 1 (*ACSS1*) mRNA expression between 13VLA and the rest groups of the TCGA LIHC cohort

F. Metabolic characteristics of high- and low-ACSS2 human liver cancer

I used the gene expression profiles of the high- and low-ACSS2 groups to investigate their metabolic characteristics. GSEA analysis of the TCGA cohort showed that gene sets for anabolic lipid metabolism are significantly elevated in the high-ACSS2 patient group, as defined by the 2352 RSEM cut-off value (Fig. 24A). At individual gene levels, the expressions of key genes in the lipid anabolic pathways, *SREBF1, SREBF2, HMGCS1, HMGCS2, FASN, ACACA, ACLY*, and *GPAM*, were shown to be consistently upregulated in the high-ACSS2 group (Fig. 24B). Very similarly, significant differences in anabolic lipid metabolism were also observed between the 13VLA group and the rest (Fig. 25A and B). Interestingly, for the 13VLA group, the expressions of key genes in glycolytic pathways, such as *LDH, HK,* and *PFK,* were significantly upregulated compared to the rest group, indicating high glucose catabolism (Fig. 25C), which is consistent with the results from cell and animal models. Previously, hypoxia was suggested to induce ACSS expression, higher acetate usage, and higher malignancy in several cancers, including liver cancer [18, 58]. In contrast, my analysis found significant negative correlations between *ACSS2* and a well-established hypoxia score (Fig. 25D) [68], suggesting that high-ACSS2 levels are associated with lower hypoxia. Indeed, the hypoxia score was significantly elevated in the 13VLA group compared with the rest group (Fig. 25E).

Next, the 13VLA and the rest groups were analyzed for DNA promoter methylation, which has important implications in liver cancer carcinogenesis and prognosis [69, 70]. Strikingly, the promoter sites in the *ACSS2* and *FASN* genes

ranked among the top 20 (among ~390,000) differentially methylated sites between the two groups (Fig. 25F). Specifically, the site at a CpG shore of the *ACSS2* promoter (specific for the cg09801828 probe) exhibited significantly higher methylation in the 13VLA group than the other groups (Fig. 25G), suggesting DNA methylation has roles in ACSS2 suppression. Overall, these patient data analyses show that high-ACSS2 expression is associated with lipid anabolic characteristics, reduced glycolysis, and lower hypoxia and malignancy, confirming my cell and animal level results.
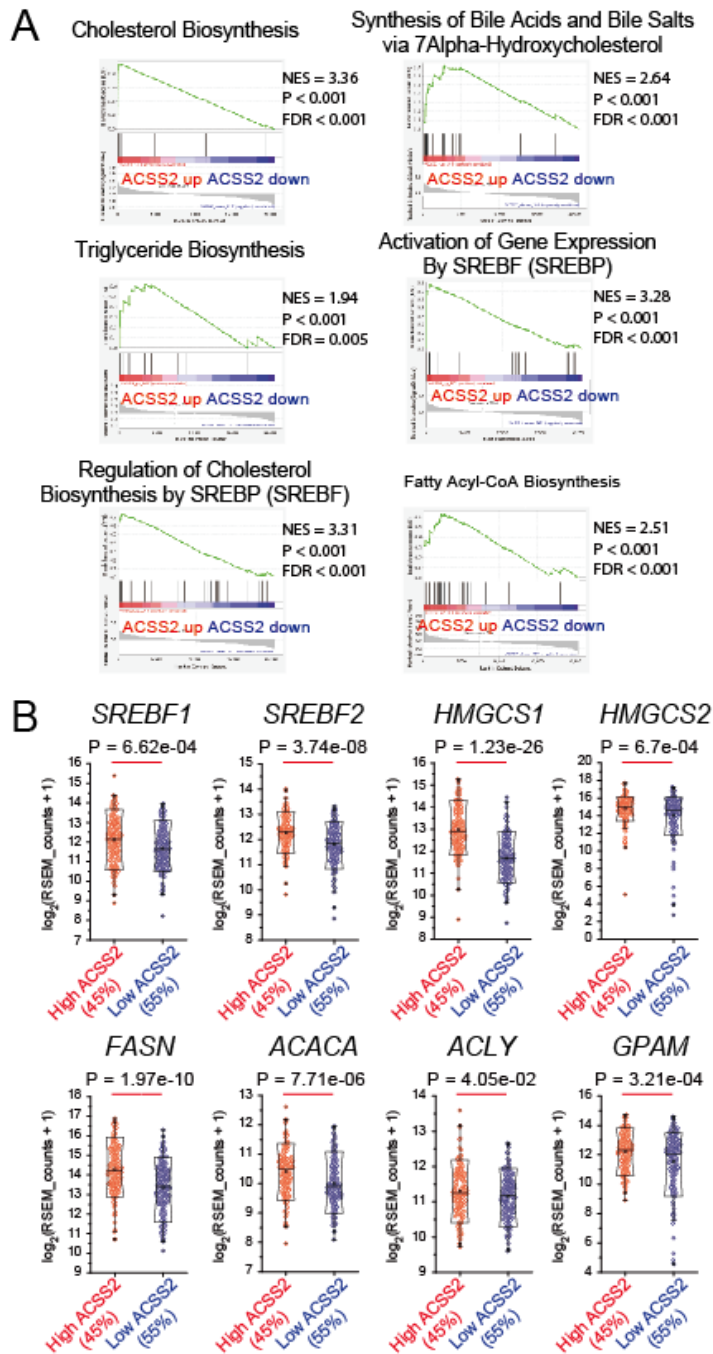
Figure 24. Comparison of metabolic characteristics between the two groups according to 2352 RSEM cut-off value

(A) GSEA results for lipid-related pathways between the groups according to the 2352 RSEM cut-off value. NES, Normalized Enrichment Score; FDR, False Discovery Rate. (B) mRNA expressions of some key genes of lipid anabolic pathways in the groups according to the 2352 RSEM cut-off value. Abbreviations: sterol regulatory element binding transcription factor 1/2 (*SREBF1/2*), 3-hydroxy-3-methylglutaryl-CoA synthase 1/2 *(HMGCS1/2)*, fatty acid synthase (*FASN*), acetyl-CoA carboxylase alpha (*ACACA*), ATP citrate lyase (*ACLY*), glycerol-3-phosphate acyltransferase, mitochondrial (*GPAM*).
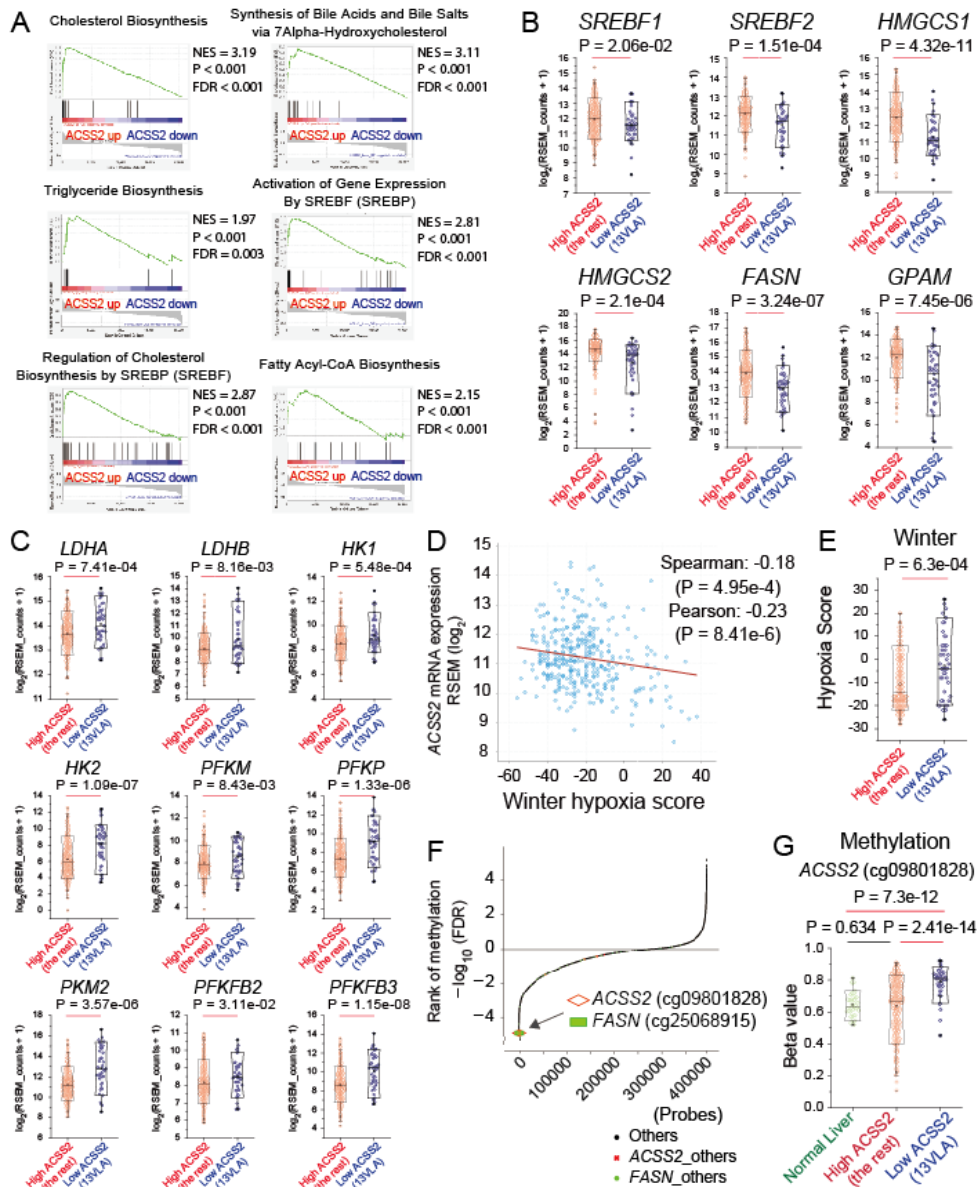
Figure 25. Metabolic characteristics of high- and low-ACSS2 human liver cancer

(A) GSEA results for lipid-related pathways in the 13VLA and the rest groups. NES, Normalized Enrichment Score; FDR, False Discovery Rate. (B) mRNA expressions of some key genes in the lipid anabolic pathways in the 13VLA and the rest groups. (C) mRNA expressions levels for key glycolysis genes in the 13VLA and the rest

81

groups. (D) Correlation between the *ACSS2* expression and the Winter hypoxia score for the entire TCGA LIHC cohort. (E) Winter hypoxia scores in the 13VLA and the rest groups. (F) The differential methylation rank plot between the 13VLA group and the rest. Approx. 390,000 methylation probes (sites) were ranked according to the FDR values. (G) The methylation beta values for the normal, 13VLA, and the rest groups of the TCGA LIHC cohort. Abbreviations: sterol regulatory element binding transcription factor 1/2 (*SREBF1/2*), 3-hydroxy-3-methylglutaryl-CoA synthase 1/2 (*HMGCS1/2*), fatty acid synthase (*FASN*), glycerol-3-phosphate acyltransferase, mitochondrial (*GPAM*), lactate dehydrogenase A/B (*LDHA/B*), hexokinase 1/2 (*HK1/2*), phosphofructokinase, muscle (*PFKM*), phosphofructokinase, platelet (*PFKP*), pyruvate kinase M2 (*PKM2*), 6-phosphofructo-2-kinase/fructose-2,6-biphosphatase 2/3 (*PFKFB2/3*).

G. PET-CT imaging of low- and high-grade liver cancer patients

To directly assess the metabolite-malignancy relationship in living human patients, PET-CT data with ^{11}C-acetate and ^{18}F-fluorodeoxyglucose (^{18}F-FDG) and tumor grades were analyzed. I found much higher ^{11}C-acetate with little ^{18}F-FDG uptake in patients with lower-grade (grade II) liver cancer, whereas there was little ^{11}C-acetate but prominent ^{18}F-FDG uptake in higher-grade hepatocellular carcinoma patients (grade III) (Fig. 26A and B, Fig. 27A and B for the other eight cases). Metabolic stress due to a low blood supply, such as hypoxia or nutrient depletion, would have affected the uptake of acetate and FDG to a similar extent. Nevertheless, the selective uptake of either acetate or glucose in the imaging results seems to suggest low blood supply is not a requisite for acetate uptake. Therefore, acetate uptake seems to be an inherent property of lower-grade liver cancer. These clinical human data confirm that the relationship between high acetate uptake and low malignancy is independent of metabolic stress.
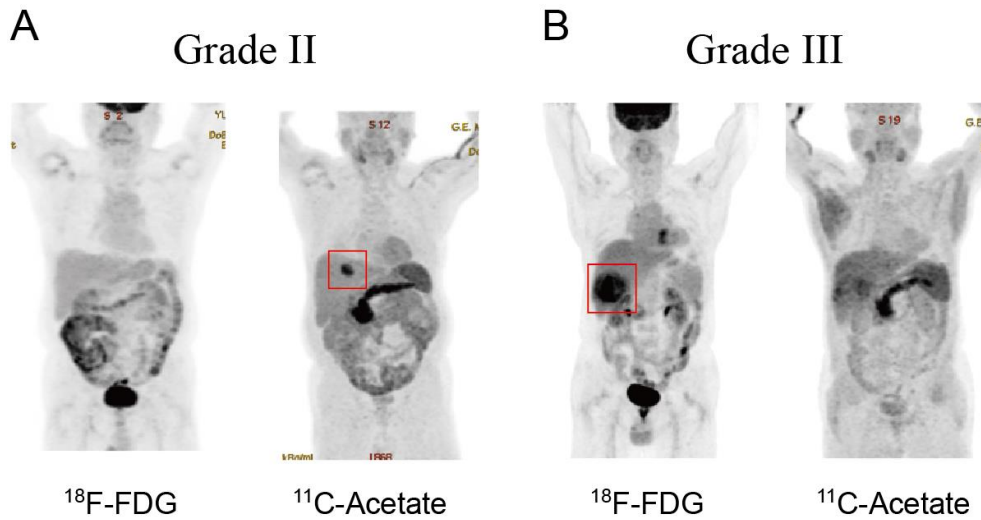
Figure 26. PET-CT imaging of low- and high-grade liver cancer patients

(A and B) Representative PET-CT images in a low- (grade II) (A) and a high-grade (grade III) (B) liver cancer patients, each of whom was monitored by both ^{18}F-FDG and ^{11}C-acetate (See Fig. 27A and B for data from eight more patients). Cancerous regions are marked with red boxes.
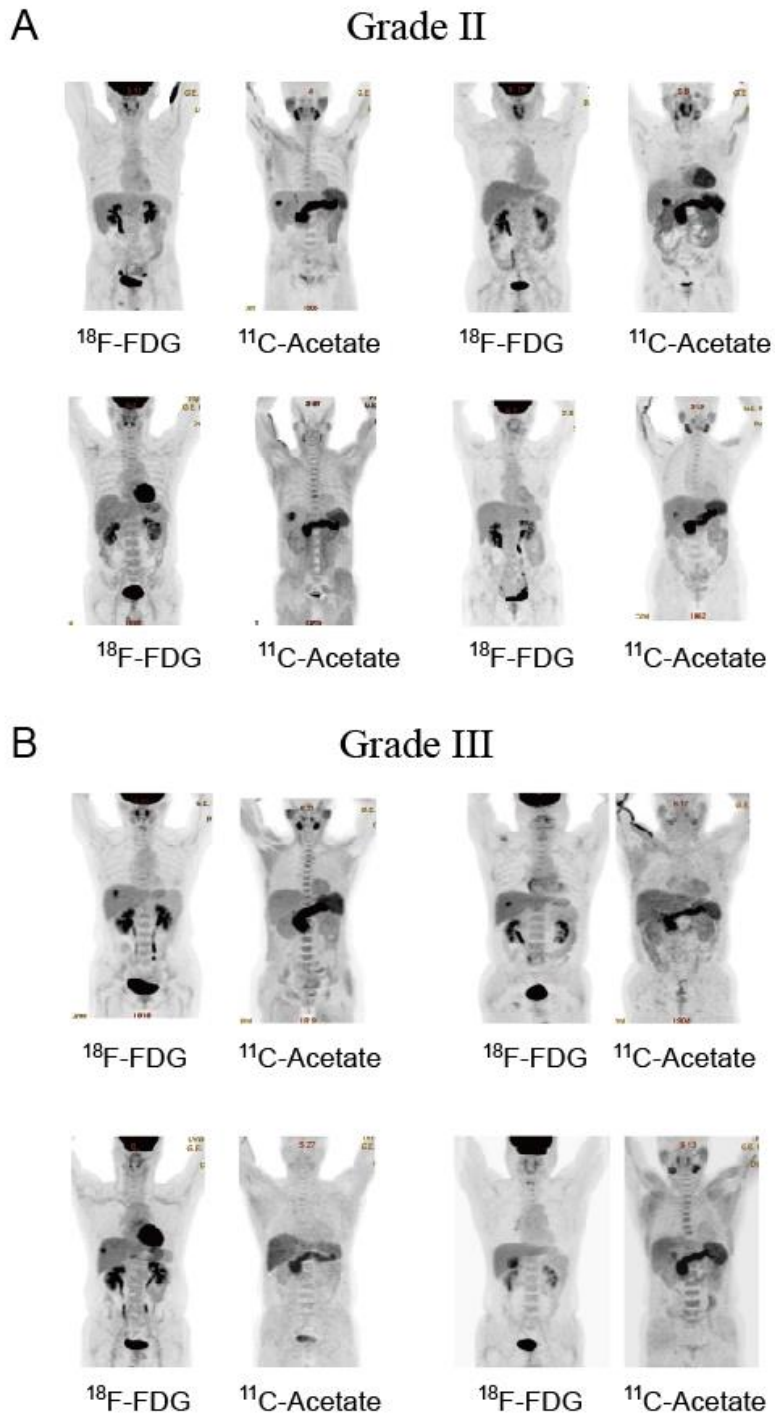
Figure 27. PET-CT imaging of additional patients

(A and B) PET-CT imaging of low- (A) and high- (B) grade liver cancer patients.

IV. Discussion

Despite prominent studies suggesting that acetate usage is limited to nutrient-depleted or hypoxic conditions [17, 18], and that there is a link between high ACSS2/acetate usage and enhanced cancer malignancy [15, 64], their generalization may require cautions. Conceptually, nutrient depletion occurs because of a low blood supply that may actually limit acetate availability. Indeed, my cell, animal, and patient studies consistently showed that high acetate uptake/ACSS2 expression can occur in glucose- or nutrient-replete conditions for lower-grade liver cancer cells or tumors that feature reduced hypoxia. In addition, hypoxia generally activates glycolytic activity and is associated with a higher malignancy [60, 61]. Enhanced glycolytic metabolism may reduce acetate usage and, therefore, the link between acetate uptake and higher malignancy may not be universal, either. In fact, in colorectal cancer patients, a lower acetate uptake was attributed to a higher malignancy [71]. ACSS2 levels are generally high in normal human liver tissues [72, 73], and it has been noted that ACSS2 is not induced, but maintained in high-ACSS2 liver cancer, and only lost in low-ACSS2 cancer [17]. Based on my results and the established roles of ACSS2 in acetate usage [15, 74, 75], ACSS2-driven high acetate uptake seems to be an inherent property of normal livers that may be slightly lost, if at all, in low malignancy liver cancer and largely lost in high malignancy liver cancer.

In a mostly bioinformatics study, high acetate uptake through ACSS1 under hypoxia was proposed for their iHCC3 group with shorter patient survival, hence higher malignancy [59]. Unfortunately, the effect of hypoxia was not explicitly addressed for ACSS1 or ACSS2 in their experimental model, HepG2 cells.

Interestingly, though, I was able to find high ACSS2 level in their iHCC1 group, with the lowest malignancy and longest survival [59], which is consistent with my overall results. Yet another study performed the knockdown of ACSS2 in liver cancer cells, but in a high-malignancy cell line with lower ACSS2 levels (MHCC97H) rather than a lower-malignancy cell line with higher ACSS2 levels (MHCC97L) [76], making it difficult to compare the results with ours. From my results, the knockdown of ACSS2 in HepG2 cells induced higher glycolytic lactate production, and the 13VLA patients featured upregulation of glycolytic genes. Therefore, ACSS2 loss seems to occur concomitantly with enhanced glycolysis. This may render the cancer cells more malignant, more viable under hypoxia, and more Warburg-type, and again this is consistent with my PET-CT results. It is tempting to speculate that ACSS2 may have an inhibitory role for glycolysis, which may be an interesting future study topic.

There are noteworthy translational implications of our results. First, the PET-CT-detectable metabotypes of ACSS2-driven acetate uptake may be used as non-invasive biomarkers for lower-malignancy liver cancer. The use of both ^{11}C-acetate and ^{18}F-FDG may overcome the unacceptably high false-negative rate (40~50%) of single ^{18}F-FDG imaging [63] and could also help to discriminate between acetate-using (acetophilic) and glycolytic (glucophilic) liver cancers. In comparison, previously developed biomarkers based on transcriptomics or genetics [70, 77, 78] require invasive biopsies. Second, for patient stratifications, the metabolic patterns of the 13VLA group, which had particularly poor prognoses, were not apparent in earlier stratification studies. Hoshida et al. [77] found that the most malignant tumor group (S1) constituted 25~33% of the cohort. Two major subtypes (proliferation and nonproliferation classes), each comprising about 50%, were found

by analyzing many previous studies [78]. In an omics-based study [70], about 33% of the cohort (iClust1 group) was found to have higher-grade tumors with poor prognoses. In a bioinformatics study, the iHCC3 group, comprising about 28% of the cohort, exhibited a shorter survival time with high glycolytic and fatty acid synthetic gene expression [59]. Therefore, the 13VLA group seems to constitute a smaller proportion (~13%) of patients with distinct metabolic characteristics and, thus, is proposed as a new subset with the poorest prognosis among the poor prognosis groups. Third, systemic chemotherapy for liver cancer is recommended only for advanced-stage patients (BCLC stage C) [79] who tend to exhibit high histologic grades [80]. However, ACSS2 inhibitors [81] might be particularly helpful for patients in the acetophilic group with lower-grade tumors, who have been conventionally treated with more invasive modalities [79]. The benefits may be significant, as the better prognosis group comprises at least ~50% of patients [59, 77, 78]. For the glucophilic group, such as the 13VLA group, glycolysis inhibitors may be useful [82].

In summary, I suggest there are associations among high acetate use, anabolic characteristics, and low malignancy for liver cancer, based on comprehensive studies on cell, animal, and human systems. I also identified a particularly poor prognostic patient group with very low ACSS2 expression and glycolytic characteristics. My results may help to stratify liver cancer patients and choose the best treatment options.

4. Conclusions

This research investigated the relationship between acetate metabolism and cancer in terms of acquired resistance to cancer drug and changes in tumor grade. Live metabolomics and biochemical approaches have shown that a bypass is activated in the fatty acid synthesis pathway in cisplatin-resistant bladder cancer cells. The well-known fatty acid synthesis pathway uses ACLY via citrate in mitochondria, but a new pathway requiring ACSS2 is believed to be activated in cisplatin-resistant cells. Isotope tracing showed that glucose-derived endogenous acetate is the preferred two-carbon source for fatty acid synthesis in cisplatin-resistant cells. This was verified by determining the correlation between ACSS2 expression levels and resistance to cisplatin treatment in the tissues of bladder cancer patients. Therefore, it was found that glucose-derived acetate metabolism contributes to the acquisition of cisplatin resistance by activating a new fatty acid synthesis pathway using ACSS2 in bladder cancer patients.

Integrative research methods using cellular, animal, and human systems showed differences in acetate metabolism according to tumor grade in liver cancer. Previous studies have shown that acetate metabolism is induced during nutrient deficiency or hypoxia. However, the active use of acetate in the livers of normal mice showed that nutrient deficiency was not a prerequisite for acetate use. Acetate uptake and metabolism were different in liver cancer cells, and the mouse xenograft model of these cells showed that acetate metabolism was related to tumor grade. These observations suggested that higher ACSS2 expression and acetate metabolism were associated with lower malignancy in liver cancer. In two independent large patient

cohorts, the group with higher ACSS2 expression also had a good prognosis for various survival-related variables. Through bioinformatics analysis, the 13VLA group with extremely low ACSS2 expression could be designated as the worst subset, even within the poor prognosis group. The reduction in ACSS2 made liver cancer cells more malignant, more viable under hypoxia, and more Warburg-type, and these features were consistent with PET-CT results in liver cancer patients. Therefore, acetate metabolism seems to be an inherent property of the liver, which is associated with low malignancy grades in liver cancer; the prognosis worsens as acetate metabolism declines in high malignancy grades. Overall, acetate metabolism features can be applied to the stratification and prognoses of bladder and liver cancer patients, may lead to the discovery of new targets, and may aid clinicians in selecting the best treatment options.

References

1. Gonzalez-Dominguez R, Gonzalez-Dominguez A, Segundo C, Schwarz M, Sayago A, Mateos RM, et al. High-Throughput Metabolomics Based on Direct Mass Spectr ometry Analysis in Biomedical Research. *Methods Mol Biol* **2019**;1978:27-38.

2. Jang C, Chen L, Rabinowitz JD. Metabolomics and Isotope Tracing. *Cell* **2018**;173(4):822-837.

3. Larive CK, Barding GA, Jr., Dinges MM. NMR spectroscopy for metabolomics and metabolic profiling. *Anal Chem* **2015**;87(1):133-146.

4. Lei Z, Huhman DV, Sumner LW. Mass spectrometry strategies in metabolomics. *J Biol Chem* **2011**;286(29):25435-25442.

5. Zhang A, Sun H, Wang P, Han Y, Wang X. Modern analytical techniques in metabolomics analysis. *Analyst* **2012**;137(2):293-300.

6. Lin P, Lane AN, Fan TW. Stable Isotope-Resolved Metabolomics by NMR. *Methods Mol Biol* **2019**;2037:151-168.

7. Wishart DS. Metabolomics for Investigating Physiological and Pathophysiological Processes. *Physiol Rev* **2019**;99(4):1819-1875.

8. Warburg O. On the origin of cancer cells. *Science* **1956**;123(3191):309-314.

9. DeBerardinis RJ, Chandel NS. Fundamentals of cancer metabolism. *Sci Adv* **2016**;2(5):e1600200.

10. O'Connell TM. Recent advances in metabolomics in oncology. *Bioanalysis* **2012**;4(4):431-451.

11.   Carracedo A, Cantley LC, Pandolfi PP. Cancer metabolism: fatty acid oxidation in the limelight. *Nat Rev Cancer* **2013**;13(4):227-232.

12.   Luengo A, Gui DY, Vander Heiden MG. Targeting Metabolism for Cancer Therapy. *Cell Chem Biol* **2017**;24(9):1161-1180.

13.   Bose S, Ramesh V, Locasale JW. Acetate Metabolism in Physiology, Cancer, and Beyond. *Trends Cell Biol* **2019**;29(9):695-703.

14.   Schug ZT, Vande Voorde J, Gottlieb E. The metabolic fate of acetate in cancer. *Nat Rev Cancer* **2016**;16(11):708-717.

15.   Mashimo T, Pichumani K, Vemireddy V, Hatanpaa KJ, Singh DK, Sirasanagandla S, et al. Acetate is a bioenergetic substrate for human glioblastoma and brain metastases. *Cell* **2014**;159(7):1603-1614.

16.   Medes G, Friedmann B, Weinhouse S. Fatty acid metabolism. VIII. Acetate metabolism in vitro during hepatocarcinogenesis by p-dimethylaminoazobenzene. *Cancer Res* **1956**;16(1):57-62.

17.   Comerford SA, Huang Z, Du X, Wang Y, Cai L, Witkiewicz AK, et al. Acetate dependence of tumors. *Cell* **2014**;159(7):1591-1602.

18.   Schug ZT, Peck B, Jones DT, Zhang Q, Grosskurth S, Alam IS, et al. Acetyl-CoA synthetase 2 promotes acetate utilization and maintains cancer cell growth under metabolic stress. *Cancer Cell* **2015**;27(1):57-71.

19.   Gao X, Lin SH, Ren F, Li JT, Chen JJ, Yao CB, et al. Acetate functions as an epigenetic metabolite to promote lipid synthesis under hypoxia. *Nat Commun* **2016**;7:11960.

20.   Jaworski DM, Namboodiri AM, Moffett JR. Acetate as a Metabolic and Epigenetic Modifier of Cancer Therapy. *J Cell Biochem* **2016**;117(3):574-588.

21. Kiemeney LA, Witjes JA, Verbeek AL, Heijbroek RP, Debruyne FM. The clinical epidemiology of superficial bladder cancer. *Br J Cancer* **1993**;67(4):806-812.

22. Borden LS, Jr., Clark PE, Hall MC. Bladder cancer. *Curr Opin Oncol* **2003**;15(3):227-233.

23. Hall MC, Chang SS, Dalbagni G, Pruthi RS, Seigne JD, Skinner EC, et al. Guideline for the management of nonmuscle invasive bladder cancer (stages Ta, T1, and Tis): 2007 update. *J Urol* **2007**;178(6):2314-2330.

24. Babjuk M, Oosterlinck W, Sylvester R, Kaasinen E, Bohle A, Palou-Redorta J, et al. EAU guidelines on non-muscle-invasive urothelial carcinoma of the bladder. *Eur Urol* **2008**;54(2):303-314.

25. Stenzl A, Cowan NC, De Santis M, Kuczyk MA, Merseburger AS, Ribal MJ, et al. Treatment of muscle-invasive and metastatic bladder cancer: update of the EAU guidelines. *Eur Urol* **2011**;59(6):1009-1018.

26. Black PC, Dinney CP. Growth factors and receptors as prognostic markers in urothelial carcinoma. *Curr Urol Rep* **2008**;9(1):55-61.

27. Cohen SM, Lippard SJ. Cisplatin: from DNA damage to cancer chemotherapy. *Prog Nucleic Acid Res Mol Biol* **2001**;67:93-130.

28. Santos NAG, Catao CS, Martins NM, Curti C, Bianchi MLP, Santos AC. Cisplatin-induced nephrotoxicity is associated with oxidative stress, redox state unbalance, impairment of energetic metabolism and apoptosis in rat kidney mitochondria. *Arch Toxicol* **2007**;81(7):495-504.

29. Siddik ZH. Cisplatin: mode of cytotoxic action and molecular basis of resistance. *Oncogene* **2003**;22(47):7265-7279.

30.   Viale A, Draetta GF. Metabolic Features of Cancer Treatment Resistance. *Recent Results Cancer Res* **2016**;207:135-156.

31.   Kwon HN, Kim M, Wen H, Kang S, Yang HJ, Choi MJ, et al. Predicting idiopathic toxicity of cisplatin by a pharmacometabonomic approach. *Kidney Int* **2011**;79(5):529-537.

32.   Pan X, Wilson M, Mirbahai L, McConville C, Arvanitis TN, Griffin JL, et al. In vitro metabonomic study detects increases in UDP-GlcNAc and UDP-GalNAc, as early phase markers of cisplatin treatment response in brain tumor cells. *J Proteome Res* **2011**;10(8):3493-3500.

33.   Sullivan LB, Gui DY, Heiden MGV. Altered metabolite levels in cancer: implications for tumour biology and cancer therapy. *Nat Rev Cancer* **2016**;16(11):680-693.

34.   Yoshii Y, Furukawa T, Saga T, Fujibayashi Y. Acetate/acetyl-CoA metabolism associated with cancer fatty acid synthesis: overview and application. *Cancer Lett* **2015**;356(2 Pt A):211-216.

35.   Jin X, Yun SJ, Jeong P, Kim IY, Kim WJ, Park S. Diagnosis of bladder cancer and prediction of survival by urinary metabolomics. *Oncotarget* **2014**;5(6):1635-1645.

36.   Lin L, Huang Z, Gao Y, Chen Y, Hang W, Xing J, et al. LC-MS-based serum metabolic profiling for genitourinary cancer classification and cancer type-specific biomarker discovery. *Proteomics* **2012**;12(14):2238-2246.

37.   Putluri N, Shojaie A, Vasu VT, Vareed SK, Nalluri S, Putluri V, et al. Metabolomic profiling reveals potential markers and bioprocesses altered in bladder cancer progression. *Cancer Res* **2011**;71(24):7376-7386.

38.   Huang Z, Lin L, Gao Y, Chen Y, Yan X, Xing J, et al. Bladder cancer determination via two urinary metabolites: a biomarker pattern approach. *Mol Cell Proteomics* **2011**;10(10):M111 007922.

39.   Kim WT, Kim J, Yan C, Jeong P, Choi SY, Lee OJ, et al. S100A9 and EGFR gene signatures predict disease progression in muscle invasive bladder cancer patients after chemotherapy. *Ann Oncol* **2014**;25(5):974-979.

40.   Lee MY, Yeon A, Shahid M, Cho E, Sairam V, Figlin R, et al. Reprogrammed lipid metabolism in bladder cancer with cisplatin resistance. *Oncotarget* **2018**;9(17):13231-13243.

41.   Wen H, Xu WJ, Jin X, Oh S, Phan CH, Song J, et al. The roles of IP3 receptor in energy metabolic pathways and reactive oxygen species homeostasis revealed by metabolomic and biochemical studies. *Biochim Biophys Acta* **2015**;1853(11 Pt A):2937-2944.

42.   Wen H, An YJ, Xu WJ, Kang KW, Park S. Real-time monitoring of cancer cell metabolism and effects of an anticancer agent using 2D in-cell NMR spectroscopy. *Angew Chem Int Ed Engl* **2015**;54(18):5374-5377.

43.   Lee S, Wen H, An YJ, Cha JW, Ko YJ, Hyberts SG, et al. Carbon Isotopomer Analysis with Non-Unifom Sampling HSQC NMR for Cell Extract and Live Cell Metabolomics Studies. *Anal Chem* **2017**;89(2):1078-1085.

44.   Amoedo ND, Obre E, Rossignol R. Drug discovery strategies in the field of tumor energy metabolism: Limitations by metabolic flexibility and metabolic resistance to chemotherapy. *Biochim Biophys Acta* **2017**;1858(8):674-685.

45.   Zaidi N, Swinnen JV, Smans K. ATP-citrate lyase: a key player in cancer metabolism. *Cancer Res* **2012**;72(15):3709-3714.

46.   Rohrig F, Schulze A. The multifaceted roles of fatty acid synthesis in cancer. *Nat Rev Cancer* **2016**;16(11):732-749.

47.   Elliott KA, Greig ME. The metabolism of lactic and pyruvic acids in normal and tumour tissues: The formation of succinate. *Biochem J* **1937**;31(7):1021-1032.

48.   Kornacker MS, Lowenstein JM. Citrate and the Conversion of Carbohydrate into Fat. The Activities of Citrate-Cleavage Enzyme and Acetate Thiokinase in Livers of Starved and Re-Fed Rats. *Biochem J* **1965**;94:209-215.

49.   Xu WJ, Wen H, Kim HS, Ko YJ, Dong SM, Park IS, et al. Observation of acetyl phosphate formation in mammalian mitochondria using real-time in-organelle NMR metabolomics. *Proc Natl Acad Sci U S A* **2018**;115(16):4152-4157.

50.   Mullen AR, Wheaton WW, Jin ES, Chen PH, Sullivan LB, Cheng T, et al. Reductive carboxylation supports growth in tumour cells with defective mitochondria. *Nature* **2012**;481(7381):385-388.

51.   Morita M, Sato T, Nomura M, Sakamoto Y, Inoue Y, Tanaka R, et al. PKM1 Confers Metabolic Advantages and Promotes Cell-Autonomous Tumor Cell Growth. *Cancer Cell* **2018**;33(3):355-367 e357.

52.   Peetla C, Vijayaraghavalu S, Labhasetwar V. Biophysics of cell membrane lipids in cancer drug resistance: Implications for drug transport and drug delivery with nanoparticles. *Adv Drug Deliv Rev* **2013**;65(13-14):1686-1698.

53.   Rysman E, Brusselmans K, Scheys K, Timmermans L, Derua R, Munck S, et al. De novo lipogenesis protects cancer cells from free radicals and chemotherapeutics by promoting membrane lipid saturation. *Cancer Res* **2010**;70(20):8117-8126.

54.   Liu H, Liu Y, Zhang JT. A new mechanism of drug resistance in breast

cancer cells: fatty acid synthase overexpression-mediated palmitate overproduction. *Mol Cancer Ther* **2008**;7(2):263-270.

55.   Zhang J, Pavlova NN, Thompson CB. Cancer cell metabolism: the essential role of the nonessential amino acid, glutamine. *EMBO J* **2017**;36(10):1302-1315.

56.   Hui S, Ghergurovich JM, Morscher RJ, Jang C, Teng X, Lu W, et al. Glucose feeds the TCA cycle via circulating lactate. *Nature* **2017**;551(7678):115-118.

57.   Kamphorst JJ, Chung MK, Fan J, Rabinowitz JD. Quantitative analysis of acetyl-CoA production in hypoxic cancer cells reveals substantial contribution from acetate. *Cancer Metab* **2014**;2:23.

58.   Bjornson E, Mukhopadhyay B, Asplund A, Pristovsek N, Cinar R, Romeo S, et al. Stratification of Hepatocellular Carcinoma Patients Based on Acetate Utilization. *Cell Rep* **2015**;13(9):2014-2026.

59.   Bidkhori G, Benfeitas R, Klevstig M, Zhang C, Nielsen J, Uhlen M, et al. Metabolic network-based stratification of hepatocellular carcinoma reveals three distinct tumor subtypes. *Proc Natl Acad Sci U S A* **2018**;115(50):E11874-E11883.

60.   Gilkes DM, Semenza GL, Wirtz D. Hypoxia and the extracellular matrix: drivers of tumour metastasis. *Nat Rev Cancer* **2014**;14(6):430-439.

61.   Choudhry H, Harris AL. Advances in Hypoxia-Inducible Factor Biology. *Cell Metab* **2018**;27(2):281-298.

62.   Jiang Y, Hu T, Wang T, Shi X, Kitano A, Eagle K, et al. AMP-activated protein kinase links acetyl-CoA homeostasis to BRD4 recruitment in acute myeloid leukemia. *Blood* **2019**;134(24):2183-2194.

63.   Ho CL, Yu SC, Yeung DW. 11C-acetate PET imaging in hepatocellular carcinoma and other liver masses. *J Nucl Med* **2003**;44(2):213-221.

64.   Wen H, Lee S, Zhu WG, Lee OJ, Yun SJ, Kim J, et al. Glucose-derived acetate and ACSS2 as key players in cisplatin resistance in bladder cancer. *Biochim Biophys Acta Mol Cell Biol Lipids* **2019**;1864(3):413-421.

65.   Brown ZJ, Heinrich B, Greten TF. Establishment of Orthotopic Liver Tumors by Surgical Intrahepatic Tumor Injection in Mice with Underlying Non-Alcoholic Fatty Liver Disease. *Methods Protoc* **2018**;1(2):21.

66.   Mizuno H, Kitada K, Nakai K, Sarai A. PrognoScan: a new database for meta-analysis of the prognostic value of genes. *BMC Med Genomics* **2009**;2:18.

67.   Liberzon A, Birger C, Thorvaldsdóttir H, Ghandi M, Mesirov JP, Tamayo P. The Molecular Signatures Database (MSigDB) hallmark gene set collection. *Cell Syst* **2015**;1(6):417-425.

68.   Winter SC, Buffa FM, Silva P, Miller C, Valentine HR, Turley H, et al. Relation of a hypoxia metagene derived from head and neck cancer to prognosis of multiple cancers. *Cancer Res* **2007**;67(7):3441-3449.

69.   Villanueva A, Portela A, Sayols S, Battiston C, Hoshida Y, Méndez-González J, et al. DNA methylation-based prognosis and epidrivers in hepatocellular carcinoma. *Hepatology* **2015**;61(6):1945-1956.

70.   Cancer Genome Atlas Research Network. Comprehensive and Integrative Genomic Characterization of Hepatocellular Carcinoma. *Cell* **2017**;169(7):1327-1341 e1323.

71.   Bae JM, Kim JH, Oh HJ, Park HE, Lee TH, Cho NY, et al. Downregulation of acetyl-CoA synthetase 2 is a metabolic hallmark of tumor progression and aggressiveness in colorectal carcinoma. *Mod Pathol* **2017**;30(2):267-277.

72.   Uhlén M, Fagerberg L, Hallström BM, Lindskog C, Oksvold P, Mardinoglu

A, et al. Proteomics. Tissue-based map of the human proteome. *Science* **2015**;347(6220):1260419.

73.   Kampf C, Mardinoglu A, Fagerberg L, Hallstrom BM, Edlund K, Lundberg E, et al. The human liver-specific proteome defined by transcriptomics and antibody-based profiling. *FASEB J* **2014**;28(7):2901-2914.

74.   Huang Z, Zhang M, Plec AA, Estill SJ, Cai L, Repa JJ, et al. ACSS2 promotes systemic fat storage and utilization through selective regulation of genes involved in lipid metabolism. *Proc Natl Acad Sci U S A* **2018**;115(40):E9499-E9506.

75.   Bulusu V, Tumanov S, Michalopoulou E, van den Broek NJ, MacKay G, Nixon C, et al. Acetate Recapturing by Nuclear Acetyl-CoA Synthetase 2 Prevents Loss of Histone Acetylation during Oxygen and Serum Limitation. *Cell Rep* **2017**;18(3):647-658.

76.   Sun L, Kong Y, Cao M, Zhou H, Li H, Cui Y, et al. Decreased expression of acetyl-CoA synthase 2 promotes metastasis and predicts poor prognosis in hepatocellular carcinoma. *Cancer science* **2017**;108(7):1338-1346.

77.   Hoshida Y, Nijman SM, Kobayashi M, Chan JA, Brunet JP, Chiang DY, et al. Integrative transcriptome analysis reveals common molecular subclasses of human hepatocellular carcinoma. *Cancer Res* **2009**;69(18):7385-7392.

78.   Zucman-Rossi J, Villanueva A, Nault JC, Llovet JM. Genetic Landscape and Biomarkers of Hepatocellular Carcinoma. *Gastroenterology* **2015**;149(5):1226-1239.e1224.

79.   European Association for the Study of the Liver. EASL Clinical Practice Guidelines: Management of hepatocellular carcinoma. *J Hepatol* **2018**;69(1):182-236.

80.   Kenmochi K, Sugihara S, Kojiro M. Relationship of histologic grade of hepatocellular carcinoma (HCC) to tumor size, and demonstration of tumor cells of multiple different grades in single small HCC. *Liver* **1987**;7(1):18-26.

81.   Kargbo RB. Inhibition of ACSS2 for Treatment of Cancer and Neuropsychiatric Diseases. *ACS Med Chem Lett* **2019**;10(8):1100-1101.

82.   Sheng H, Tang W. Glycolysis Inhibitors for Anticancer Therapy: A Review of Recent Patents. *Recent Pat Anticancer Drug Discov* **2016**;11(3):297-308.

국문초록

암의 약제 내성 및 악성도에서

아세테이트 대사 연구

이 수 진

약학과 천연물과학전공

서울대학교 약학대학 대학원

아세테이트 대사는 생물에너지학, 거대 분자 합성, 및 후성 유전학과 관련하여 암의 아세테이트에 대한 대사적 의존성이 보고되면서 암 연구에서 새로운 흐름이 되고 있다. 그러나 아세테이트 대사가 항암제 내성 획득과 종양 등급 변화에 미치는 영향에 대한 연구는 아직 부족하다. 따라서 방광암의 시스플라틴 내성과 간암의 악성도 등급과 관련된 아세테이트의 대사적 특성과 이의 임상적 의의를 조사하였다. 첫째로 최근 방광암에서 지질 대사가 변화되어 있다는 것이 보고되어 시스플라틴 민감성 (T24S) 및 내성 (T24R) 방광암 세포를 사용하여 시스플라틴 저항성의 대사적 의미를 연구하였다. 실시간 라이브

대사체학을 이용하여 시스플라틴 저항성 방광암 세포 (T24R)에서 시스플라틴 민감성 방광암 세포 (T24S) 대비 글루코스를 더 많이 소모하며 글루코스 유래 아세테이트와 지방산을 더 많이 생산하는 것을 확인하였다. T24R 세포에서 일반적인 대사 조절제의 활성화와 더불어 아세테이트 사용 (ACSS2) 및 지방산 합성 (ACC) 효소와 지방 합성을 위한 전구체 (아세틸-CoA)가 상승했다. ^{13}C 동위 원소를 사용한 대사 분석에서도 일관되게 T24R 세포가 T24S 세포와 다르게 지방산 합성 증가를 위한 외인성 탄소 공급원으로 아세테이트보다 글루코스를 선호한다는 것이 나타났다. 또한 T24R 세포에서 글루코스 유래 내인성 아세테이트를 통해 아세틸-CoA 를 공급하는 핵심 효소는 잘 확립된 ACLY 가 아닌 ACSS2 였다. ACSS2 의 상관성은 ACSS2 억제제에 의한 시스플라틴 저항성 상실에 의해 추가로 확인되었으며, 시스플라틴 저항성을 가진 환자 조직에서 ACSS2 의 더 높은 발현에 의해 확인되었다. 둘째로 간암에 대한 아세테이트 흡수, 대사적 특성, 및 악성 종양 간의 관계를 종합적으로 연구했다. 세포주 중 HepG2 는 글루코스가 충분한 환경에서도 아세테이트를 사용했지만 Hep3B 에서는 그렇지 않았고 이는 ACSS2 의 발현과 연관이 있었다. 대사체 동위 원소 추적에서 ACSS2 가 높은 HepG2 는 Hep3B 보다 더 높은 아세테이트 유입과 향상된 지질 단백 대사를 나타냈다. 이러한 대사 특성은 ACSS2, 마스터 단백 동화 유전자 (mTOR), 그리고 지질 이화 유전자 (CPT1)에 대한 유전자 발현 억제 및 억제제 연구를 통해 확인되었다. in-vivo ^{13}C

102

동위 원소 추적에서 HepG2 의 동소 (orthotopic) 마우스 간암은 단백 동화가 더 잘 일어나고 악성도가 낮음이 확인되었다. 일관되게 사람의 정상 간 조직은 암 조직보다 더 높은 ACSS2 수준을 나타냈다. ACSS2 발현이 낮은 환자, 특히 13 번째 백분위수 이하 (13VLA 그룹)의 환자는 두 개의 독립적인 대규모 코호트에서 현저하게 예후가 나빴다 (총 n = 486). 또한 13VLA 환자는 더 높은 ACSS2 프로모터 메틸화, 감소된 지질 합성 경로, 그리고 증가된 해당 과정 및 강화된 저산소증을 나타냈다. 환자의 PET-CT 영상은 악성도가 낮은 간암이 ^{11}C-아세테이트의 흡수가 더 많고 ^{18}F-FDG 의 흡수가 적다는 것을 보여주었으며 이는 악성도가 높은 간암에서 역전되었다. 전반적으로 아세테이트 흡수는 영양소 고갈과 무관한 것으로 보이며 지질 단백 대사 증가와 간암의 더 나은 예후에 기여한다. 본 연구는 방광암과 간암 환자에 대한 치료 옵션을 개선하고 맞춤형 치료를 위한 환자의 취약성에 기반한 표적 개발에 도움을 줄 수 있다.

주요어: 아세테이트, ACSS2, 대사체학, 암 대사, 핵자기 공명 분광법, 질량 분석법, 생물정보학, 악성도, 방광암, 간암

학 번: 2014-31253

This appendix includes reprints of four published papers. I have participated as the first author for two of the papers, and as a co-first author for the other two. These works were done during my doctoral course in Seoul National University under my supervisor, Professor Sunghyouk Park.

Appendix

Specific Detection of Cellular Glutamine Hydrolysis in Live Cells Using HNCO Triple Resonance NMR

Sujin Lee,[†,‖] He Wen,[†,‡,‖] Jin Wook Cha,[†,§] and Sunghyouk Park*[†]

[†]Natural Product Research Institute, College of Pharmacy, Seoul National University, Sillim-dong, Gwanak-gu, Seoul, 151−742, Korea

[‡]Department of Biochemistry and Molecular Biology, School of Medicine, Shenzhen University, Shenzhen, 518060, China

[§]Natural Constituents Research Center, Korea Institute of Science and Technology (KIST), Gangneung, 25451, Korea

S Supporting Information

ABSTRACT: Glutamine plays key roles as a biosynthetic precursor or an energy source in cancers, and interest in its metabolism is rapidly growing. However, the proper evaluation of glutamine hydrolysis, the very first reaction in the entire glutaminolysis, has been difficult. Here, we report a triple resonance NMR-based assay for specific detection of glutaminase activity carrying out this reaction using stable-isotope labeled glutamine. Compared to conventional methods involving coupled enzyme assays, the proposed approach is direct because it detects the presence of the H−N−CO amide spin system. In addition, the method is unique in enabling the measurement of glutamine hydrolysis reaction in real-

time in live cells. The approach was applied to investigating the effects of a glutaminase inhibitor and the inhibitory effects of glucose on glutamine metabolism in live cells. It can be easily applied to studying other signals that affect cellular glutamine metabolism.
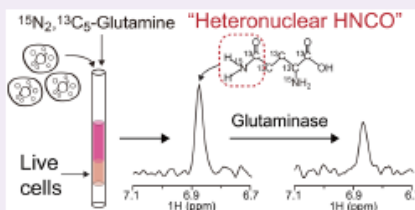
Reprogramming of metabolism in cancers to support biosynthetic activity and energy generation has been reported in a variety of cancers.[1,2] This altered metabolic activity usually involves avid uptake and consumption of glucose, but many cancer cells also depend on glutamine, a phenomenon called glutamine addiction.[3,4] Glutamine is metabolized through glutaminolysis that converts glutamine to lactate via multiple reaction steps.[5,6] Glutamine is first converted to glutamate and then α-ketoglutarate, which enters the TCA cycle for the subsequent metabolism to malate. Malate is then converted to pyruvate by malic enzyme, and the resulting pyruvate is reduced to lactate by lactate dehydrogenase. The metabolic steps after the entry to the TCA cycle also occur during the oxidation of glucose, and therefore, the pre-TCA steps of glutaminolysis, the conversion to glutamate and then to α-ketoglutarate, have unique significance in the glutamine metabolism. Among the two reactions, the hydrolysis of glutamine to glutamate and ammonia is the first reaction of the entire glutaminolysis and is practically irreversible,[7] thereby affecting the entire glutamine usage. This glutamine hydrolysis is mediated by glutaminases encoded by *GLS1* and *GLS2*, which encode two tissue-specific isozymes, kidney type and liver type glutaminases, respectively.[8,9] Consistent with the importance of glutamine metabolism in cancers, glutaminase has been implicated in cancers. Proto-oncoprotein MYC increases the expression of glutaminase by inhibiting the transcription of glutaminase repressor microRNA-23a/b.[10] Glutaminase has been also shown to be elevated in a number

of cancers, and its inhibition suppressed oncogenic transformation of fibroblasts.[11,12] In accordance with these, CB-839, a first-in-class anticancer agent targeting glutaminase, is under clinical trials for hematologic and solid tumors (clinicaltrials.gov identifier: NCT02071862, NCT02071888[13]). Still, most studies on glutamine metabolism have measured glutaminase expression/amount which may not necessarily represent the actual activity of the enzyme. Therefore, proper evaluation of glutaminase activity both *in vitro* and in cells can contribute to an adequate evaluation of glutamine metabolism in cancers.

A commonly used glutaminase activity assay is an indirect coupled-enzymatic assay measuring NAD(P)H with colorimetry.[14,15] In the assay, glutaminase converts glutamine to glutamate, which is further converted to α-ketoglutarate with concomitant generation of NAD(P)H by glutamate dehydrogenase. Naturally, the results can be affected by coexisting glutamate dehydrogenase or glutamate transaminase activities in samples. In addition, interference from light-absorbing experimental reagents and NAD(P)H modulation by other cellular dehydrogenases should be considered in the indirect colorimetric NAD(P)H measurements. There are other assay methods for glutaminase, such as those measuring NH₃ produced by glutaminase using Nessler's reagent[16,17] and those involving ^{14}C glutamine and column separation of [14]C

A

glutamate.[18,19] The former suffers from the specificity issue as other nitrogen-containing metabolites such as glutamate (*via* glutamate dehydrogenase) and asparagine (*via* asparaginase) can produce NH_3, and the latter has issues with the use of radioactivity. Another equally important consideration with the above *in vitro* glutaminase assay is the requirement of high phosphate concentration ($\sim$40 mM) for the enzyme activation. As serum phosphate concentration is only about $\sim$1 mM,[20] this characteristic led to a suggestion of possibly distinct enzymatic mechanisms *in vitro* vs *in vivo*. In addition, glutaminase activities have been shown to be markedly affected by solubilization techniques,[21] and the inhibition characteristics were different between purified glutaminases and those in isolated mitochondria.[22] Therefore, glutaminase activity measured *in vitro*, i.e., with cell lysate, may not represent the true activity in actual intact cells. As all of the above-mentioned conventional assay methods require cell extractions, a reliable method for glutaminase activity measurement in live cells has also been desired. Here, we describe a triple resonance NMR-based assay for the detection of glutaminase activity applicable to both cell lysates and intact cells. We also demonstrate its utility in assessing the effects of glucose on cellular glutaminase activities in live cells.

■ RESULTS AND DISCUSSION

Glutamine Affects Cell Growth Rate. To assess the dependence of the growth rate of L1210 cells on glutamine availability, L1210 cells were grown under various glutamine concentrations. We supplemented the glucose and glutamine-free DMEM media with 4 mM, 0.5 mM, or 0 mM glutamine and 10 mM glucose to measure the growth rate for 72 h. The cell growth rates gradually decreased with lower glutamine concentrations (Figure 1). After 72 h, the number of cells for
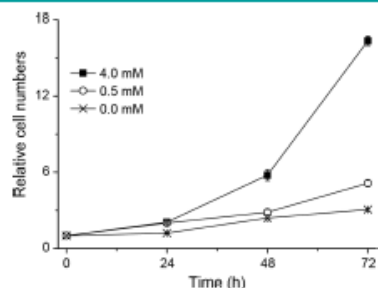

Figure 1. Glutamine dependence of L1210 cell growth. L1210 cell growth under various glutamine concentrations (0, 0.5, or 4 mM) was measured with the cell cytometry at indicated time points after seeding with 10 mM glucose. The values represent the cell numbers normalized to that at the 0 h point. The error bars represent the standard deviation. Cross, 0 mM group; open circle, 0.5 mM group; filled box, 4 mM group.

the 0.5 mM and 0 mM glutamine groups were 31% and 19% that of the 4 mM glutamine group, respectively. Therefore, glutamine seems essential for the fast growth of L1210 leukemia cells. As the first step of glutamine metabolism in cells is its hydrolysis into glutamate and ammonia, a practically irreversible reaction mediated by glutaminase,[7] the correct

estimation of this hydrolysis activity is important for overall assessment of glutamine metabolism.

A New Assay Using HNCO Triple Resonance NMR. We developed a novel assay that can directly detect the glutamine hydrolysis without the need of a coupled enzyme reaction or purification step, so that it may be used in complex mixtures or in live cells. The assay exploited a triple resonance HNCO NMR experiment and nonradioactive [13]C- and ^{15}N-isotope labeled glutamine (Figure 2). As shown previously by us and
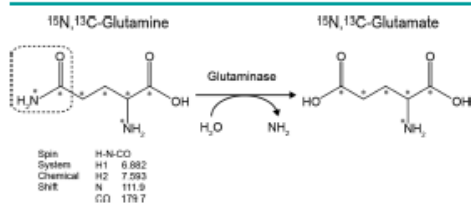

Figure 2. Glutaminase enzyme reaction and the spin system detected by HNCO experiment. [13]C_5-labeled carbons and [15]N_2-nitrogens are indicated with asterisks, and the H−N−CO spin system detected by HNCO is indicated with dotted box. The chemical shifts of the spin system are also presented.

others, triple resonance NMR experiments, if customized appropriately, can be used for specific enzymatic assay methods *in vitro*.[23−25] The three-dimensional HNCO experiment has actually been used widely in protein NMR community to establish the sequential connectivity through the backbone amide spin system (nitrogen and carbonyl carbons). We tailored the one-dimensional version of HNCO to detect the side chain amide spin system of glutamine by setting the offset frequencies of the carbonyl and nitrogen to those of the glutamine side chain. Given the covalent bond between N and CO atoms in the amide group of glutamine, the HNCO experiment is best suited to detect the glutamine hydrolysis.

Glutamine Detection in a Complex Mixture. The feasibility of the assay method was first tested using L1210 cell lysate, a complex mixture without any purification. The labeled glutamine was added to the lysate, and a conventional one-dimensional NMR spectrum was obtained. The spectrum featured many overlapped signals from the complex mixture, making it difficult to quantify the glutamine level (Figure 3a). The identification of glutamine peaks in the amide region was not possible probably due to the complex splitting of the amide signals and the intensity decrease by $^1J_{H-N}$, $^2J_{H-C=O}$, and $^3J_{H-CH_2}$. The same mixture was subjected to the HNCO experiment, and the spectrum showed clean glutamine amide proton signals without any background signals (Figure 3b). This high selectivity is due to the extremely low (3×10^{-5}) natural abundance of the H−[15]N−[13]CO spin system, and the detected signal can be safely considered coming only from the added isotope-labeled glutamine. It is also worth mentioning that a simple one-dimensional spectrum may not be used for specific detection of glutamine hydrolysis, since glutamine and asparagine amide signals completely overlap in a cell lysate spectrum (Supporting Information Figure S1).

Real-Time Monitoring of Glutamine Hydrolysis in Live Cells. With the success in specific detection of glutamine in a complex mixture, we tested the HNCO NMR method for monitoring glutamine hydrolysis in real-time in live cells. We
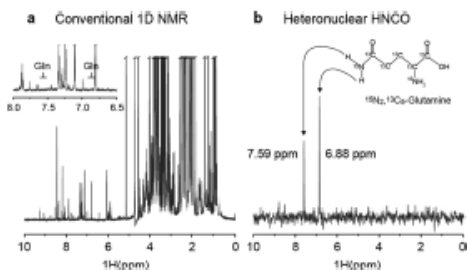
B

Figure 3. Monitoring glutaminase reaction with conventional or HNCO NMR experiment. Conventional one-dimensional NMR spectrum (a) and heteronuclear HNCO spectrum (b) of the glutaminase reaction sample with $^{13}C_5$, $^{15}N_2$-glutamine in L1210 cell lysate. The inset in a is the expansion of the 6.5–8.0 ppm region. The expected positions of the glutamine peaks considering the scalar couplings to ^{15}N and ^{13}C are indicated.

added the labeled glutamine in the cell suspension and placed the mixture into a shigemi NMR tube. The NMR experiment was carried out as described in our recent paper for adherent cells with live NMR metabolomics.[26] Here, we modified the sample preparation procedures for the suspension culture cells and showed that a specific metabolic reaction can also be followed in real-time in live L1210 cells (Figure 4). With the HNCO experiment, the glutamine peak was observed, which allowed the real-time monitoring of intensity decreases of the peak due to the hydrolysis by glutaminase activities. Our approach itself does not discriminate the glutamine in- or outside the cells, and it measures the total glutamine.
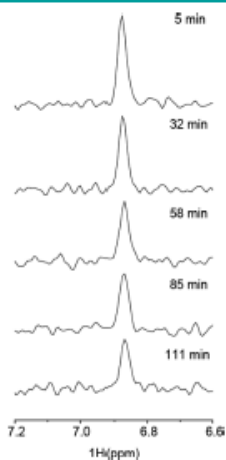

Figure 4. Time-dependent monitoring of glutaminase reaction in live cells. Changes in glutamine peak intensities detected by HNCO with live L1210 cells. L1210 cells were suspended in a media containing $^{13}C_5$,$^{15}N_2$-glutamine (4 mM) and nonlabeled glucose (10 mM), and the HNCO spectra of the cell samples directly put into an NMR tube were measured at the indicated time points. Out of the two glutamine peaks, one at 6.882 ppm is shown.

Nevertheless, as glutaminase is present inside the cells, the observed glutamine peak changes represent the glutamine hydrolysis inside the cells.

Application of the HNCO Assay for Inhibitors and Glucose Effects. Since we set up the new assay, we applied it to practical cases of chemical and biological interest. First, the assay can be used to test an inhibitor for glutaminase that mediates the hydrolysis. Glutaminase inhibitors might be used as anticancer drugs of a novel mechanism, as exemplified by CB-839, which is under clinical trial for acute lymphocytic leukemia and solid tumors (Clinicaltrials.gov identifier: NCT02071927 and NCT02071862). When we added a glutaminase inhibitor 6-diazo-5-oxo-L-norleucine (DON, 4 mM), the HNCO signal intensity remained unchanged over time, as opposed to the steady decrease in the control group (Figure 5). This confirms that our assay is specific for
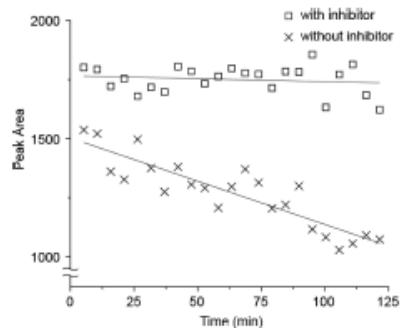

Figure 5. Effects of a glutaminase inhibitor treated to live cells on the HNCO peak intensities. HNCO spectra were acquired for live L1210 cells in an NMR tube as in Figure 4 in the absence (cross) and presence (box) of 6-diazo-5-oxo-L-norleucine (4 mM).

glutaminase-mediated glutamine hydrolysis in cells. It also shows that this live cell assay can be used to test whether an *in vitro* inhibitor actually penetrates the cell membrane and inhibits intracellular glutaminase activities. This is a significant advantage over other *in vitro* enzyme assays, since many compounds with *in vitro* activities fail to show activities in cellular experiments due to the cell penetration issues. This inhibitor experiment also shows that the glutaminase activity is indeed a major factor in glutamine hydrolysis reaction in live cells. In theory, carbamoyl phosphate synthase (CPS) might also catalyze the glutamine hydrolysis. However, based on the near-invariable level of glutamine peak in the inhibitor-treated group, the CPS activity should be negligible compared to that of glutaminase under this condition.

The second application is about the effects of glucose availability on glutamine metabolism by glutaminase. Although increased glucose metabolism is one of the common features of cancers,[27,28] glutamine is also important, and glutamine addiction is found in various cancers.[4,29] In this respect, the effects of glucose on glutamine metabolism in live cells may be important in cancer metabolism, and they can be readily assessed using our HNCO NMR. Therefore, we added varying concentrations of glucose to L1210 cell suspension and measured the remaining glutamine level after incubation (15 min). The glutamine peaks were larger with a higher

C

concentration of added glucose (Figure 6), suggesting that glucose prevents the glutamine hydrolysis. Similar results were
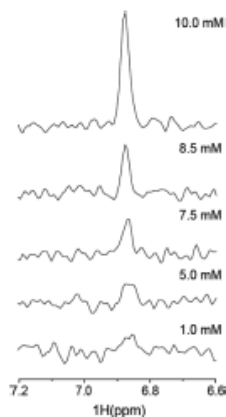

Figure 6. Effects of glucose concentrations on glutamine metabolism. Glutamine peaks detected by HNCO NMR from live L1210 cells in the presence of the indicated amounts of glucose (incubation time 15 min). Out of the two glutamine peaks, one at 6.882 ppm is shown. HNCO spectra were acquired for L1210 cells in an NMR tube as in Figure 4.

obtained with different relaxation delays (Supporting Information Figure S2), showing the technical consistency of the experiment. Previous studies have suggested that glucose levels are related with glutamine metabolism.[10,30] A low glucose condition was found to increase the expression of c-myc,[31] whose product, MYC, inhibits the expression of miR-23a/b that suppresses glutaminase transcription. Our results support these effects of glucose at the metabolite level in live cells rather than glutaminase expression. Whether or not glucose also affects the glutamine transporter may be an interesting future question.

In theory, glutamine hydrolysis may also be monitored with a simpler 2D heteronuclear single quantum coherence (2D HSQC) experiment. The biggest advantage of the proposed HNCO approach is the specificity for the desired glutaminase-mediated reaction. A likely confounding reaction to the glutaminase catalysis is glutamine synthetase-mediated back-synthesis of glutamine. In this reaction, the ^{15}N labeled ammonia released by glutaminase reacts with endogenous (^{12}C) glutamate to give ^{15}N-labeled glutamine. This can happen as intracellular glutamate concentration can be as high as 10 mM.[32] Since the regenerated ^{15}N-labeled glutamine will be also detected by 2D HSQC, the monitoring of true glutaminase-mediated glutamine consumption is not possible with the experiments. In some cases, where glutamine synthetase activity is very high, the apparent glutaminase activity detected by 2D HSQC can be very low, even though the glutaminase activity is actually high. In comparison, the triple resonance HNCO experiment will not detect the back-synthesized ^{15}N-labeled glutamine with ^{12}C. It detects only the ^{15}N and ^{13}C-labeled glutamine that we added and therefore gives a much better estimation of the consumed glutamine by glutaminase.

One interesting and consistent observation is that the glutamine peak was broadened to a near-noise level in the

media-only sample before the cell addition. After the addition of the cells and the required dead time for the NMR experiment (10 min), the glutamine peak showed up, and its intensity gradually decreased over the experimental time (60 min; Supporting Information Figure S3). The initial appearance of the peak at the first point was very abrupt compared to the decrease after the addition of the cells. This result suggests that the glutamine transport is much faster than the hydrolysis and that the transport is not rate-limiting in the glutamine consumption.

Overall, our real-time in-cell HNCO NMR assay is a convenient and specific method detecting glutaminase activity. Compared to other conventional methods, our approach detects direct glutamine hydrolysis reaction mediated by glutaminase. In addition, the detection of a stable-isotope labeled amide bond in H−N−CO system confers selectivity, enabling its straightforward application to a very challenging system such as live cells. As glutamine metabolism and the associated glutaminase activity are gaining interest in cancer research and treatments, our approach may prove useful for studying them and inhibitor effects in native cellular environments. The method can be straightforwardly extended to effects of other nutrients or protein status on glutamine metabolism.

■ METHODS

Chemicals and Reagents. The stable U−^{13}C$_5$,U−^{15}N$_2$ isotope labeled glutamine (CNLM-1275, U−^{13}C$_5$, 99%; U−^{15}N$_2$, 99%) was purchased from Cambridge Isotope Laboratories (Andover, MA, USA). D-(+)-glucose solution (G8644, D-(+)-Glucose 10%) and 6-diazo-5-oxo-L-norleucine (DON), a glutaminase inhibitor, were obtained from Sigma-Aldrich (St. Louis, MO, USA).

Cell Lines and Cultures. The mouse lymphocytic leukemia L1210 cells were obtained from American Type Culture Collection (ATCC) and grown in DMEM medium (HyClone, Logan, UT, USA) supplemented with 10% heat-inactivated fetal bovine serum (FBS, HyClone, Logan, UT, USA) and penicillin-streptomycin solution (HyClone, Logan, UT, USA). Cells were cultured at 37 °C and 5% CO$_2$ humidified incubator. For the growth measurements, L1210 cells (5×10^5) were seeded in six-well plates containing 4, 0.5, or 0 mM glutamine and 10 mM glucose in DMEM media without glucose and glutamine (Gibco, Grand Island, NY, USA). After 24, 48, and 72 h of incubation, the cells were counted using cell hemocytometer.

Sample Preparation for NMR Spectroscopy. The sample preparation was adapted from a previous report for live metabolomics[26] for use with the suspension cell culture. The counted L1210 cells (10^8) were resuspended with 500 μL of NMR media (DMEM media without glucose and glutamine (Gibco, Grand Island, NY, USA) supplemented with 10% dialyzed FBS (Welgene, Daegu, Korea), 4 mM ^{13}C$_5$,^{15}N$_2$-labeled glutamine, an indicated amount of unlabeled glucose, and 10% D$_2$O). An NMR shigemi tube containing L1210 cell suspension was centrifuged lightly with a hand centrifuge to sediment the live cells. For the glutaminase inhibitor-treated samples, 6-diazo-5-oxo-L-norleucine (4 mM) was also added to the media. For the spectra of cell lysates, the harvested cell pellets were resuspended with 400 μL of a mixture composed of methanol, acetonitrile, and distilled water (5:3:2). The samples were centrifuged at 15 000g for 20 min at 4 °C. The supernatant was collected and then dried with a vacuum centrifugator (Vision, Seoul, Korea). The pellets were redissolved with 500 μL of buffer composed of 2 mM Na$_2$HPO$_4$ and 5 mM NaH$_2$PO$_4$ in D$_2$O with 0.025% TSP as an internal standard.

NMR Measurement. One-dimensional HNCO NMR spectra were measured on an 800-MHz Bruker Avance spectrometer with a cryogenic triple resonance probe using a 3D HNCO pulse sequence (HNCOGP3D with Waltz65 composite decoupling). A spectrum with a media-only sample before the addition of the cells was obtained, and then, the time course measurement with cells was performed at 37 °C for 23 time points, each taking 5 min. One second of relaxation delay

D

was used unless specified otherwise. The deadtime between the media-only spectrum and the time course experiment was 10 min.

■ ASSOCIATED CONTENT

ⓢ Supporting Information

■ AUTHOR INFORMATION

Corresponding Author

*Phone: +82-2-880-7831. Fax: +82-2-880-7831. E-mail: psh@snu.ac.kr.

Author Contributions

║These authors equally contributed to this work.

Notes

The authors declare no competing financial interest.

■ ACKNOWLEDGMENTS

■ REFERENCES

(1) Schulze, A., and Harris, A. L. (2012) How cancer metabolism is tuned for proliferation and vulnerable to disruption. *Nature* 491, 364–373.

(2) Pavlova, N. N., and Thompson, C. B. (2016) The Emerging Hallmarks of Cancer Metabolism. *Cell Metab.* 23, 27–47.

(3) Wise, D. R., and Thompson, C. B. (2010) Glutamine addiction: a new therapeutic target in cancer. *Trends Biochem. Sci.* 35, 427–433.

(4) Hensley, C. T., Wasti, A. T., and DeBerardinis, R. J. (2013) Glutamine and cancer: cell biology, physiology, and clinical opportunities. *J. Clin. Invest.* 123, 3678–3684.

(5) Jin, L., Alesi, G. N., and Kang, S. (2016) Glutaminolysis as a target for cancer therapy. *Oncogene* 35, 3619.

(6) Jacque, N., Ronchetti, A. M., Larrue, C., Meunier, G., Birsen, R., Willems, L., Saland, E., Decroocq, J., Maciel, T. T., Lambert, M., Poulain, L., Hospital, M. A., Sujobert, P., Joseph, L., Chapuis, N., Lacombe, C., Moura, I. C., Demo, S., Sarry, J. E., Recher, C., Mayeux, P., Tamburini, J., and Bouscary, D. (2015) Targeting glutaminolysis has antileukemic activity in acute myeloid leukemia and synergizes with BCL-2 inhibition. *Blood* 126, 1346–1356.

(7) Benzinger, T. H., and Hems, R. (1956) Reversibility and Equilibrium of the Glutaminase Reaction Observed Calorimetrically to Find the Free Energy of Adenosine Triphosphate Hydrolysis. *Proc. Natl. Acad. Sci. U. S. A.* 42, 896–900.

(8) Botman, D., Tigchelaar, W., and Van Noorden, C. J. (2014) Determination of phosphate-activated glutaminase activity and its kinetics in mouse tissues using metabolic mapping (quantitative enzyme histochemistry). *J. Histochem. Cytochem.* 62, 813–826.

(9) Mates, J. M., Segura, J. A., Martin-Rufian, M., Campos-Sandoval, J. A., Alonso, F. J., and Marquez, J. (2013) Glutaminase isoenzymes as key regulators in metabolic and oxidative stress against cancer. *Curr. Mol. Med.* 13, 514–534.

(10) Gao, P., Tchernyshyov, I., Chang, T. C., Lee, Y. S., Kita, K., Ochi, T., Zeller, K. I., De Marzo, A. M., Van Eyk, J. E., Mendell, J. T.,

and Dang, C. V. (2009) c-Myc suppression of miR-23a/b enhances mitochondrial glutaminase expression and glutamine metabolism. *Nature* 458, 762–765.

(11) Katt, W. P., and Cerione, R. A. (2014) Glutaminase regulation in cancer cells: a druggable chain of events. *Drug Discovery Today* 19, 450–457.

(12) Wang, J. B., Erickson, J. W., Fuji, R., Ramachandran, S., Gao, P., Dinavahi, R., Wilson, K. F., Ambrosio, A. L., Dias, S. M., Dang, C. V., and Cerione, R. A. (2010) Targeting mitochondrial glutaminase activity inhibits oncogenic transformation. *Cancer Cell* 18, 207–219.

(13) Gross, M. I., Demo, S. D., Dennison, J. B., Chen, L., Chernov-Rogan, T., Goyal, B., Janes, J. R., Laidig, G. J., Lewis, E. R., Li, J., Mackinnon, A. L., Parlati, F., Rodriguez, M. L., Shwonek, P. J., Sjogren, E. B., Stanton, T. F., Wang, T., Yang, J., Zhao, F., and Bennett, M. K. (2014) Antitumor activity of the glutaminase inhibitor CB-839 in triple-negative breast cancer. *Mol. Cancer Ther.* 13, 890–901.

(14) Pye, I. F., Stonier, C., and McGale, H. F. (1978) Double-enzymatic assay for determination of glutamine and glutamic acid in cerebrospinal fluid and plasma. *Anal. Chem.* 50, 951–953.

(15) Gella, F. J., and Pascual, M. A. (1982) Assay of glutaminase activity by colorimetric determination of glutamate. *Anal. Biochem.* 127, 322–325.

(16) Imada, A., Igarasi, S., Nakahama, K., and Isono, M. (1973) Asparaginase and glutaminase activities of micro-organisms. *J. Gen. Microbiol.* 76, 85–99.

(17) Madaras, M. B., Spokane, R. B., Johnson, J. M., and Woodward, J. R. (1997) Glutamine biosensors for biotechnology applications, with suppression of the endogenous glutamate signal. *Anal. Chem.* 69, 3674–3678.

(18) Prusiner, S., and Milner, L. (1970) A rapid radioactive assay for glutamine synthetase, glutaminase, asparagine synthetase, and asparaginase. *Anal. Biochem.* 37, 429–438.

(19) Engler, J. A., Gottesman, J. M., Harkins, J. C., Urazaev, A. K., Lieberman, E. M., and Grossfeld, R. M. (2002) Properties of glutaminase of crayfish CNS: implications for axon-glia signaling. *Neuroscience* 114, 699–705.

(20) Kottmann, R. M., Kulkarni, A. A., Smolnycki, K. A., Lyda, E., Dahanayake, T., Salibi, R., Honnons, S., Jones, C., Isern, N. G., Hu, J. Z., Nathan, S. D., Grant, G., Phipps, R. P., and Sime, P. J. (2012) Lactic acid is elevated in idiopathic pulmonary fibrosis and induces myofibroblast differentiation via pH-dependent activation of transforming growth factor-beta. *Am. J. Respir. Crit. Care Med.* 186, 740–751.

(21) McGivan, J. D., and Bradford, N. M. (1983) Influence of phospholipids on the activity of phosphate-dependent glutaminase in extracts of rat liver mitochondria. *Biochem. J.* 214, 649–652.

(22) Shapiro, R. A., Haser, W. G., and Curthoys, N. P. (1985) The orientation of phosphate-dependent glutaminase on the inner membrane of rat renal mitochondria. *Arch. Biochem. Biophys.* 243, 1–7.

(23) Wen, H., Yun, T., Xu, W. J., Choi, S. H., Kim, H., Park, C. K., Lee, S. H., Park, S. W., Lee, S. K., and Park, S. (2013) A highly facile and specific assay for cancer-causing isocitrate dehydrogenase mutant using 13C4-labeled α-ketoglutarate and heteronuclear NMR. *Anal. Chem.* 85, 11987–11992.

(24) Yamada, H., Mizusawa, K., Igarashi, R., Tochio, H., Shirakawa, M., Tabata, Y., Kimura, Y., Kondo, T., Aoyama, Y., and Sando, S. (2012) Substrate/Product-targeted NMR monitoring of pyrimidine catabolism and its inhibition by a clinical drug. *ACS Chem. Biol.* 7, 535–542.

(25) Ueki, R., Yamaguchi, K., Nonaka, H., and Sando, S. (2012) 1H NMR probe for in situ monitoring of dopamine metabolism and its application to inhibitor screening. *J. Am. Chem. Soc.* 134, 12398–12401.

(26) Wen, H., An, Y. J., Xu, W. J., Kang, K. W., and Park, S. (2015) Real-time monitoring of cancer cell metabolism and effects of an anticancer agent using 2D in-cell NMR spectroscopy. *Angew. Chem., Int. Ed.* 54, 5374–5377.

(27) Elf, S. E., and Chen, J. (2014) Targeting glucose metabolism in patients with cancer. *Cancer 120*, 774−780.

(28) Koppenol, W. H., Bounds, P. L., and Dang, C. V. (2011) Otto Warburg's contributions to current concepts of cancer metabolism. *Nat. Rev. Cancer 11*, 325−337.

(29) DeBerardinis, R. J., Mancuso, A., Daikhin, E., Nissim, I., Yudkoff, M., Wehrli, S., and Thompson, C. B. (2007) Beyond aerobic glycolysis: transformed cells can engage in glutamine metabolism that exceeds the requirement for protein and nucleotide synthesis. *Proc. Natl. Acad. Sci. U. S. A. 104*, 19345−19350.

(30) Liu, L., Ulbrich, J., Muller, J., Wustefeld, T., Aeberhard, L., Kress, T. R., Muthalagu, N., Rycak, L., Rudalska, R., Moll, R., Kempa, S., Zender, L., Eilers, M., and Murphy, D. J. (2012) Deregulated MYC expression induces dependence upon AMPK-related kinase 5. *Nature 483*, 608−612.

(31) Briata, P., Laurino, C., and Gherzi, R. (1989) c-myc gene expression in human cells is controlled by glucose. *Biochem. Biophys. Res. Commun. 165*, 1123−1129.

(32) Stanley, C. A. (2009) Regulation of glutamate metabolism and insulin secretion by glutamate dehydrogenase in hypoglycemic children. *Am. J. Clin. Nutr. 90*, 862s−866s.

F

Carbon Isotopomer Analysis with Non-Unifom Sampling HSQC NMR for Cell Extract and Live Cell Metabolomics Studies

Sujin Lee,[†] He Wen,[†,‡] Yong Jin An,[†] Jin Wook Cha,[†,§] Yoon-Joo Ko,[∥] Sven G. Hyberts,[⊥] and Sunghyouk Park*[,†]

[†]Natural Product Research Institute, College of Pharmacy, Seoul National University, Sillim-dong, Gwanak-gu, Seoul 151-742, Korea

[‡]Department of Biochemistry and Molecular Biology, School of Medicine, Shenzhen University, Shenzhen 518060, China

[§]Natural Constituents Research Center, Korea Institute of Science and Technology (KIST), Gangneung 25451, Korea

[∥]National Center for Inter-University Research Facilities (NCIRF), Seoul National University, Sillim-dong, Gwanak-gu, Seoul 151-742, Korea

[⊥]Department of Biological Chemistry and Molecular Pharmacology, Harvard Medical School, Boston, Massachusetts 02115, United States

S Supporting Information

ABSTRACT: Isotopomer analysis using either ^{13}C NMR or LC/GC−MS has been an invaluable tool for studying metabolic activities in a variety of systems. Traditional challenges are, however, that ^{13}C-detected NMR is insensitive despite its high resolution, and that MS-based techniques cannot easily differentiate positional isotopomers. In addition, current ^{13}C NMR or LC/GC−MS has limitations in detecting metabolites in living cells. Here, we describe a non-uniform sampling-based 2D heteronuclear single quantum coherence (NUS HSQC) approach to measure metabolic isotopomers in both cell lysates and living cells. The method provides a high resolution that can resolve multiplet structures in the ^{13}C dimension while retaining the sensitivity of the [1]H-indirect detection. The approach was tested in L1210 mouse leukemia cells labeled with ^{13}C acetate by measuring NUS HSQC with 25% sampling density. The results gave a variety of metabolic information such as (1) higher usage of acetate in acetylation pathway than aspartate synthesis, (2) TCA cycle efficiency changes upon the inhibition of mitochondrial oxidative phosphorylation by pharmacological agents, and (3) position-dependent isotopomer patterns in fatty acids in living cells. In addition, we were able to detect fatty acids along with other hydrophilic molecules in one sample of live cells without extraction. Overall, the high sensitivity and resolution along with the application to live cells should make the NUS HSQC approach attractive in studying carbon flux information in metabolic studies.
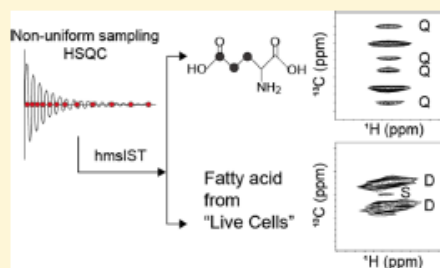
N MR has been an invaluable tool for metabolomic studies with its superb reproducibility, quantitativeness, and information-richness.[1−3] So far, the most popular approach of NMR metabolomics involves the one-dimensional (1D) ^{1}H NMR experiment. As it is quick and easy to perform, it has been particularly popular for clinical applications with a large number of heterogeneous samples.[4−7] In comparison, two-dimensional isotope-edited NMR has not been used as much due to its longer time requirement and low natural abundance of isotopes, although it can give more confidence in molecular identification.[8,9] Isotope-edited two-dimensional NMR is more suited for studies that are compatible with isotope incorporation or homogeneous samples, such as cell culture systems. Recently, the use of stable isotopes highlighted the usefulness of isotopomer-based metabolomic flux analysis in elucidating complex metabolic alterations in cancer cells.[10−12] Isotope-edited two-dimensional NMR also has unique advantages in

those studies,[13] but it has been exploited only in limited cases.[14,15] The main limiting factor of the infrequent use is the poor resolution in the indirectly detected ^{13}C dimension preventing the isotopomer analysis. ^{13}C-direct-detected one-dimensional NMR has been also used for the isotopomer analysis, but it suffered from disappointingly low sensitivity and signal overlaps.[3,16−18]

Non-uniform sampling (NUS) NMR has been developed in the protein NMR community to both shorten the experimental time for multidimensional data and increase the resolution of the indirect dimension. Initially, the processing itself took much effort and required high computing power. However, recently proposed methods provide robust processing efficiency making

A

the processing possible even with a laptop computer.[19,20] The approach enabled us to cut the routine protein NMR acquisition time from several days to about a day. Naturally, NUS methodology has also been adapted to the NMR metabolomics field, and it was shown that high quality two-dimensional data can be obtained for steady state metabolomics in a shorter time.[21−23] However, another important merit of NUS NMR, the high resolution in the indirect dimension, has not been much exploited in metabolomics. This is particularly important in isotopomer analysis with two-dimensional NMR with ^{13}C indirect detection, such as HSQC. Although uniformly sampled (US) HSQC retains the ^{1}H sensitivity, the carbon dimension resolution is insufficient, unless an impractically large number of increments is used. Moreover, such a measure inevitably decreases the relative signal-to-noise ratio, since the latter part of the indirect FID with much noise equally contributes to the final frequency domain data. A recent study used NUS to enhance the resolution in the indirect ^{1}H dimension and analyzed carbon isotopomers indirectly using the ^{1}H splitting by [1]H−[13]C J coupling.[24] However, it cannot be used to analyze the isotopomers of carbonyl carbons which are abundant in the core cell metabolisms such as the tricarboxylic acid (TCA) cycle and glycolysis.

Here, with hmsIST,[25] one of the fastest NUS approaches, we demonstrate that 2D NUS HSQC can give high resolution 2D data with very good resolution of carbon isotopomer multiplets. This enabled the detailed metabolomics flux analysis in L1210 leukemia cancer cells including metabolic pathway usages and TCA cycle efficiency. Because the carbon isotopomer information is obtained directly from the carbon dimension, the carbonyl carbon isotopomers could be also analyzed using [13]C−[13]C J splitting patterns on the adjacent aliphatic carbons. We also show that the short acquisition time makes it compatible for live metabolomics where metabolites are directly detected in living cells. We believe the NUS HSQC approach will be very valuable for detailed metabolomic analysis both with cell extracts and with live cells.

■ EXPERIMENTAL SECTION

Cell Lines and Culture Conditions. The mouse leukemia L1210 cells were purchased from American Type Culture Collection (ATCC) and cultured in high glucose (25 mM) DMEM medium (Welgene, Daegu, Korea) supplemented with 10% fetal bovine serum (FBS, Welgene, Daegu, Korea) and 1% penicillin−streptomycin solution (Gibco, Grand Island, NY). Cells were cultured at 37 °C in a 5% CO_2 humidified incubator.

Materials. The stable 1,2-[13]C_2 isotope-labeled sodium acetate (CLM-440-1,1,2-[13]C_2 99%) was purchased from Cambridge Isotope Laboratories (Andover, MA). D-(+)-Glucose solution (G8644, D-(+)-glucose 10%) and rotenone were obtained from Sigma-Aldrich (St. Louis, MO). The Mito-Xpress oxygen consumption measurement kit was obtained from Luxcel Biosciences (Cork, Ireland).

Sample Preparation. The sample preparation was adapted for suspension cultures from the live metabolomics approach for adherent cultures described previously.[26] Briefly, 5×10^7 L1210 cells were counted and resuspended with D-glucose-free DMEM media (Gibco, Grand Island, NY) supplemented with 10% dialyzed FBS (Welgene, Daegu, Korea), 1% penicillin−streptomycin solution, 5 mM unlabeled glucose, and 4 mM 1,2-[13]C_2-labeled sodium acetate. The resuspended L1210 cells were cultured at 37 °C and in a 5% CO_2 incubator overnight. After 24 h of incubation, 10^8 L1210 cells were counted and

resuspended with 500 μL of the culture media supplemented with 10% D_2O. The shigemi NMR tube containing the suspended L1210 cells was mildly centrifuged to sediment the live cells using a hand centrifuge. For rotenone treatment, 50 μM rotenone was added before the 24 h of incubation.

Metabolites Extraction. After the in-cell NUS HSQC acquisition, 2 mL of extraction mixture of methanol and acetonitrile (5:3) was added to the sample containing the cells and the media. The samples were centrifuged at 21 000g for 10 min at 4 °C. The supernatants were dried with a vacuum centrifugator (Vision, Seoul, Korea). The pellets were resuspended with 250 μL of buffer composed of 2 mM Na_2HPO_4 and 5 mM NaH_2PO_4 in D_2O with 0.025% TSP as an internal standard.

NMR Spectroscopy. The data were obtained with an 800 MHz Bruker Avance III HD spectrometer equipped with a 5 mm CPTCI CryoProbe (Bruker BioSpin, Germany). Non-uniform sampling-based 2D heteronuclear single quantum coherence (NUS HSQC) and US HSQC spectra were obtained with a Bruker pulse sequence hsqcetgpsisp2.2 provided with the TopSpin 3.5 pl5 version at 310 K. Spectral widths for both NUS and US HSQC were set to 16 ppm (^{1}H) and 39 ppm (^{13}C), the latter of which is to allow aliasing of the carbon signals for better digital resolution. The carrier frequency for the carbon dimension was set to 31.5 ppm. The acquisition data matrix had 1024 (T2) × 256 (T1) complex points for both NUS and US HSQC experiments. The number of NUS sampling points was 256 complex points (25% sampling density of 1024 points), and the time points were calculated with Schedule Generator 3.0 (available at http://gwagner.med.harvard.edu/intranet/hmsIST/gensched_new.html) with sinusoidal weighting. Each experiment had 12 scans per T1 increment with interscan delay of 1.0 s, which took approximately 2 h. We also took the long US HSQC with 4 times the number of points, i.e., 1024 (T2) × 1024 (4 × 256; T1) which took about 8 h.

The direct proton dimensions were processed in the same way for both NUS and US data. Zerofilling, shifted sine bell functions, and polynomial baseline correction were applied to the final 2048 points. For the indirect carbon dimensions, the NUS spectra were processed with the hmsIST[25] algorithm implemented as an nmrPipe function,[27] filling in the skipped data points (75%) with 400 iteration steps. The US data had a linear prediction to twice of the acquired points. Both NUS and US data were zerofilled to a final 4096 points and baseline corrected with polynomial functions.

Oxygen Consumption Assay. After 24-h incubation of cells with or without rotenone, 4×10^6 L1210 cells were resuspended with 150 μL prewarmed culture media and transferred to a 96 well plate. A 10 μL portion of Mito-Xpress, dissolved in 1 mL water, was added to each well, and 100 μL of prewarmed mineral oil was applied. The fluorescence was measured on a SpectraMax M5 microplate reader (Molecular Devices GmbH, München, Germany) every 2 min for 2 h (61 points).

■ RESULTS AND DISCUSSION

NUS Gives Higher Resolution for Homonuclear Carbon Splitting. To compare the resolution between the NUS and US HSQC NMR approaches, we obtained the spectra with both methods with comparable experimental acquisition time. We obtained 256 complex points using both methods and processed the data with Fourier transform (US) and hmsIST
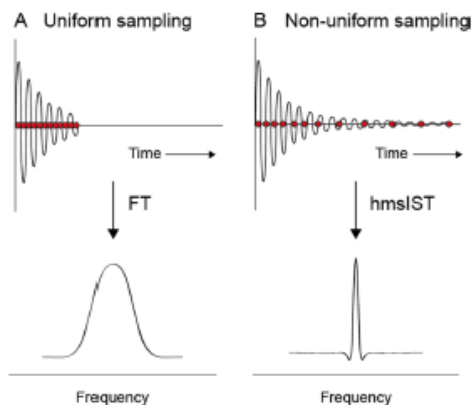
B

112

Figure 1. US and NUS strategies and the respective spectra. In this study, 256 complex points were acquired in both cases. NUS spectra were taken with 25% sampling density. The carbon dimension spectral width was set to 39 ppm with the carrier frequency at 31.5 ppm to allow aliasing for better digital resolution. The circles on the time domain data represent the acquired time points, and their numbers are not the same. The figures are not drawn to scale. (A) Uniform sampling method and the resulting peak shape with processing by Fourier transform (conventional processing method). (B) Non-uniform sampling and the resulting peak shape with processing by hmsIST (a customized method for NUS).

(NUS) (Figure 1). An acceptable NUS spectrum was reported with a sampling density as low as ~3% (compression rate of 32) in a previous study with a clean artificial mixture of standard samples.[23] In our case with a very complex mixture of cell lysate or even live cells, we chose 25% sampling density for the NUS to obtain more a quantitative isotopomer distribution, although 10% sampling density should give a good spectrum for a qualitative purpose. General spectral appearances, i.e., the number and patterns of the peaks, are very similar (Figure 2A,B). However, it was immediately clear that the NUS spectral peaks have fine structures along the carbon axis due to the much higher resolution (Figure 2A). As we used $1,2^{-13}C_2$-labeled acetate, these fine structures are due to carbon–carbon homonuclear J coupling between the adjacent carbons. The analysis of these coupling should give useful information on the flux of the metabolic pathways which cannot be obtained using simple analysis of nonresolved peak intensities. Although the US HSQC did show some fine structures with apparent splitting, the peaks from multiple isotopomers with different splitting patterns are little resolved, hindering proper analysis of the couplings (Figure 2C,D).

Assessment of Metabolite Usages in Different Metabolic Pathways. As NUS HSQC provided highly resolved carbon multiplet patterns, we analyzed them to investigate the metabolic usage of the acetate by the L1210 cells. First, we analyzed the multiplet patterns of aspartate α-carbon with both NUS and US HSQC. The carbon can be derived from acetate through sequential operation of TCA cycle and the transamination step (Figure 3A). Thus, analyzing the singlet and doublet structures can give information on how
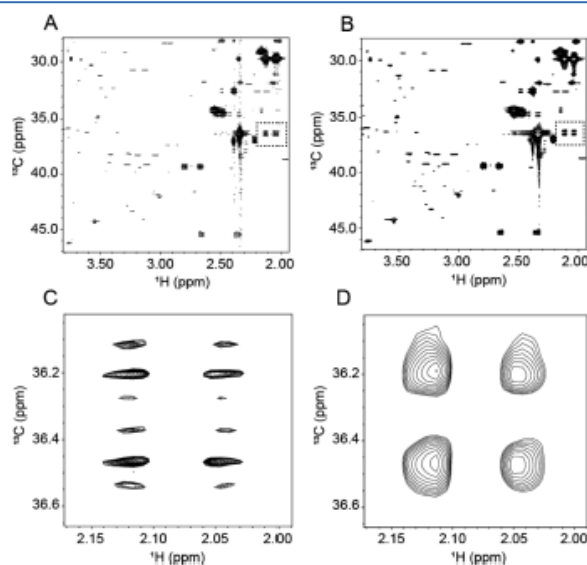
Figure 2. Comparison between NUS and US HSQC spectra. The lysate from L1210 cells labeled with 4 mM $1,2^{-13}C_2$ acetate was used for the NMR measurements. (A) Non-uniform sampling-based 2D heteronuclear single quantum coherence (NUS HSQC) spectrum. (B) Uniformly sampled 2D heteronuclear single quantum coherence (US HSQC) spectrum of the same sample. (C, D) Expansions of the dotted area of parts A and B, respectively.
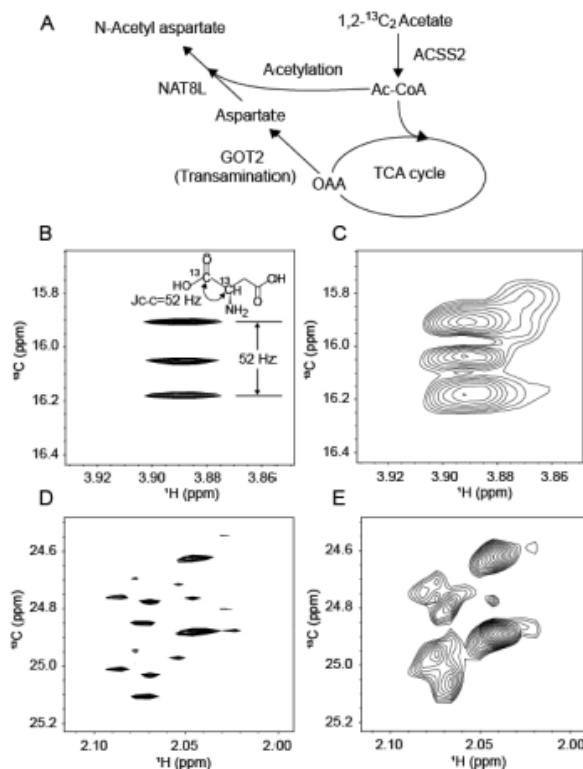
C

113

Figure 3. Isotope incorporation in N-acetylated metabolites and aspartate from $1,2\text{-}^{13}C_2$ acetate. (A) Biosynthetic metabolic pathways for aspartate and N-acetyl aspartate from acetate. (B) NUS HSQC and (C) US HSQC spectra of the α-carbon of aspartate. (D) NUS HSQC and (E) US HSQC spectra of the methyl group of the N-acetylated metabolites. The carbon dimension spectral width was set to 39 ppm with the carrier frequency at 31.5 ppm to allow aliasing for better digital resolution. The following abbreviations are used: NAT8L, N-acetyltransferase 8 like; GOT2, glutamic-oxaloacetic transaminase 2; ACSS2, acetyl-coenzyme A synthetase 2; OAA, oxaloacetate; Ac-CoA, acetyl coenzyme A.

much external acetate contributes to the aspartate biosynthesis. This has much biological importance, as recent reports showed critical roles for aspartate biosynthesis in cancer metabolism.[11,28] The NUS HSQC spectrum gave a completely resolved carbon splitting pattern, whereas the US HSQC exhibited broadly overlapped signals (Figure 3B,C). The volume measurement of the singlet, derived from preformed TCA intermediates or other pathways, and the doublet, from the external acetate, revealed that only about 3.7% of aspartate is derived from the external acetate source. This calculation took into consideration the natural abundance of the ^{12}C singlet (1%) relative to the ^{13}C doublet. The quantitative incorporation value was also obtained with a US HSQC spectrum with a 4 times longer acquisition time (4×256 complex points) matching the NUS HSQC's resolution. The overall spectral quality was very close to the NUS spectrum (Supporting Information Figure S1A,B), and the same quantitative analysis gave a 3.3% incorporation value, validating the analysis of the NUS spectrum (Supporting Information Figure S2A). The quantitative analysis was also tried on a

directly detected ^{13}C one-dimensional spectrum (Supporting Information Figure S2B), which was not successful due to the signal overlap. These clearly demonstrate the advantages of NUS HSQC over conventional methods. For a biosynthetic perspective, aspartate should be readily synthesized from other carbon sources such as glucose and glutamine, suggesting that glycolysis and glutamine anaplerosis are much more important in the aspartate synthesis in this experimental condition. Second, we analyzed the peaks for N-acetylated compounds which appear in a characteristic region of the spectrum (^1H = 2.02–2.10 and ^{13}C = 24.6–25.2 ppm). They exhibited well-resolved doublets with virtually no singlet (Figure 3D) as compared to the broadly overlapped peaks on US HSQC (Figure 3E). The apparently dominant peaks at 2.08 ppm on the US HSQC are from peaks fused with those at 2.07 ppm due to the low resolution. A US HSQC spectrum with 4 times the acquisition time matching the NUS's resolution exhibited a very similar peak pattern with the NUS spectrum (Supporting Information Figure S3A,B). As the singlet is from 1% natural abundance ^{13}C carbon, it is possible that small amounts of N-
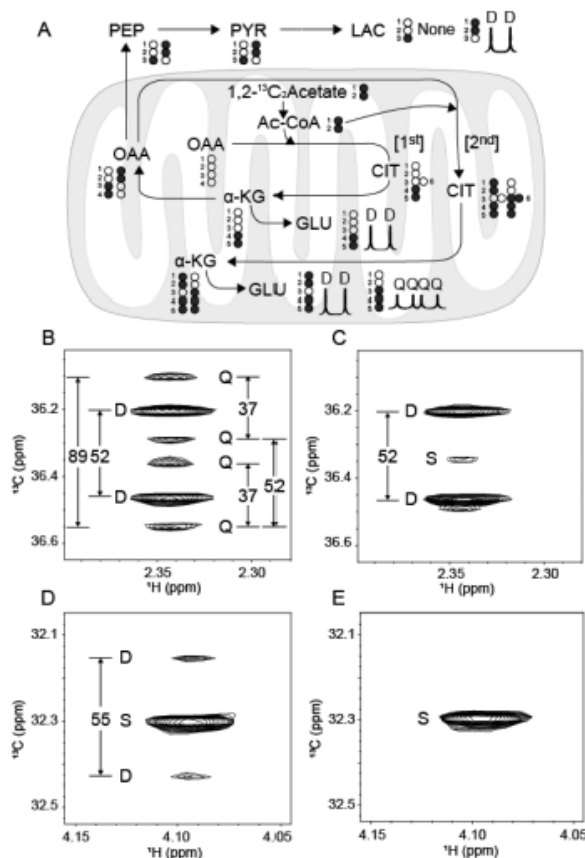
D

114

Figure 4. TCA cycle turn efficiency changes by rotenone treatment. (A) Isotope incorporation patterns of lactate and glutamate in relation to the TCA cycle. Open and filled circles represent ^{12}C and ^{13}C carbon atoms, respectively. The numbers represent the carbon position. (B–E) Singlet (S), doublet (D), and quartet (Q) represent the carbon splitting patterns of particular isotopomers. Glutamate C4 splitting in the absence (B) and presence (C) of rotenone (50 μM). Lactate C2 splitting in the absence (D) and presence (E) of rotenone (50 μM). The numbers on the spectra represent the splitting in Hertz. The carbon dimension spectral width was set to 39 ppm with the carrier frequency at 31.5 ppm to allow aliasing for better digital resolution. Abbreviations used here follow: LAC, lactate; PYR, pyruvate; PEP, phosphoenolpyruvate; OAA, oxaloacetate; CIT, citrate; α-KG, α-ketoglutarate; GLU, glutamate.

acetylated compounds from other unlabeled precursors were not detected due to low intensity. Still, the result clearly shows that the acetate incorporation into N-acetylated compounds is much higher than that into aspartate. Thus, acetate goes through the N-acetylation pathway much more readily than the TCA cycle followed by the transamination pathway (see Figure 3A), and the NUS approach can provide information on relative acetate usage for different metabolic pathways.

Estimation of the TCA Cycle Efficiency. The high resolution of NUS HSQC can also be exploited to investigate how the TCA cycle efficiency is affected by different cellular conditions. The isotope incorporation patterns from labeled acetate, and thus the splitting, of relevant TCA metabolites depend on the number of turns of the TCA cycle (Figure 4A).

Here, we analyzed the multiplet patterns of glutamate C4 carbon in the presence or absence of rotenone, an inhibitor of mitochondrial oxidative phosphorylation (OXPHOS), using NUS HSQC (Supporting Information Figure S4A,B). In the absence of rotenone, the C4 peak exhibited the mixture status of a quartet (Q; by J_{C-C} with ^{13}C3 and carbonyl ^{13}C5) and a doublet (D; by J_{C-C} with carbonyl ^{13}C5) (Figure 4B). As a quartet can be only from glutamate that has gone through two cycles of TCA cycle, the results show that acetate has been incorporated into the TCA cycle twice (see Figure 4A). In comparison, the rotenone-treated cells exhibited the mixture of a singlet and doublet without a quartet (Figure 4C). As a singlet is from endogenous sources and a doublet can be from the first turn of the TCA cycle, the absence of a quartet shows that the
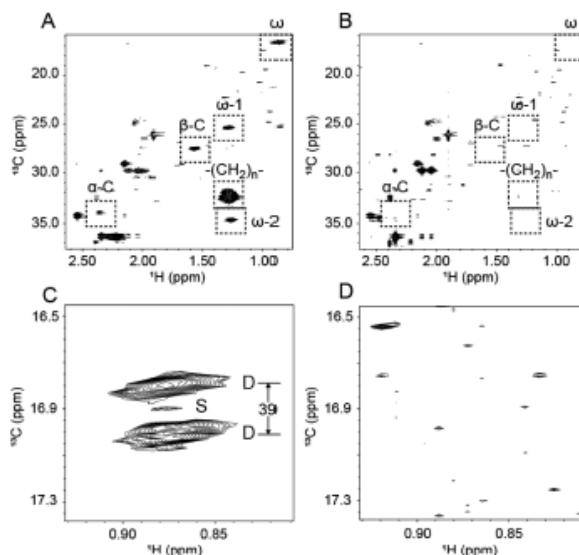
E

Figure 5. NUS HSQC spectra for fatty acid peaks from live L1210 cells and cell lysate with $1,2\text{-}^{13}C_2$ acetate labeling. (A) NUS HSQC spectrum of live L1210 cells labeled with 4 mM $1,2\text{-}^{13}C_2$ acetate. (B) NUS HSQC spectrum of the L1210 cell lysate. (A and B) Dotted boxes represent peaks from fatty acids. Peaks for the ω-position of fatty acids from the (C) live cell and the (D) extract spectra. The spectra were acquired in 1 h and 39 min to ascertain the viability of the cells in the NMR tube.

labeled acetate entered the TCA cycle only once. Therefore, these data show that rotenone effectively lowered the number of turns of the TCA cycle, which is consistent with a well-known idea that inhibition of mitochondrial oxidative phosphorylation suppresses the TCA cycle. The low efficiency of the TCA cycle could be also observed in the lactate peak splitting. The lactate α-carbon (C2) doublet (by J_{C-C} with carbonyl $^{13}C1$) can be only observed from that synthesized through oxaloacetate, a TCA intermediate, phosphoenolpyruvate (PEP), and pyruvate (see Figure 4A). The rotenone treatment effectively blocked the doublet signal and gave only a singlet which is from endogenous sources without the entry of the labeled acetate into the TCA cycle (Figure 4D,E). This is consistent with the lower efficiency of the TCA cycle shown by glutamate C4 splitting above. Although we analyzed the TCA cycle turn efficiency with an OXPHOS inhibitor, the approach can be straightforwardly applied to understanding how a variety of physiological conditions such as hypoxia, oncogene activation, or nutrient depletion can affect the TCA efficiency. Our approach also provided the ^{13}C incorporation status of the carbonyl carbons of glutamate C5 and lactate C1. These isotope incorporations into carbonyl carbons may not be available from the recently described NUS approach involving the splitting of ^{1}H atoms directly attached to ^{13}C atoms.[24] Therefore, our approach should be useful in analyzing core cell metabolisms, such as TCA and glycolysis, where most metabolites have carboxylic acid moieties.

Application of NUS to Live Metabolomics and Lipid Analysis. The NUS approach can also be applied to live metabolomics that we recently described,[26] allowing the detection of the carbon splitting in living cells. In observing the live L1210 cells, we noticed that live metabolomics gives many additional signals that are not visible in the usual cell lysate spectrum (Figure 5A,B). From the database search and standard sample spiking, these signals were found to arise from lipid metabolites such as fatty acids. A commonly used extraction solvent system for cell lysate metabolomics (methanol–acetonitrile–water) cannot solubilize these metabolites due to their high lipophilicity. A two phase extraction system (chloroform–methanol–water) is generally used for lipid soluble metabolites, but the approach generates two samples that need to be analyzed separately. The NUS spectrum on live cells exhibits both hydrophilic metabolites, i.e., glutamate and lactate, and lipophilic metabolites in one spectrum, allowing convenient and error-less analysis of metabolism. A unique advantage of this approach is the splitting of lipid signals appearing on different regions of the spectrum according to the carbon positions along the fatty acid chains. These signals should be from mobile fatty acids rather than membrane bound lipids, as the latter have limited mobility and very short T2 values. For example, the terminal methyl signal (ω-position) of free fatty acids appears at the characteristic position of $^{1}H = 0.87$, $^{13}C = 16.9$ ppm. Fatty acid biosynthesis always starts from the carbonyl position, and therefore, ^{13}C labeling at the ω-position can only occur for *de novo* fatty acid synthesis but not for chain elongation reactions. The analysis on the methyl carbon splitting in our data (Figure 5C) shows that 22% of the fatty acids were synthesized *de novo* from the labeled acetate and that the rest is from other sources. Again, the peak was not visible on the spectrum of the cell lysate extracted with a common extraction solvent (Figure 5D). In addition, this position-dependent isotope incorporation may

F

116

not be analyzed by mass-spectrometry-based metabolomics methods. The information on fatty acid *de novo* synthesis may have important implications for cancer cell metabolism, as some solid tumor cells were recently shown to be able to use external acetate as an important carbon source for fatty acids through an enzyme acyl-CoA synthetase (ACSS2).[29,30] It may be interesting to see if the same metabolic rewiring is also activated in leukemia cells when glucose is limited.

■ CONCLUSIONS

Overall, we used NUS HSQC to obtain high resolution ^{13}C dimension spectra retaining the high sensitivity of ^1H NMR. The ^{13}C dimension splitting patterns enabled us to directly analyze carbon isotopomers of core cellular metabolic pathways including those with carbonyl carbons. Detailed biological metabolic information such as differential metabolic pathway usages and the efficiency of the TCA cycle turns could be obtained by isotopomer analysis. In addition, the NUS HSQC approach was used to observe lipid isotopomers directly in live cells without solvent extraction. It gave carbon-position-dependent isotopomer information that is important in estimating *de novo* fatty acid biosynthesis. Isotopomer analysis in live cells and the position-dependent information constitute advantages of NUS HSQC that are not available from mass-spectrometry-dependent isotopomer analysis. Our approach is simple and can be straightforwardly extended to a variety of cellular systems where metabolism is affected by environmental or inherent conditions.

■ ASSOCIATED CONTENT

⑤ Supporting Information

The Supporting Information is available free of charge on the ACS Publications website at DOI: 10.1021/acs.analchem.6b02107.

    Additional spectra and oxygen consumption plot (PDF)

■ AUTHOR INFORMATION

Corresponding Author

*Phone:+82-2-880-7831. Fax: +82-2-880-7831. E-mail: psh@snu.ac.kr.

ORCID ⑩

Sunghyouk Park: 0000-0003-1981-3274

Notes

The authors declare no competing financial interest.

■ REFERENCES

(1) Raffler, J.; Friedrich, N.; Arnold, M.; Kacprowski, T.; Rueedi, R.; Altmaier, E.; Bergmann, S.; Budde, K.; Gieger, C.; Homuth, G.; Pietzner, M.; Romisch-Margl, W.; Strauch, K.; Volzke, H.; Waldenberger, M.; Wallaschofski, H.; Nauck, M.; Volker, U.; Kastenmuller, G.; Suhre, K. *PLoS Genet.* **2015**, *11*, e1005487.

(2) Gowda, G. A.; Tayyari, F.; Ye, T.; Suryani, Y.; Wei, S.; Shanaiah, N.; Raftery, D. *Anal. Chem.* **2010**, *82*, 8983−8990.

(3) Moreno, K. X.; Satapati, S.; DeBerardinis, R. J.; Burgess, S. C.; Malloy, C. R.; Merritt, M. E. *J. Biol. Chem.* **2014**, *289*, 35859−35867.

(4) Holmes, E.; Loo, R. L.; Stamler, J.; Bictash, M.; Yap, I. K.; Chan, Q.; Ebbels, T.; De Iorio, M.; Brown, I. J.; Veselkov, K. A.; Daviglus, M. L.; Kesteloot, H.; Ueshima, H.; Zhao, L.; Nicholson, J. K.; Elliott, P. *Nature* **2008**, *453*, 396−400.

(5) Wen, H.; Yoo, S. S.; Kang, J.; Kim, H. G.; Park, J. S.; Jeong, S.; Lee, J. I.; Kwon, H. N.; Kang, S.; Lee, D. H.; Park, S. *J. Hepatol.* **2010**, *52*, 228−233.

(6) McPhail, M. J.; Shawcross, D. L.; Lewis, M. R.; Coltart, I.; Want, E. J.; Antoniades, C. G.; Veselkov, K.; Triantafyllou, E.; Patel, V.; Pop, O.; Gomez-Romero, M.; Kyriakides, M.; Zia, R.; Abeles, R. D.; Crossey, M. M.; Jassem, W.; O'Grady, J.; Heaton, N.; Auzinger, G.; Bernal, W.; Quaglia, A.; Coen, M.; Nicholson, J. K.; Wendon, J. A.; Holmes, E.; Taylor-Robinson, S. D. *J. Hepatol.* **2016**, *64*, 1058−1067.

(7) Bertini, I.; Cacciatore, S.; Jensen, B. V.; Schou, J. V.; Johansen, J. S.; Kruhoffer, M.; Luchinat, C.; Nielsen, D. L.; Turano, P. *Cancer Res.* **2012**, *72*, 356−364.

(8) Chikayama, E.; Sekiyama, Y.; Okamoto, M.; Nakanishi, Y.; Tsuboi, Y.; Akiyama, K.; Saito, K.; Shinozaki, K.; Kikuchi, J. *Anal. Chem.* **2010**, *82*, 1653−1658.

(9) Lewis, I. A.; Schommer, S. C.; Hodis, B.; Robb, K. A.; Tonelli, M.; Westler, W. M.; Sussman, M. R.; Markley, J. L. *Anal. Chem.* **2007**, *79*, 9385−9390.

(10) Birsoy, K.; Wang, T.; Chen, W. W.; Freinkman, E.; Abu-Remaileh, M.; Sabatini, D. M. *Cell* **2015**, *162*, 540−551.

(11) Cardaci, S.; Zheng, L.; MacKay, G.; van den Broek, N. J.; MacKenzie, E. D.; Nixon, C.; Stevenson, D.; Tumanov, S.; Bulusu, V.; Kamphorst, J. J.; Vazquez, A.; Fleming, S.; Schiavi, F.; Kalna, G.; Blyth, K.; Strathdee, D.; Gottlieb, E. *Nat. Cell Biol.* **2015**, *17*, 1317−1326.

(12) Vincent, E. E.; Sergushichev, A.; Griss, T.; Gingras, M. C.; Samborska, B.; Ntimbane, T.; Coelho, P. P.; Blagih, J.; Raissi, T. C.; Choiniere, L.; Bridon, G.; Loginicheva, E.; Flynn, B. R.; Thomas, E. C.; Tavare, J. M.; Avizonis, D.; Pause, A.; Elder, D. J.; Artyomov, M. N.; Jones, R. G. *Mol. Cell* **2015**, *60*, 195−207.

(13) Fan, T. W.; Lane, A. N. *Prog. Nucl. Magn. Reson. Spectrosc.* **2016**, *92−93*, 18−53.

(14) Szyperski, T.; Glaser, R. W.; Hochuli, M.; Fiaux, J.; Sauer, U.; Bailey, J. E.; Wuthrich, K. *Metab. Eng.* **1999**, *1*, 189−197.

(15) Chikayama, E.; Suto, M.; Nishihara, T.; Shinozaki, K.; Kikuchi, J.; Hirayama, T. *PLoS One* **2008**, *3*, e3805.

(16) Mendes, A. C.; Caldeira, M. M.; Silva, C.; Burgess, S. C.; Merritt, M. E.; Gomes, F.; Barosa, C.; Delgado, T. C.; Franco, F.; Monteiro, P.; Providencia, L.; Jones, J. G. *Magn. Reson. Med.* **2006**, *56*, 1121−1125.

(17) Lapidot, A.; Gopher, A. *J. Biol. Chem.* **1994**, *269*, 27198−27208.

(18) Gorietti, D.; Zanni, E.; Palleschi, C.; Delfini, M.; Uccelletti, D.; Saliola, M.; Puccetti, C.; Sobolev, A. P.; Mannina, L.; Miccheli, A. *Biochim. Biophys. Acta, Gen. Subj.* **2015**, *1850*, 2222−2227.

(19) Hyberts, S. G.; Arthanari, H.; Robson, S. A.; Wagner, G. *J. Magn. Reson.* **2014**, *241*, 60−73.

(20) Kazimierczuk, K.; Orekhov, V. *Magn. Reson. Chem.* **2015**, *53*, 921−926.

(21) Pudakalakatti, S. M.; Dubey, A.; Jaipuria, G.; Shubhashree, U.; Adiga, S. K.; Moskau, D.; Atreya, H. S. *J. Biomol. NMR* **2014**, *58*, 165−173.

(22) Guennec, A. L.; Giraudeau, P.; Caldarelli, S. *Anal. Chem.* **2014**, *86*, 5946−5954.

(23) Le Guennec, A.; Dumez, J. N.; Giraudeau, P.; Caldarelli, S. *Magn. Reson. Chem.* **2015**, *53*, 913−920.

(24) Reardon, P. N.; Marean-Reardon, C. L.; Bukovec, M. A.; Coggins, B. E.; Isern, N. G. *Anal. Chem.* **2016**, *88*, 2825−2831.

(25) Hyberts, S. G.; Milbradt, A. G.; Wagner, A. B.; Arthanari, H.; Wagner, G. *J. Biomol. NMR* **2012**, *52*, 315−327.

G

117

(26) Wen, H.; An, Y. J.; Xu, W. J.; Kang, K. W.; Park, S. *Angew. Chem., Int. Ed.* **2015**, *54*, 5374−5377.

(27) Delaglio, F.; Grzesiek, S.; Vuister, G. W.; Zhu, G.; Pfeifer, J.; Bax, A. *J. Biomol. NMR* **1995**, *6*, 277−293.

(28) Sullivan, L. B.; Gui, D. Y.; Hosios, A. M.; Bush, L. N.; Freinkman, E.; Vander Heiden, M. G. *Cell* **2015**, *162*, 552−563.

(29) Mashimo, T.; Pichumani, K.; Vemireddy, V.; Hatanpaa, K. J.; Singh, D. K.; Sirasanagandla, S.; Nannepaga, S.; Piccirillo, S. G.; Kovacs, Z.; Foong, C.; Huang, Z.; Barnett, S.; Mickey, B. E.; DeBerardinis, R. J.; Tu, B. P.; Maher, E. A.; Bachoo, R. M. *Cell* **2014**, *159*, 1603−1614.

(30) Comerford, S. A.; Huang, Z.; Du, X.; Wang, Y.; Cai, L.; Witkiewicz, A. K.; Walters, H.; Tantawy, M. N.; Fu, A.; Manning, H. C.; Horton, J. D.; Hammer, R. E.; McKnight, S. L.; Tu, B. P. *Cell* **2014**, *159*, 1591−1602.

118

Glucose-derived acetate and ACSS2 as key players in cisplatin resistance in bladder cancer

He Wen[a,1], Sujin Lee[b,1], Wei-Guo Zhu[a], Ok-Jun Lee[c], Seok Joong Yun[d], Jayoung Kim[e,f,*],
Sunghyouk Park[b,**]

[a] Guangdong Key Laboratory for Genome Stability and Human Disease Prevention, Department of Biochemistry and Molecular Biology, Shenzhen University School of Medicine, Shenzhen 518060, China
[b] College of Pharmacy, Natural Product Research Institute, Seoul National University, Seoul 151-742, South Korea
[c] Department of Pathology, College of Medicine and Institute for Tumor Research, Chungbuk National University, Cheongju, Chungbuk 361-711, South Korea
[d] Department of Urology, College of Medicine and Institute for Tumor Research, Chungbuk National University, Cheongju, Chungbuk 361-711, South Korea
[e] Departments of Surgery and Biomedical Sciences, Cedars-Sinai Medical Center, Los Angeles, CA 90048, USA
[f] Department of Medicine, University of California, Los Angeles, CA 90095, USA

ARTICLE INFO

ABSTRACT

Cisplatin is an important chemotherapeutic agent against metastatic bladder cancer, but resistance often limits its usage. With the recent recognition of lipid metabolic alterations in bladder cancers, we studied the metabolic implications of cisplatin resistance using cisplatin-sensitive (T24S) and resistant (T24R) bladder cancer cells. Real-time live metabolomics revealed that T24R cells consume more glucose, leading to higher production of glucose-derived acetate and fatty acids. Along with the activation of general metabolic regulators, enzymes involved in acetate usage (ACSS2) and fatty acid synthesis (ACC) and a precursor for fatty acid synthesis (acetyl-CoA) were elevated in T24R cells. Consistently, metabolic analysis with ^{13}C isotope revealed that T24R cells preferred glucose to acetate as the exogenous carbon source for the increased fatty acid synthesis, contrary to T24S cells. In addition, ACSS2, rather than the well-established ACLY, was the key enzyme that supplies acetyl-CoA in T24R cells through glucose-derived endogenous acetate. The relevance of ACSS2 in cisplatin resistance was further confirmed by the abrogation of resistance by an ACSS2 inhibitor and, finally, by the higher expression of ACSS2 in the patient tissues with cisplatin resistance. Our results may help improve the treatment options for chemoresistant bladder cancer patients and provide possible vulnerability targets to overcome the resistance.

1. Introduction

Bladder cancer (BC) usually arises in the bladder epithelial lining, and is the seventh most common cancer for men worldwide [1–3]. A majority of BC cases (~90%) are classified as transitional cell carcinoma (TCC), which can be further categorized as non-muscle invasive (NMIBC) or muscle invasive bladder cancer (MIBC), according to the extent of invasion into the muscular layer. NMIBC exhibits better prognosis and survival rate, but about 20% of those patients progress to MIBC [4, 5]. Radical cystectomy is a standard treatment for MIBC, but about 50% of the patients develop distant metastases within two years. For metastatic BC, cisplatin-based chemotherapy, with or without radiotherapy, is the current gold standard. Those who do not respond well to this treatment generally have a poor prognosis [6].

It is well established that cisplatin kills rapidly proliferating cancer cells mostly through DNA damages [7]. It generates intra- and inter-strand purine crosslinks that interferes with DNA replication, which eventually lead to apoptosis. The toxicity mechanism, especially for kidney, has also been reported as involving the generation of reactive oxygen species and oxidative stress [8]. However, the biochemical processes underlying its resistance are more complex and may involve various signaling pathways such as p53, PI3K/AKT, and ROS detoxification [9]. In addition, the contribution of these individual mechanisms may differ according to the particular tumors involved.

Recent results suggest that not only these well-established cell signaling mechanisms, but also metabolic activities may be involved in cisplatin-induced cell death [10]. For example, differences in succinate dehydrogenase-mediated production of NADPH generation may be responsible for pharmacometabonomic heterogeneity of cisplatin-induced kidney toxicity [11]. In addition, the level of UDP-GlcNAc, the metabolite involved in N-acetylglucosmaine glycosylation, was shown to correlate with cisplatin sensitivity of cancer cells [12]. As metabolism is increasingly recognized as involved in cancer initiation and progression [13], metabolic study of cisplatin resistance may lead to clues for improving therapies for refractory bladder cancer.

Among key metabolites that fuel cancer cell proliferation, acetate has not drawn as much attention as glucose and glutamine [14]. Recent studies, however, have found acetate to be a key substrate for cancer bioenergetics or macromolecular synthesis [15, 16]. In addition, increased usages of ^{11}C-aceate positron emission tomography in clinics provide proof of concept evidence for the importance of acetate metabolism in cancer [17]. At the heart of acetate utilization in cancer is the enzyme ACSS2, responsible for converting acetate to acetyl-CoA. Production of acetyl-CoA is critical for the upkeep of fatty acid synthesis in cancer cells [14]. Fatty acid metabolism is a critical aspect of cancer metabolism, as cancer cell proliferation requires large amount of biomass. It is also interesting to note that bladder cancer may also have alterations in lipid or fatty acid metabolism [18–21]. Despite this interesting relationship among acetate, fatty acid, and cancer metabolism, the exact source of acetate in cancer cells is still debatable due to the low blood concentration of acetate.

In this study, we applied real-time live metabolomics to identify metabolic reprogramming in cisplatin-resistant bladder cancer cells and verified the results in patient-derived tissues. Our findings may reveal a new aspect of the acquired chemoresistance and vulnerabilities to overcome the resistance.

2. Materials and methods

2.1. Chemicals and reagents

The stable isotope labeled D-Glucose (U-^{13}C$_6$, 99%) and acetate (1,2-^{13}C, 99%) were purchased from Cambridge Isotope Laboratories (Andover, MA, USA). The standard compounds, including pyruvate, lactate, alanine, acetate, succinate, glucose, palmitate, glycine, glutamate, isoleucine, valine, leucine, and glutathione(reduced) were obtained from Sigma-Aldrich (St. Louis, MO, USA). The inhibitors for ACSS2, 1-(2,3-di(thiophen-2-yl)quinoxalin-6-yl)-3-(2-methoxyethyl) urea, and for ACLY, 3,5-Dichloro-2-hydroxy-N-(4-methoxy[1,1′-biphenyl]-3-yl)-benzenesulfonamide (BMS-303141), were purchased from ChemBridge (San Diego, CA, USA) and Bio-Techne (Minneapolis, MN, USA), respectively. The following antibodies, β-Actin (A1978, 1:5000) from Sigma, ACSS2 (PA5-52059, 1:1000) from Thermo Fisher Scientific, were used. All other antibodies, ACC (3676, 1:750), FAS (3180, 1:750), EGFR (2232; 1:1000), phospho-EGFR (Tyr1068) (3777; 1:1000), Src (2108; 1:750), phospho-Src (Tyr527) (2105; 1:1000), mTOR (2983; 1:1000), phospho-mTOR (Ser2448) (5536; 1:1000), and HRP-conjugated secondary antibodies (7074, 1:1000; 7076, 1:1000) were obtained from Cell Signaling Technologies.

2.2. Cell culture and biochemical assays

T24S and T24R urothelial carcinoma cells were cultured in DMEM supplemented with 10% FBS, 2 mM L-glutamine, and 1% antibiotic solution (all from Invitrogen, Carlsbad, CA). All cells were maintained in a humidified incubator (37 °C and 5% CO$_2$). Cisplatin-resistant bladder cancer cells (T24R) were obtained through chronic treatments of cisplatin at low doses over six months [22, 23]. Briefly, the final cell viability was < 40% for T24S cells and nearly 100% for T24R cells upon 10 μM cisplatin treatment for 12 h. Cell viability assay was

performed using MTS (Promega, Inc., Madison, WI) according to the manufacturer's protocol. Western blot analysis was performed following routine procedures with actin as normalization control.

2.3. Sample preparation for live NMR metabolomics

Six plates (100 mm) of 70% confluent cultured cells were harvested with centrifugation. After the re-suspension of the cells with 5 mL DPBS, cells were counted, and 3×10^7 cells were moved into a new tube. After centrifugation, the harvested cells were re-suspended with 500 μL glucose-free DMEM media (Gibco, Grand Island, NY, USA) supplemented with 10% dialyzed FBS (Welgene, Daegu, Korea), 25 mM ^{13}C$_6$-labeled glucose, and 10% D$_2$O. The cells were spun in an NMR tube with a weak centrifugal force (30g for 100 s) to allow sedimentation, enough to cover the active region of the NMR detection coil. The NMR tubes with the cells were inserted into NMR magnet and the spectra were acquired as usual.

2.4. Isotope incorporation analysis for fatty acids

The T24S and T24R cells were counted (5×10^6) and seeded in 6-well plates. After 24 h adaptation, cells were treated with glucose-free DMEM media (Gibco, Grand Island, NY, USA) supplemented with 10% dialyzed FBS (Welgene, Daegu, Korea), and 5 mM non-labeled glucose. For the ^{13}C-acetate and ^{13}C-glucose treatment, 0.5 mM [1,2-^{13}C] acetate and 20 mM [U-^{13}C] glucose was added, respectively. For the inhibitor treatment, the ACSS2 inhibitor (15.6 μM) and the ACLY inhibitor (32 μM) were also added to the cell media. After a 24 h treatment, the fatty acids were extracted from the counted (9.05×10^6) cells using the two-layer methanol-chloroform extraction method as previously described [24].

2.5. NMR measurement

^{1}H-^{13}C Heteronuclear Single Quantum Coherence (HSQC) NMR spectra were measured on a 800-MHz Bruker Avance spectrometer (Bruker BioSpin, Rheinstetten, Germany) equipped with a cryogenic triple resonance probe at Seoul National University, Korea. The dataset comprises 1024×128 points for the direct and indirect dimensions, respectively. The time course spectral measurement was obtained at 310 K for 24 time points, with each experiment lasting for 288 s. Each of the metabolites was identified by spiking the standard compounds. Metabolites were quantified as described previously [25]. Non-uniformly sampled HSQC (NUS-HSQC) were obtained as described previously [26].

2.6. Quantification of acetyl-CoA

The levels of acetyl-CoA were measured from cell lysates using PicoProbe™ Acetyl-CoA Assay Kit (BioVision, Milpitas, CA), following the protocol provided by the manufacturer. Briefly, free CoA was quenched, and then Acetyl-CoA was converted to CoA. The CoA was then reacted to form NADH which interacts with PicoProbe, resulting in the fluorescence. The reading was done with Ex = 535/Em = 587 nm.

2.7. Immunohistochemistry (IHC) analysis

To stain the slides of bladder tumor tissues obtained from BC patients showing complete remission (CR) or progressive disease (PD), the ACSS2 antibody (1:100, LifeSpan Biosciences, Inc., Seattle, WA) was utilized. A high pH was used for the antigen retrieval and an Ultraview DAB Detection Kit from Ventana Medical Systems was used for counterstaining. To acquire the digital images, stained slides were scanned using an Aperio Turbo Scanscope AT machine (Leica Biosystems, Buffalo Grove, IL). High-resolution images of each slide were uploaded onto the Leica Biosystems cloud drive for further annotations and

analysis. Digitized images were analyzed with the Tissue IA Optimiser (Leica Biosystems, Buffalo Grove, IL) software installed on the Leica Digital Image Hub. Following pathological annotations, the Measure Stained Cells Algorithm option on the Leica Tissue IA software was used. Each annotated slide had a minimum threshold of 100,000 cells to be analyzed. After analysis, data for the nuclear h-score, % of positive nuclei, and % of positive nuclear area in tissue were collected and used for comparative graphing.

2.8. Routine statistics

All functional validation experiments were repeated at least three times. Data were compared using Student's t-tests. $P < 0.05$ was considered to be statistically significant.

3. Results

3.1. Live metabolomics comparison between cisplatin-sensitive and resistant bladder cancer cells

Through several metabolomics studies, it has been found that bladder cancers may have abnormalities in metabolites involved in lipid usages [18, 21]. It has been also suggested that perturbed metabolism may have implication in cancer drug resistance and cancer aggressiveness or progression [27]. We hypothesized that there should be differences in metabolism and metabolism-associated pathways between cisplatin-sensitive and resistant bladder cancer cells. To test the possibility, we applied the live metabolomics approach that we recently developed [24] to isogenic bladder cancer cell lines T24S (cisplatin-sensitive) and T24R (cisplatin-resistant) [22]. The metabolites generated from ^{13}C-glucose tracer were monitored with 2D ^{1}H-^{13}C HSQC NMR in real-time (Fig. 1A and B). By spiking the spectra with standard compounds, we obtained the peak assignments for those with significant changes (Supplementary Table S1). Along with the peaks for metabolites involved in glycolysis, pyruvate metabolism and the TCA cycle, those corresponding to fatty acids could be readily identified. This was possible by the live metabolomics, since lipid-soluble fatty acids and water-soluble polar metabolites are usually not quantifiable in a single analysis with conventional cell lysate metabolomics [26].

3.2. Cisplatin resistance may be linked to the increased glucose consumption and acetate production

The time-dependent changes of these metabolites revealed that T24R cells exhibited specific metabolic characteristics in comparison with T24S cells. Glucose consumption was greater in T24R cells, indicating the higher input to glycolysis in T24R cells (Fig. 1C). The level of pyruvate, the last glycolytic metabolite prior to the TCA cycle, became almost the same, just after the brief higher consumption at an early period in T24R cells (Fig. 1D). Lactate, alanine and acetate all exhibited net productions in both cells, but there was an intriguing difference. Lactate and alanine accumulated faster and to higher levels in T24S than T24R cells (Fig. 1E and F), while acetate accumulated much faster and kept the much higher level throughout in T24R cells (Fig. 1G). In addition, despite the higher consumption of glucose in T24R cells, lactate production and excretion was significantly lower, (Fig. 1E and Supplementary Fig. S1). These findings suggest that the preferred metabolic route of the increased glucose consumption in T24R cells is not lactate formation, as occurs in Warburg-type metabolism, but it may be other metabolites generated through acetate. One possible destination may be fatty acids, because the fatty acid level was also higher in T24R cells, as estimated by their mid-chain CH_2 peak intensities (Fig. 1H). For other metabolites, glycine, a possible indicator of one carbon metabolism, and glutamate, an important anaplerotic metabolite to TCA, exhibited no significant difference in the two cells (Fig. 1I and J).

3.3. Two carbon pathway involving acetate leading to fatty acid synthesis is enhanced in the cisplatin-resistant T24 cells

We took notice of the differential patterns of changes of acetate in comparison with lactate and alanine between T24S and T24R cells. These three downstream metabolites from pyruvate exhibited similar patterns of changes in our previous live metabolomics studies with liver cells [24]. In addition, lactate and alanine retain all three carbons from pyruvate, whereas acetate is formed through the loss of one carbon from pyruvate. With these unique characteristics of acetate and the higher ^{13}C-fatty acid level in T24R cells, we hypothesized that there might be an alteration in pathways of fatty acid metabolism involving acetate. To test this hypothesis, we first looked at the levels of the upstream signaling molecules that can affect fatty acid metabolism. Significant increase in the phosphorylated EGFR and mTOR in T24R without much increase in their total levels suggested that cisplatin resistance is associated with the activation of upstream metabolic regulators (Fig. 2A). Then, looking at more downstream enzymes, we found that acetyl-CoA carboxylase (ACC), a key enzyme synthesizing malonyl-CoA from acetyl-CoA, is expressed much higher in T24R cells (Fig. 2B). Malonyl-CoA is a direct substrate of fatty acid synthase (FAS) which was present at similar levels in both cells (Fig. 2B). For the involvement of acetate in the fatty acid synthesis, we measured ACSS2 levels, as it is a key enzyme in pathways for incorporating acetate into fatty acids. The ACSS2 level was much higher in T24R cells (Fig. 2C), which was also corroborated by the higher level of acetyl-CoA generated from acetate by ACSS2 (Fig. 2D). Given that ACC and ACSS2 are two major enzymes that incorporate the acetate into fatty acids, our experimental results suggest that T24R may have the enhanced fatty acid synthesis via two carbon metabolism involving acetate.

3.4. Glucose-derived endogenous acetate contributes to the enhanced fatty acid de novo synthesis in T24R cells

The metabolic flux through a particular step can increase significantly even with a constant enzyme level, as long as there is an increased supply of the substrates. We observed activation of the acetate-involving two carbon metabolism leading to the FAS step in T24R cells despite similar FAS levels in T24S and T24R cells (see Fig. 2B). Therefore, we tested if the actual fatty acid de novo synthesis is increased and correlated with the activation of the acetate-involving two carbon metabolism in T24R cells. The de novo fatty acid synthesis was assessed by measuring the splitting of the omega methyl carbon signal arising from ^{13}C-^{13}C coupling in the HSQC spectra obtained with ^{13}C-glucose tracer. This is possible because ^{13}C labels from a glucose-derived two carbon unit are incorporated into the omega methyl group for de novo fatty acid synthesis (Fig. 3A). In comparison, fatty acid chain elongation starting from a pre-existing fatty acyl chain occurs only at the carboxyl terminal end. The intensities of the splitting doublet of the omega methyl group of fatty acids, derived from the tracer glucose, were much higher in T24R (Fig. 3B), indicating elevated de novo fatty acid synthesis from glucose in T24R. Combined with the above results for the increased acetate production from glucose and higher levels of ACSS2, ACC and acetyl-CoA, this indicates that an acetate-involving two carbon unit from glucose should contribute to the enhanced fatty acid synthesis in T24R cells.

Since previous studies emphasized the roles of blood-borne exogenous acetate, not glucose-derived endogenous, in the bioenergetics or lipid biosynthesis [15, 16], we also tested the de novo fatty acid synthesis from exogenous ^{13}C-acetate added to the medium. The incorporation of acetate to the terminal methyl was much lower in T24R cells, indicating that exogenous acetate is not a major source for their increased fatty acid de novo synthesis (Fig. 3C). The lower production of glucose-derived fatty acids in T24S cells is also consistent with the higher excretion of lactate from glucose (See Supplementary Fig. S1). In comparison, the higher consumption of glucose in T24R cells may
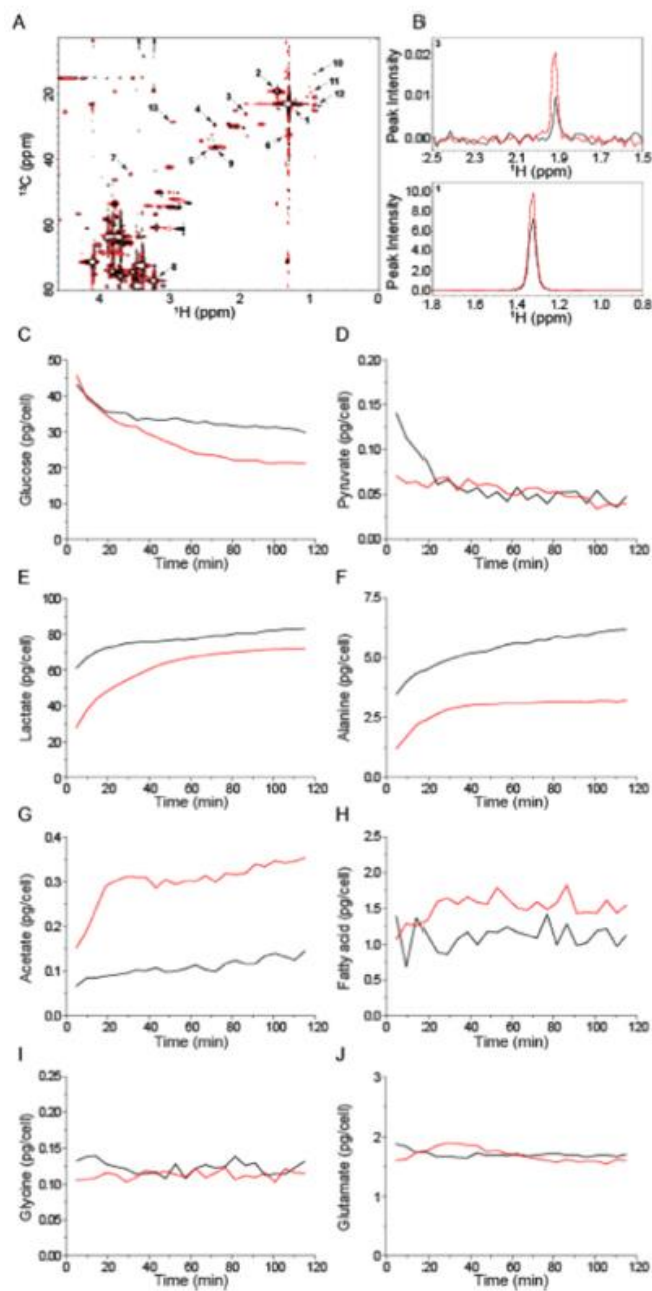
121

Fig. 1. Live NMR metabolomic comparison between cisplatin-sensitive and resistant cells.
(A) The first (black) and last (red) spectra obtained from cisplatin-sensitive (T24S) cancer cells over 1 h and 56 min after the addition of $^{13}C_6$-glucose. (1: lactate, 2: alanine, 3: acetate, 4: pyruvate, 5: succinate, 6: fatty acid, 7: glycine, 8: glucose, 9: glutamate, 10: isoleucine, 11: valine, 12: leucine, 13: glutathione (reduced); see supplementary Table S1). Assignments were obtained by spiking the standard compounds. (B) One-dimensional spectra from two compounds were extracted for comparison (1 and 3). (C through J) Time-dependent metabolic changes between T24S (black) and T24R (red) cells were obtained in real-time with live NMR metabolomics approach. The metabolites were quantified as described previously [24].
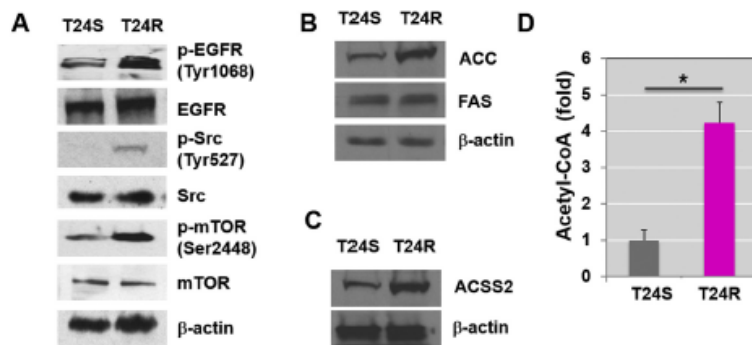
122

Fig. 2. Expression levels of metabolic regulators and enzymes in T24S and T24R cells.
Western blot analysis of (A) upstream regulators of metabolism (EGFR, Src, and mTOR) and their phosphorylated forms, (B) acetyl-CoA carboxylase (ACC) and fatty acid synthase (FAS) involved in fatty acid synthesis, and (C) acetyl-CoA synthetase 2 (ACSS2) for acetate utilization in T24S and T24R cells. The expression levels of β-actin were used as a loading control for western blot analysis. (D) The acetyl-CoA level was measured as described in the method section. The statistical analysis was performed using Student's t-test, and the asterisk indicates $P < 0.05$. The error bars represent the standard deviation ($N = 5$).

contribute to the higher de novo fatty acid synthesis through acetate production.

3.5. ACSS2 Inhibition decreases fatty acid synthesis and cell viability for T24R cells

As the data above collectively suggest a possible link from glucose to fatty acid synthesis through endogenous acetate from glucose, we decided to obtain further details on the pathways. Theoretically, a glucose-derived two carbon unit can be incorporated into fatty acids either via acetate or citrate, with the former mediated by ACSS2 and the latter by ACLY (Fig. 4A). The ACLY-mediated pathway has been considered the major pathway in various cancers [28], whereas the ACSS2-mediated pathway using glucose-derived endogenous acetate has been very little explored. Therefore, we selectively inhibited either of the two pathways using specific inhibitors, and measured the de novo fatty acid synthesis with NMR as above.

Inhibition of the ACSS2 pathway by 1-(2,3-di(thiophen-2-yl)quinoxalin-6-yl)-3-(2-methoxyethyl)urea decreased the de novo synthesis of fatty acid by > 60% in T24R cells, whereas no significant changes were observed in T24S cells (Fig. 4B). In comparison, ACLY inhibition by BMS-303141 led to a decrease in the de novo synthesis in T24S cells without significant effects on T24R cells. Importantly, the same ACSS2 inhibitor led to the growth inhibition of the T24R cells under cisplatin resistance condition (Fig. 4C). As we did not add any acetate in the media, these results confirm that the incorporation of glucose-derived endogenous acetate into fatty acids via ACSS2 is important in the cisplatin-resistance phenotype of T24R. We further obtained consistent data with siRNA approach. ACSS2 siRNA treatment induced a substantial decrease in acetyl-CoA in T24R cells, whereas ACLY siRNA treatment did not change the level (Supplementary Fig. S2A). The data also show that ACSS1 has much smaller role in acetyl-CoA production in T24R cells. Furthermore, ACLY siRNA induced a larger decrease in fatty acid synthesis in T24S than T24R cells (Supplementary Fig. S2B).

3.6. ACSS2 expression is increased in cisplatin-resistant patient tissue

To obtain the relevance of the above results in clinical settings, we tested the implication of ACSS2 with patient tissues. We measured the expression of ACSS2 in bladder tumor tissues obtained from patients who underwent a series of cisplatin-based chemotherapies. Bladder tumor tissues obtained from BC patients with complete remission (CR)

upon chemotherapies exhibited low levels of ACSS2, while those from patients with progressive disease (PD) had much higher levels of ACSS2 expression (Fig. 5A and B). Representative IHC images are also shown in Fig. 5C. These results confirm the relevance of ACSS2 in the cisplatin resistance of bladder cancer. As cisplatin-resistant bladder cancers are often more aggressive, we also performed an immunohistochemistry (IHC) analysis using bladder cancer tissue microarrays (TMA) with varying aggressiveness. The results showed that ACSS2 protein expression level is significantly associated with the aggressiveness of bladder cancers (Supplementary Fig. S3).

4. Discussion

By employing a live metabolomics and biochemical approach, we show that glucose-derived endogenous acetate contributes to fatty acid synthesis in cisplatin-resistant cells. Fatty acids are required components in proliferating cells, just like DNA, and therefore, it may not be surprising that cisplatin-resistant cells can have an alternative machinery to make fatty acids in the presence of the toxic drug. Still, the use of endogenous acetate in fatty acid synthesis may require more explanation. The most well-established pathway for fatty acid synthesis utilizes citrate as an intermediate for acetyl-CoA, whether it is from glucose or glutamine [29]. Citrate formed in mitochondria is lysed in the cytosol by ACLY to give oxaloacetate and acetyl-CoA that can be used for fatty acid synthesis. Another pathway for fatty acid synthesis involves exogenous acetate and requires ACSS2 for generating acetyl-CoA in the cytosol [16]. Although the involvement of ACSS2 is the same for both exogenous and endogenous acetate usage for fatty acid synthesis, we showed that ^{13}C incorporation into fatty acids from exogenous ^{13}C-acetate is much lower in cisplatin-resistant cells. Therefore, endogenous acetate seems to be the preferred source of the two carbon unit needed for fatty acid synthesis for the cisplatin-resistant cancer cells. Actually, the formation of endogenous acetate in cancers is not unprecedented. It was first documented about 80 years ago [30], but its roles in cancer metabolism has been little considered. For general fatty acid synthesis, too, endogenous acetate was proposed as an intermediate about 50 years ago [31], but it has been largely neglected compared to citrate as the main intermediate [14, 29]. Now, our data suggest a novel implication of endogenous acetate from glucose in the fatty acid synthesis in cisplatin-resistant cells. With currently available state-of-the-art analytical techniques, more roles of endogenous acetate in cancer metabolism are expected to be revealed.
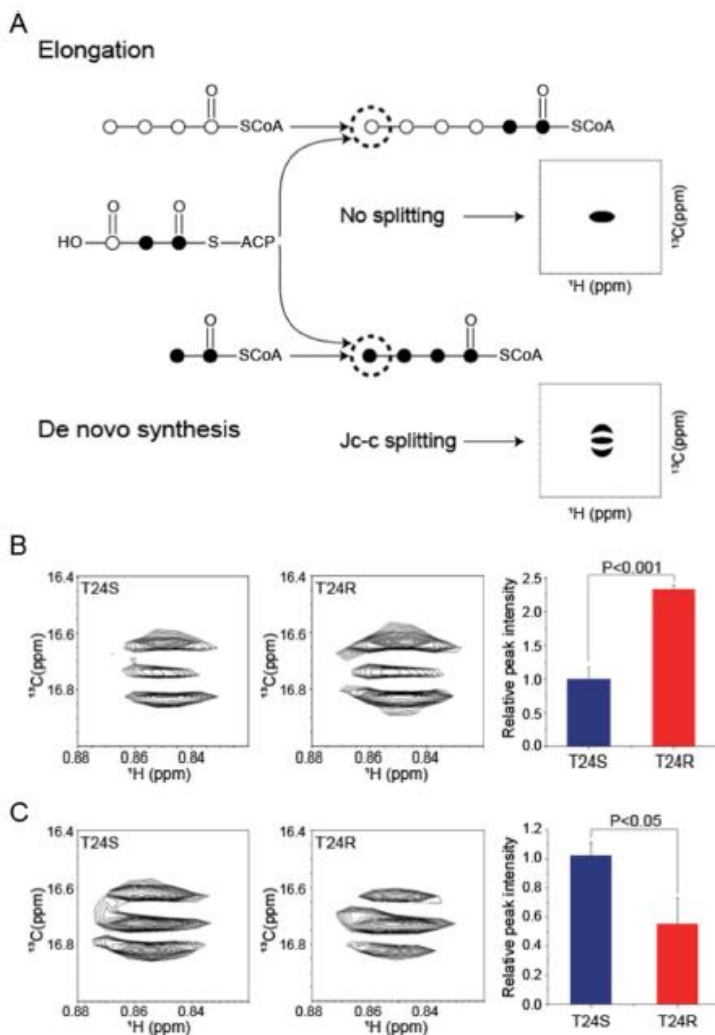
Fig. 3. Fatty acid de novo synthesis from glucose and acetate.
(A) Schematic representation of NMR signal splitting patterns by ^{13}C-acetyl-CoA for fatty acid elongation and de novo synthesis steps. Filled circles represent ^{13}C isotopes whereas open circles represent unlabeled carbons. (B) ^{13}C isotope incorporations in the omega position of the fatty acid alkyl chain with U-^{13}C-glucose. Left and Middle, NUS HSQC spectra for the omega carbon in fatty acid alkyl chains from T24S and T24R cells, respectively. Right, The peak area of the doublet of the omega carbon from the spectra. The peak area was normalized by the number of harvested cells. (C) ^{13}C isotope incorporations as in (B) with U-^{13}C-acetate. T24S and T24R cells were cultured in the media containing 5 mM non-labeled glucose supplemented with 20 mM ^{13}C-glucose (B) or 0.5 mM ^{13}C-acetate (C) for 24 h. The statistical analysis from three independent experiments was performed using the Student's t-test and the resulting P-values are indicated. The error bars represent the standard deviation.

Our data suggest that the endogenous acetate is derived from glucose, most probably through pyruvate, and we showed that acetate can be generated from pyruvate in mitochondria [32]. We also observed decrease in acetate production when T24R cells are treated with UK5099, an inhibitor of mitochondrial pyruvate carrier (MPC) (Supplementary Fig. S4). The pyruvate uptake through MPC is lower in some cancer cells, but still many cancers import pyruvate into mitochondria. For example, glioblastoma generates about half of cellular glutamate from glucose-driven TCA cycle that goes through pyruvate [15]. In osteosarcoma cells, glucose-derived citrate through pyruvate accounted for ~60% of total citrate pool [33]. Simultaneous enhancement of Warburg effect and TCA cycle using glucose-derived pyruvate was also observed in small cell lung cancer [34]. Therefore, despite pronounced Warburg effect that can reduce pyruvate uptake into cancer mitochondria and reduced MPC functions in some cancer cells, pyruvate can still contribute to acetate generation in mitochondria. The higher oxygen consumption rate for T24R cells also supports functional mitochondrial activity in T24R cells. (Supplementary Fig. S5).

An interesting question may be raised as to how the increased fatty acid synthesis affects the cisplatin chemosensitivity. There have been several reports linking fatty acid synthesis and anticancer drug
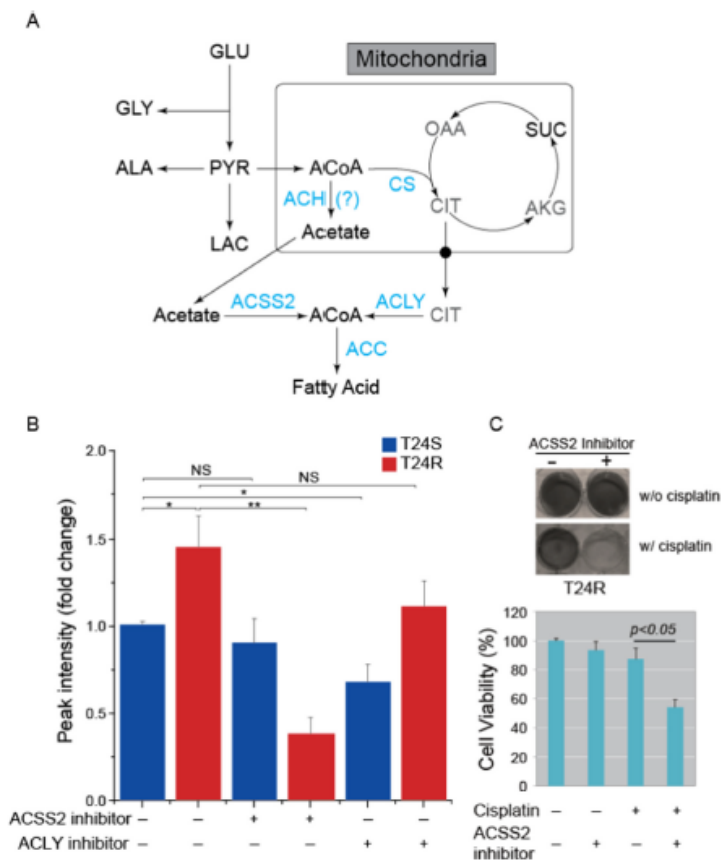
A

B

C

Fig. 4. The involvement of ACSS2 in the fatty acid de novo synthesis and survival in T24R cells.
(A) Schematic pathways for fatty acid synthesis from glucose. Pathways involving ACSS2 or ACLY are described. The question mark on the side of ACH indicates that the exact mechanism of acetate generation from pyruvate in mitochondria is yet to be firmly established (Additional references in Supplemental Information). (B) The effects of ACSS2 and ACLY inhibitors on the de novo fatty acid synthesis in T24S (blue) and T24R (red) cells. The de novo synthesis was estimated as in Fig. 3 and normalized against that of T24S without inhibitors. For inhibitors, either ACSS2 (15.6 μM) or ACLY (32 μM) inhibitors were added to the culture media. See the method section for the chemical names of the inhibitors. The statistical analysis was performed using Student's t-test. Two asterisks, $P < 0.001$; one asterisk, $P < 0.05$; NS, not significant, $P > 0.05$. The error bars represent the standard deviation. (C) The effect of the ACSS2 inhibitor on the cell survival of T24R cells in the presence of cisplatin. Upper: The T24R cells were seeded in a 6-well plate 1 day before experiment and cells were treated with ACSS2 inhibitor or vehicle 1 h before the addition of cisplatin (10 μM). Cells were stained with crystal violet solution 48 h after the cisplatin treatment. Lower: Bar graph for the cell viability obtained from photometric analysis of the upper samples. Abbreviation: GLU, glucose; GLY, glycine; ALA, alanine; PYR, pyruvate; LAC, lactate; ACoA, acetyl-CoA; OAA, oxaloacetate; SUC, succinate; AKG, a-ketoglutarate; CIT, citrate; ACH, acetyl-CoA hydrolase; CS, citrate synthase; ACSS2, acetyl-CoA synthetase 2; ACLY, ATP citrate lyase; ACC, acetyl-CoA carboxylase.

resistance. First, de novo fatty acid synthesis may lead to plasma membrane remodeling by changing fatty acid and lipid composition. This can lead to altered drug uptake and intracellular drug concentration, affecting the chemosensitivity [35, 36]. Second, it has been reported that increased de novo fatty acid synthesis lowers the portions of unsaturated fatty acids in plasma membrane [36]. Lowered levels of unsaturated fatty acids have been implicated in reduced efficacy of anti-cancer drugs, as unsaturated fatty acids are important sources of reactive oxygen free radicals [36]. In addition, the production of reactive oxygen species (ROS) is an important mechanism for the cytotoxicity of many anticancer drugs, including cisplatin. Third, increased fatty acid synthesis by FASN overexpression may protect cancer cells from apoptosis. The increased FASN reducing the expression of biosynthesis of pre-apoptotic lipid molecules has been suggested as a new mechanism of chemoresistance [37]. As the above mechanisms are not mutually exclusive, the increased cisplatin resistance upon elevated fatty acid synthesis from glucose-derived acetate may involve all the above or a yet-to-be identified pathways.

By implicating ACSS2 in chemosensitivity in cells and patient tissues, our results suggest two key translational opportunities involving the protein. For one thing, as elevated levels of ACSS2 were observed in cisplatin-resistant patient tissues, which are often more invasive and refractory, the ACSS2 level may be used to stratify patients who would require more aggressive treatment from the beginning. In addition, the ACSS2 level may be helpful in deciding whether or not cisplatin should be administered to particular patients. For the other, inhibitors of ACSS2, along with other treatment modalities, may be used to treat cisplatin-resistant bladder cancer patients. Although the inhibitor used in the current study may not be suitable in the clinical settings, given the importance of ACSS2 in the tumorigenesis of glioblastoma and hepatocellular carcinoma [15, 16], more inhibitors are expected. In addition, other enzymes on the fatty acid synthetic pathway involving endogenous acetate, i.e., acetyl-CoA thioesterase needed for acetate transport across the mitochondrial membrane, may be novel targets for cisplatin-resistant bladder cancer.

Disclosure of potential conflicts of interest

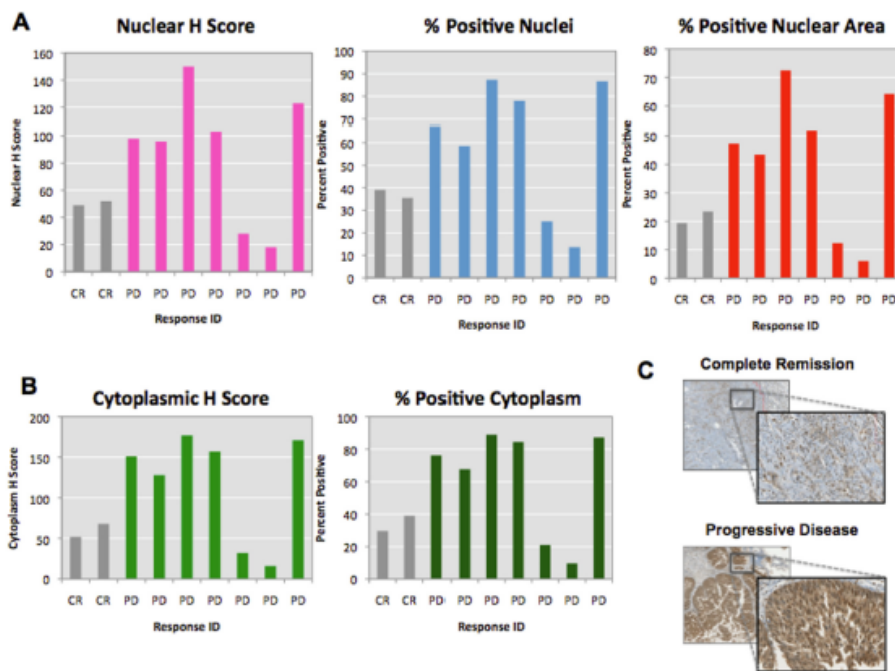The authors declare no potential conflicts of interest.

Fig. 5. The expression levels of ACSS2 in the tissues from cisplatin-sensitive and resistant BC patients.
(A) Quantitative analysis of annotated regions of the nucleus from IHC results: the nuclear H-score, percent of positive nuclei, and percent of positive nuclear area in BC tumors are presented. (B) Quantitative analysis of annotated regions of the cytoplasm from IHC results: the cytoplasmic H-score and percent of positive cytoplasm are presented. (C) Representative digitalized immunohistochemistry images. Complete remission (CR; cisplatin-sensitive) or progressive disease (PD; cisplatin-resistant) groups. An anti-ACSS2 antibody was used for IHC staining.

Author contributions

J.K. and SP designed the study. H.W. and S.L. performed metabolomics study and analyzed the data. W.Z and J.K. performed Western blot and Acetyl-CoA measurement experiments. O.J.L. and S.J.Y. provided patient data and sample, and they performed H&E analysis. J.K., H. W., S.L. and S.P. wrote the manuscript. All authors read and approved the final manuscript.

Transparency document

The Transparency document associated with this article can be found, in online version.

Acknowledgments

Appendix A. Supplementary data

Supplementary data to this article can be found online at https://doi.org/10.1016/j.bbalip.2018.06.005.

References

[1] L.A. Kiemeney, J.A. Witjes, A.L. Verbeek, R.P. Heijbroek, F.M. Debruyne, The clinical epidemiology of superficial bladder cancer. Dutch South-East Cooperative Urological Group, Br. J. Cancer 67 (1993) 806–812.
[2] L.S. Borden Jr., P.E. Clark, M.C. Hall, Bladder cancer, Curr. Opin. Oncol. 15 (2003)

227–233.

[3] M.C. Hall, S.S. Chang, G. Dalbagni, R.S. Pruthi, J.D. Seigne, E.C. Skinner, J.S. Wolf Jr., P.F. Schellhammer, Guideline for the management of nonmuscle invasive bladder cancer (stages Ta, T1, and Tis): 2007 update, J. Urol. 178 (2007) 2314–2330.

[4] M. Babjuk, W. Oosterlinck, R. Sylvester, E. Kaasinen, A. Bohle, J. Palou-Redorta, U. European association of, EAU guidelines on non-muscle-invasive urothelial carcinoma of the bladder, Eur. Urol. 54 (2008) 303–314.

[5] A. Stenzl, N.C. Cowan, M. De Santis, M.A. Kuczyk, A.S. Merseburger, M.J. Ribal, A. Sherif, J.A. Witjes, Treatment of muscle-invasive and metastatic bladder cancer: update of the EAU guidelines, Eur. Urol. 59 (2011) 1009–1018.

[6] P.C. Black, C.P. Dinney, Growth factors and receptors as prognostic markers in urothelial carcinoma, Curr. Urol. Rep. 9 (2008) 55–61.

[7] S.M. Cohen, S.J. Lippard, Cisplatin: from DNA damage to cancer chemotherapy, Prog. Nucleic Acid Res. Mol. Biol. 67 (2001) 93–130.

[8] N.A.G. Santos, C.S. Catao, N.M. Martins, C. Curti, M.L.P. Bianchi, A.C. Santos, Cisplatin-induced nephrotoxicity is associated with oxidative stress, redox state unbalance, impairment of energetic metabolism and apoptosis in rat kidney mitochondria, Arch. Toxicol. 81 (2007) 495–504.

[9] Z.H. Siddik, Cisplatin: mode of cytotoxic action and molecular basis of resistance, Oncogene 22 (2003) 7265–7279.

[10] A. Viale, G.F. Draetta, Metabolic features of cancer treatment resistance, Recent Results Cancer Res. 207 (2016) 135–156.

[11] H.N. Kwon, M. Kim, H. Wen, S. Kang, H.J. Yang, M.J. Choi, H.S. Lee, D. Choi, I.S. Park, Y.J. Suh, S.S. Hong, S. Park, Predicting idiopathic toxicity of cisplatin by a pharmacometabonomic approach, Kidney Int. 79 (2011) 529–537.

[12] X. Pan, M. Wilson, L. Mirbahai, C. McConville, T.N. Arvanitis, J.L. Griffin, R.A. Kauppinen, A.C. Peet, In vitro metabonomic study detects increases in UDP-GlcNAc and UDP-GalNAc, as early phase markers of cisplatin treatment response in brain tumor cells, J. Proteome Res. 10 (2011) 3493–3500.

[13] L.B. Sullivan, D.Y. Gui, M.G.V. Heiden, Altered metabolite levels in cancer: implications for tumour biology and cancer therapy, Nat. Rev. Cancer 16 (2016) 680–693.

[14] Z.T. Schug, J. Vande Voorde, E. Gottlieb, The metabolic fate of acetate in cancer, Nat. Rev. Cancer 16 (2016) 708–717.

[15] T. Mashimo, K. Pichumani, V. Vemireddy, K.J. Hatanpaa, D.K. Singh, S. Sirasanagandla, S. Nannepaga, S.G. Piccirillo, Z. Kovacs, C. Foong, Z. Huang, S. Barnett, B.E. Mickey, R.J. DeBerardinis, E.A. Maher, R.M. Bachoo, Acetate is a bioenergetic substrate for human glioblastoma and brain metastases, Cell 159 (2014) 1603–1614.

[16] S.A. Comerford, Z. Huang, X. Du, Y. Wang, L. Cai, A.K. Witkiewicz, H. Walters, M.N. Tantawy, A. Fu, H.C. Manning, J.D. Horton, R.E. Hammer, S.L. McKnight, R.P. Tu, Acetate dependence of tumors, Cell 159 (2014) 1591–1602.

[17] Y. Yoshii, T. Furukawa, T. Saga, Y. Fujibayashi, Acetate/acetyl-CoA metabolism associated with cancer fatty acid synthesis: overview and application, Cancer Lett. 356 ((2015) 211–216.

[18] X. Jin, S.J. Yun, P. Jeong, I.Y. Kim, W.J. Kim, S. Park, Diagnosis of bladder cancer and prediction of survival by urinary metabolomics, Oncotarget 5 (2014) 1635–1645.

[19] L. Lin, Z. Huang, Y. Gao, Y. Chen, W. Hang, J. Xing, X. Yan, LC-MS-based serum metabolic profiling for genitourinary cancer classification and cancer type-specific biomarker discovery, Proteomics 12 (2012) 2238–2246.

[20] N. Putluri, A. Shojaie, V.T. Vasu, S.K. Vareed, S. Nalluri, V. Putluri, G.S. Thangjam, K. Panzitt, C.T. Tallman, C. Butler, T.R. Sana, S.M. Fischer, G. Sica, D.J. Brat, H. Shi, G.S. Palapattu, Y. Lotan, A.Z. Weizer, M.K. Terris, S.F. Shariat, G. Michailidis, A. Sreekumar, Metabolomic profiling reveals potential markers and bioprocesses altered in bladder cancer progression, Cancer Res. 71 (2011) 7376–7386.

[21] Z. Huang, L. Lin, Y. Gao, Y. Chen, X. Yan, J. Xing, W. Hang, Bladder cancer determination via two urinary metabolites: a biomarker pattern approach, Mol. Cell. Proteomics 10 (2011) (M1 11 007 922).

[22] W.T. Kim, J. Kim, C. Yan, P. Jeong, S.Y. Choi, O.J. Lee, Y.B. Chae, S.J. Yun, S.C. Lee, W.J. Kim, S100A9 and EGFR gene signatures predict disease progression in muscle invasive bladder cancer patients after chemotherapy, Ann. Oncol. 25 (2014) 974–979.

[23] M.Y. Lee, A. Yeon, M. Shahid, E. Cho, V. Sairam, R. Figlin, K.H. Kim, J. Kim, Reprogrammed lipid metabolism in bladder cancer with cisplatin resistance, Oncotarget 9 (2018) 13231–13243.

[24] H. Wen, W.J. Xu, X. Jin, S. Oh, C.H. Phan, J. Song, S.K. Lee, S. Park, The roles of IP3 receptor in energy metabolic pathways and reactive oxygen species homeostasis revealed by metabolomic and biochemical studies, Biochim. Biophys. Acta 1853 (2015) 2937–2944.

[25] H. Wen, Y.J. An, W.J. Xu, K.W. Kang, S. Park, Real-time monitoring of cancer cell metabolism and effects of an anticancer agent using 2D in-cell NMR spectroscopy, Angew. Chem. Int. Ed. Eng. 54 (2015) 5374–5377.

[26] S. Lee, H. Wen, Y.J. An, J.W. Cha, Y.J. Ko, S.G. Hyberts, S. Park, Carbon isotopomer analysis with non-uniform sampling HSQC NMR for cell extract and live cell metabolomics studies, Anal. Chem. 89 (2017) 1078–1085.

[27] N.D. Amoedo, E. Obre, R. Rossignol, Drug discovery strategies in the field of tumor energy metabolism: limitations by metabolic flexibility and metabolic resistance to chemotherapy, Biochim. Biophys. Acta 1858 (2017) 674–685.

[28] N. Zaidi, J.V. Swinnen, K. Smans, ATP-citrate lyase: a key player in cancer metabolism, Cancer Res. 72 (2012) 3709–3714.

[29] F. Rohrig, A. Schulze, The multifaceted roles of fatty acid synthesis in cancer, Nat. Rev. Cancer 16 (2016) 732–749.

[30] K.A. Elliott, M.E. Greig, The metabolism of lactic and pyruvic acids in normal and tumour tissues: the formation of succinate, Biochem. J. 31 (1937) 1021–1032.

[31] M.S. Kornacker, J.M. Lowenstein, Citrate and the conversion of carbohydrate into fat. The activities of citrate-cleavage enzyme and acetate thiokinase in livers of starved and re-fed rats, Biochem. J. 94 (1965) 209–215.

[32] W.J. Xu, H. Wen, H.S. Kim, Y.J. Ko, S.M. Dong, I.S. Park, J.I. Yook, S. Park, Observation of acetyl phosphate formation in mammalian mitochondria using real-time in-organelle NMR metabolomics, Proc. Natl. Acad. Sci. U. S. A. 115 (2018) 4152–4157.

[33] A.R. Mullen, W.W. Wheaton, E.S. Jin, P.H. Chen, L.B. Sullivan, T. Cheng, Y. Yang, W.M. Linehan, N.S. Chandel, R.J. DeBerardinis, Reductive carboxylation supports growth in tumour cells with defective mitochondria, Nature 481 (2012) 385–388.

[34] M. Morita, T. Sato, M. Nomura, Y. Sakamoto, Y. Inoue, R. Tanaka, S. Ito, K. Kurosawa, K. Yamaguchi, Y. Sugiura, H. Takizaki, Y. Yamashita, R. Katakura, I. Sato, M. Kawai, Y. Okada, H. Watanabe, G. Kondoh, S. Matsumoto, A. Kishimoto, M. Obata, M. Matsumoto, T. Fukuhara, H. Motohashi, M. Suematsu, M. Komatsu, K.I. Nakayama, T. Watanabe, T. Soga, H. Shima, M. Maemondo, N. Tanuma, PKM1 confers metabolic advantages and promotes cell-autonomous tumor cell growth, Cancer Cell 33 (2018) 355–367 (e357).

[35] C. Peetla, S. Vijayaraghavalu, V. Labhasetwar, Biophysics of cell membrane lipids in cancer drug resistance: implications for drug transport and drug delivery with nanoparticles, Adv. Drug Deliv. Rev. 65 (2013) 1686–1698.

[36] E. Rysman, K. Brusselmans, K. Scheys, L. Timmermans, R. Derua, S. Munck, P.P. Van Veldhoven, D. Waltregny, V.W. Daniels, J. Machiels, F. Vanderhoydonc, K. Smans, E. Waelkens, G. Verhoeven, J.V. Swinnen, De novo lipogenesis protects cancer cells from free radicals and chemotherapeutics by promoting membrane lipid saturation, Cancer Res. 70 (2010) 8117–8126.

[37] H. Liu, Y. Liu, J.T. Zhang, A new mechanism of drug resistance in breast cancer cells: fatty acid synthase overexpression-mediated palmitate overproduction, Mol. Cancer Ther. 7 (2008) 263–270.

127

The effects of Mozart's music on metabolic response upon stress

Sujin Lee[1], Ga Eul Yoo[2], Hyun Ju Chong[2], Seung Hong Choi[3], and Sunghyouk Park[1,*]

[1]Natural Product Research Institute, College of Pharmacy, Seoul National University, Sillim-dong, Gwanak-gu, Seoul, 151-742, Republic of Korea
[2]Department of Music Therapy, Graduate School, Ewha Womans University, Seoul, Republic of Korea
[3]Department of Radiology, Seoul National University College of Medicine, 28, Yongon-dong, Chongno-gu, 110-744, Seoul, Republic of Korea

Abstract Mozart's music has been suggested to affect spatio-temporal reasoning of listeners, which has been called "Mozart effect". However, the effects of Mozart's music on human metabolism have not been known. We dissected Mozart's music into its compositional elements and studied their effects on metabolism of experimental animals. Mozart music significantly reduced cortisol level induced by stress. NMR metabolomic study revealed different urine metabolic profile according to the listening to Mozart's music. In addition, each element of music exhibited different metabolic profile. Functional MRI study also showed enhanced brain activity upon listening to Mozart's music. Taken together, Mozart's music seems to be related with brain activity, stress hormone and whole body metabolism.

Keywords Mozart effect, NMR, stress, music

서문

음악이 신체에 미치는 영향은 다양한 차원에서 일어난다. 이는 크게 생리적, 운동적, 정서적, 그리고 인지적 반응으로 구분되지만 총체적으로 상호 유기적 영향을 미친다고 할 수 있다.[1-3] 소리의 복합체로 구성된 음악은 청각적 처리과정을 통해 감상자의 생리적 항상성을 도

모할 수도 있고 방해할 수도 있다. 동조화 (entrainment)은 외부에서 들어오는 청각적 자극 (auditory cue)에 동조화되려는 내적 성향을 말하는데 음악 감상 동안 음악이 체내 생리적 상태의 각성 또는 이완을 유도하는 것도 이 때문이라고 할 수 있다.[4,5]

이러한 반응을 유도하는 음악 작품의 하나로서 모차르트 음악은 그 효과에 대해 많은 연구가 수행되어 왔다. 1993 년 모차르트 음악 (소나타 K.488)이 spatio-temporal reasoning (공간지각능력)을 증진시킨다는 연구결과가 발표되며 음악 청취와 인지 능력 사이의 연관성을 밝히려는 연구들이 진행되었다.[6] 공간적 추론에 대한 단기적 개선을 의미하는 'Mozart effect'는 많은 과학자들이 그 유효성을 검증하였으나 방법론적 차이로 인해 효과에 대한 논란이 있어 왔다. 최근에는 모차르트 음악에 대한 fMRI 연구에서 spatio-temporal reasoning 과 관련된 brain 영역에서 혈류 활성화가 나타난다는 결과가 보고되었다.[7] 치료학적 효과에서도 다양한 연구가 진행되어 심혈관계 질환, 신경계 질환 등의 질병에 적용 가능성이 보고되고 있다. 모차르트 음악이 blood pressure 와 heart rate 을 감소시킨다는 연구결과는 심혈관계 질환의 치료 보조 목적으로 이용될 수 있다.[8] 신경계 질환 분야에서는 모차르트 음악이 epileptic disease 와 ADHD 등의 증상을 완화시킬 수 있다는 결과가 보고되었다.[9, 10] 또한 모차르트 음악이 스트레스를 경감시키는 효과가 있다는 연구결과도

* Address correspondence to: Sunghyouk Park, College of Pharmacy, Seoul National University, San 56-1 Sillim-dong, Gwanak-gu, Seoul 151742, Republic of Korea, Tel: +82-2-880-7831; E-mail: psh@snu.ac.kr

보고되었다.[11]

음악에 의해 조절될 수 있는 스트레스는 신체에 다양한 영향을 미쳐 각종 질병에의 이환을 증가시킨다. 스트레스는 자율신경계, 호르몬계를 교란시키고 염증을 유발하며 물질대사를 변화시킨다고 알려져 있다. 스트레스가 신체에 미치는 영향을 연구하기 위해 스트레스 호르몬과 대사반응에 대한 다양한 연구가 진행되고 있다. 최근 우울증 환자의 urine 에서 cortisol 과 그의 대사 형태인 tetrahydrocortisol 농도 증가 및 스트레스 관련 호르몬 비율의 변화가 보고되었다. 또한 만성 스트레스에 노출된 rat 의 대사연구에서 plasma 와 urine 의 대사 변화가 확인되었다. Rat 의 만성 스트레스 모델에서 혈압 증가 및 우울증 발생과 관련된 대사체들도 확인되었다. 이렇게 스트레스에 대한 다양한 연구가 진행중이지만 스트레스에 의한 대사반응을 이해하기에는 아직 부족하다. 더욱이 스트레스에 영향을 준다고 알려진 모차르트 음악이 대사에 어떤 영향이 주는지는 아직까지 연구된 바가 없다. 즉 모차르트 음악과 스트레스와의 상관성 연구가 있고 스트레스와 대사반응과의 상관성 연구도 있으나 모차르트 음악이 대사에도 영향을 미치는지는 아직 알려지지 않았다. 따라서 우리는 모차르트 음악이 유도된 스트레스에 의한 대사반응을 경감시킬 수 있는지에 대해 대사적 관점에서 연구를 진행하였다. 우리는 좀더 세분화된 분석을 진행하기 위해 모차르트 음악을 리듬, 선율, 리듬+선율, 그리고 원곡으로 분류하여 재구성하였다. 이러한 모차르트 음악에 의한 대사변화 연구를 통해 음악 및 세분화된 음악 요소에 따른 심리적 반응 변화에 대한 과학적 근거 및 치료 기틀을 마련하고 스트레스에 의한 대사반응을 이해함으로써 이를 스트레스 관련 질환에 적용할 수 있을 것이다.

실험방법

모차르트 음악의 특성 분석 및 음원 추출 – 문헌조사를 통해 모차르트 음원으로 피아노 소나타 K.448 를 선정하였다. 모차르트 음악의 각 요소별 효과를 측정하기 위해 모차르트 음악을 리듬, 선율, 선율+리듬, 원곡으로 구분하여 재구성하는 작업 진행하였다. 무음군과 리듬, 선율, 선율+리듬, 원곡의 4 가지 음원군으로 해서 총 5군으로 연구 진행하였다.

Rat 의 가청영역은 사람의 가청영역과 달라 음원을 귀의 가청영역으로 음역대를 높여서 녹음 진행하였다. 왼손 반주를 포함한 음악 전체를 1kHz 이상이 되도록 재녹음 진행하였다. 음원 녹음 후 noise reduction 과 음질보정 작업을 진행하였다.

모차르트 음악을 청취한 실험동물의 urine 채취 – SD rat (6 주령, male)을 구입하여 일주일 동안 적응시켰다. Rat holder 를 이용해 rat 에 1 시간 동안 구속 스트레스를 준 후 무음/리듬/선율/리듬+선율/원곡의 음원 중 하나를 선택하여 들려주었다. Rat 의 일주기 리듬에 맞추어 소등 및 기상 시간인 오후 7 시부터 아침 7 시까지 12 시간 동안 음원을 들려주며 metabolic cage 를 이용하여 urine 을 채취하였다.

LC-MS 를 이용한 스트레스 호르몬 측정 – Rat urine 의 cortisol level 을 측정하기 위해 600 µl urine 을 SPE column (Oasis HLB)을 사용하여 solid phage extraction 을 진행하였다. column 에 3 ml MeOH 을 넣고 감압하고 3 ml DW 를 넣고 감압하였다. 500 µl urine 을 SPE column 으로 옮겼다. 3 ml DW, 3 ml acetone/DW (20:80), 1 ml hexane 을 차례로 넣고 감압하였다. 2 ml MeOH 로 추출하여 vacuum drying 하였다. 최종 100 µl MeOH/DW (1:1, 0.1% formic acid)에 녹였다. LC-MS (Agilent Triple Quad)를 사용하여 측정하였다. A buffer 로 0.1 formic acid DW, B buffer 로 0.1% formic acid MeOH 를 사용하여 C18 column 으로 분리를 진행하였다. Cortisol solution (Sigma-Aldrich, C-106)을 standard 로 사용하였다.

NMR 을 이용한 대사 분석 – Urine 을 얼음 위에서 녹인 후 30 sec 동안 vortexing 하였다. 4 °C 에서 10 min 동안 15,000 g 로 centrifuge 하였다. Urine 상층을 1 M K$_2$HPO$_4$, 400 mM NaH$_2$PO$_4$, 0.25% TSP를 포함하는 buffer 와 9:1 의 비율로 섞었다. 샘플을 5 mm NMR tube 로 옮긴 후 1D NOESY NMR data (Bruker, 800 MHz)를 얻었다. NMR 데이터를 Chenomx (NMR assignment S/W)로 분석하고 종합하여 전체

대사프로파일을 얻었다. NMR data 분석을 위해 statistical analysis 진행하였다.

fMRI 를 이용한 영상의학적 연구 – Anatomical images fMRI 측정 조건을 다음과 같이 최적화 하였다. Fast spin echo (axial and sagittal, TR/TE = 3000/9.61 ms; FOV = 40 × 40, matrix size = 256 × 256, 1 average, 7 slices (no gap), slice thickness = 1 mm). Resting state fMRI 측정 조건을 다음과 같이 최적화하였다. gradient echo EPI (axial, TR/TE = 1000/20 ms; FOV = 40 × 40, matrix size = 64 × 64, 1 average, 7 slices (no gap), slice thickness = 1 mm, 300 acquisitions).
무음군과 음원군에 대하여 treatment 전후에 fMRI data 를 얻었다. Brain 과 뇌의 인지와 기억을 매개하는 역할을 하는 retrosplenial cortex (RSC) 영역의 data 를 얻었다. 각 slice data 는 3D matrix (64 × 64 × 300) 형태로 저장. ROI 의 mean signal intensity 는 300 images 를 통해 평가하였다. fMRI data processing 및 seed-based brain connectivity analysis 을 진행하였다.

실험결과

모차르트 음악이 스트레스에 의해 유발된 대사 반응에 영향을 줄 수 있는지를 확인하기 위하여 다양한 모차르트 음악 중 기존에 spatio-temporal task 수행력 부분에서 많은 연구가 진행되었던 모차르트 피아노 소나타 K.488 을 선정하였다. 그리고 모차르트 음악에 대한 좀더 세분화된 분석을 진행하고자 음원을 음악의 요소에 따라 리듬, 선율, 리듬+선율, 원곡으로 분류하였다. 대사반응을 확인하기 위해 rat 에 1 시간 동안 구속 스트레스를 준 후 무음 또는 다양한 음원을 제공하면서 urine 을 채취하였다. 스트레스 마커로서 cortisol 을 LC-MS (Agilent Triple Quad)로 확인하였을 때 무음군에서는 cortisol level 이 높게 측정된 반면 원곡군 (*p* = 0.029) 과 선율+리듬군 (*p* = 0.032) 에서는 유의하게 낮게 측정되었다. (Result 1. A) 리듬군과 선율군에서도 cortisol level 이 무음군에 비해 낮게 측정되었으나 통계적 유의성은 없었다. (Result 1. A) 결과적으로 스트레스를 받은 후 모차르트 음악의 원곡 또는 원곡의 선율과 리듬이 포함된 음원을 들었을 때 유의하게

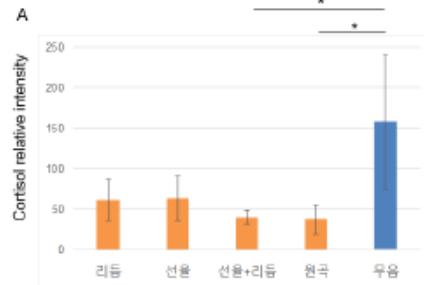cortisol level 이 감소하여 스트레스를 경감시키는 반응이 나타났음을 확인할 수 있었다.

Figure 1. 모차르트 음악 청취와 cortisol level. (A) Rat urine 의 cortisol level 은 LC-MS (Agilent Triple Quad)로 측정하였다. *는 0.05 이하의 *p* 값을 나타낸다.

모차르트 음악을 들었을 때 유의하게 cortisol level 이 감소한 것을 확인하였는데 cortisol 은 대표적인 대사 호르몬이기도 하므로 스트레스에 의해 유발된 대사반응에도 영향을 주는지를 확인하였다. 대사반응에 대한 영향은 NMR 을 이용한 소변 대사체학을 통하여 확인 하였다. Rat urine 의 1D NOESY NMR data 를 얻어 multivariate statistical analysis (OPLS-DA score plot)를 진행하였을 때 무음군과 음원군 전체는 통계적으로 유의하게 대사적 차이를 보인다는 것을 확인하였다. (Result 2. A, B) 무음군과 세부 음원군 각각의 대사적 프로파일을 비교하였을 때도 모든 음원군에서 각각 유의성 있게 무음군과 구분되는 것을 확인하였고 Q2 값도 모두 0.7 이상으로 높게 나타났다. (Result 2. C) 즉 어떤 음원군이라도 스트레스에 의해 유발된 대사반응을 변화시키는 작용을 한다는 것을 확인하였다.
모든 음원군은 음원의 종류에 상관없이 스트레스에 의한 대사반응을 변화시킨다는 것을 확인하였으므로 각각의 세부 음원은 대사적으로 어떤 차이를 나타내는지 확인하였다. 세부 음원에 대해 OPLS-DA 통계분석을 진행하였을 때 각각의 세부 음원군은 내부적으로 통일성 있는 대사 프로파일을 나타내면서도 세부 음원군별
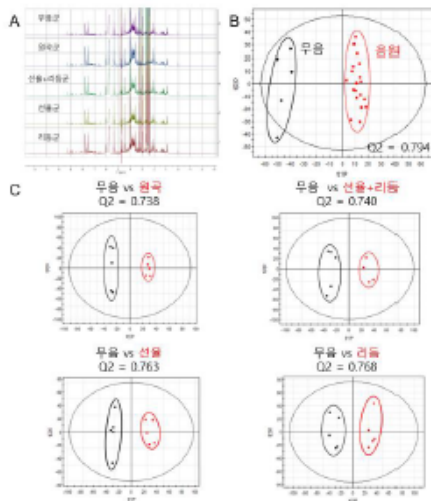
Figure 2. 모차르트 음악 청취와 대사 프로파일. (A) 1D NOESY NMR (Bruker, 800 MHz) raw data (B) 부음군과 음원군 전체에 대한 multivariate statistical analysis (OPLS-DA score plot) (C) 부음군과 각 음악 요소군의 OPLS-DA score plot

Figure 3. 모차르트 음악의 요소별 대사프로파일의 차이. (A) 부음군을 포함한 세부 음악 요소의 multivariate statistical analysis (PLS-DA score plot) (B) 세부 음악 요소만의 PLS-DA score plot (C) 원곡, 선율 그리고 리듬의 PLS-DA score plot (D) 두 개씩 묶은 세부 음악 요소의 OPLS-DA score plot

로도 구분되는 차이를 보이는 것을 확인할 수 있었다. (Result 3, A) 선율+리듬군은 선율군과 원곡군에 일부 겹치는 대사 프로파일을 나타내서 부분적으로 유사성이 있음을 확인하였다. (Result 3. B) 원곡, 선율, 리듬의 대사 프로파일은 정확히 삼등분되는 대사 프로파일을 보여 원곡(화음), 선율, 리듬에 의한 대사변화가 상당한 차이를 보이는 것을 확인하였다. (Result 3. C) 세부 음원군에 대해 2 그룹씩 분석하였을 때 선율 vs 리듬에서 가장 큰 차이 (Q2 = 0.848) 가 나타났다. (Result 3. D) 원곡 vs 선율 그리고 원곡 vs 리듬에서도 잘 구분되었으나 원곡 vs 선율+리듬에서는 통계적으로 유의한 차이가 없었다. (Restuls 3. D) 결과적으로 리듬, 선율, 그리고 원곡은 스트레스에 의한 대사반응에 각기 다른 작용을 하며 선율과 리듬을 합친 경우는 각 요소만 있을 때 보다 원곡과 가까워 지는 대사반응을 나타내는 것을 확인하였다.
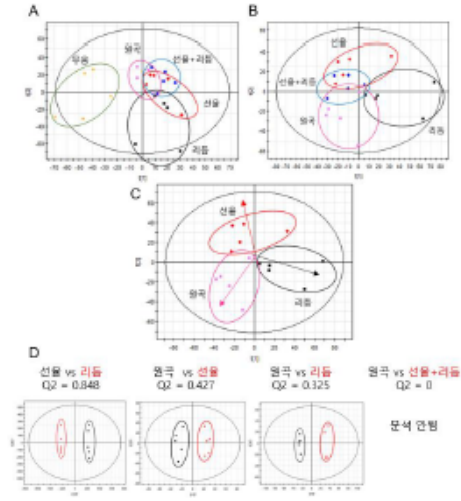
리듬, 선율, 그리고 원곡에 의한 대사변화가 특징적으로 다르게 나타나므로 리듬, 선율과 화음을 모두 포함하는 원곡을 들었을 때 대사적 영향이 극대화될 것으로 생각된다. 원곡을 들었던 rat urine 에서 cortisol level 이 가장 낮았던 것도 원곡에서 대사적 영향이 가장 크다는 것을 뒷받침해준다. 스트레스에 의한 대사반응을 가장 크게 경감시킨 원곡군에서 어떤 대사변화가 나타났는지 구체적으로 확인하기 위해 개별적 대사체 분석을 진행하였다. S-plot 을 통해 부음군과 원곡군에서 특징적인 대사체를 확인하였을 때 부음군에서 correlation coefficient 가 높은 대사체는 glycine, hippurate, succinate 등이 확인되었고 원곡군에서 correlation coefficient 가 높은 대사체는 taurine, alanine, thymidine, urea 등이 확인되었다. (Result 4. A, B)
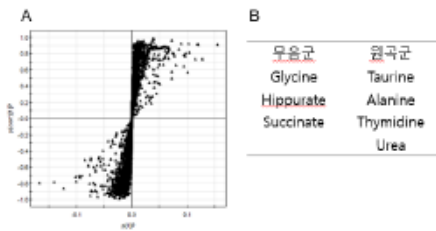
Figure 4. Urine 대사체 분석. (A) 무음군과 원곡군의 S-plot (B) 각 군과 상관관계가 높은 대사체 분석

이런 총체적 대사변화는 앞에서 관찰된 cortisol의 차이에 의해 야기될 수 있다고 생각되며 cortisol 은 간뇌의 시상하부에서 시작되는 HPA axis 에 의해 분비가 조절되므로 모차르트 음악이 결국 뇌에 영향을 미쳐 신체의 대사를 변화시켰다고 할 수 있다. 모차르트 음악이 뇌에 영향을 미쳤다면 뇌의 대사에는 어떤 영향을 미치는지 확인하기 위해 9.4 T 소동물용 자기공명강비 (functional MRI)를 이용하여 rat brain 의 뇌활성도 (DMN connectivity strength)를 측정하였다. (Result 5. A) 모차르트 음악을 들려주지 않은 무음군의 rat 에서는 pre-treatment 상태에서 나타난 뇌활성화도가 post-treatment 에서 현저히 감소하였다. ($p = 0.0045$) (Result 5. B) 그러나 모차르트 음악을 들려준 rat 에서는 pre-treatment 에서 뇌의 활성도가 무음군에 비해 넓고 강하게 나타났고 post-treatment 에서도 감소되지 않고 오히려 증가하였다. ($p = 0.0098$) (Result 5. B) 이로써 모차르트 음악이 rat brain 의 대사 활성을 증가시킨다는 것을 확인할 수 있었다.

고찰

모차르트 음악이 스트레스에 의해 유발된 대사반응에 어떤 영향을 미치는지를 확인하기 위해 대사체학적 연구를 진행하였다. 스트레스 마커로서 cortisol level 을 측정하였을 때 모차르트 음악의 원곡과 선율+리듬이 cortisol level 을 유의하게 감소시켰고 원곡이 가장 많이 감소시켰음을 확인하였다. 이는 모차르트 음악이 스트
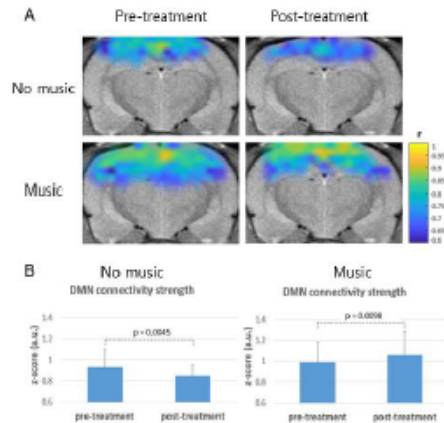

Figure 5. 모차르트 음악 청취와 rat brain 의 대사 변화 (A) 두 동물 모델의 pre- and post-treatment default mode networks (DMNs) (B) DMN connectivity strength 의 box plot. Connectivity map 은 Pearson's correlation coeffeicient 값이 0.6 이상인 region 에 대하여 color gradient 로 표시되었다.

레스를 조절하는 기관에 영향을 미쳐 직접적으로 스트레스를 감소시켰다는 것과 그 작용이 원곡에서 가장 크다는 것을 의미한다. 결국 모차르트 원곡에 의한 스트레스 완화 작용은 긍정과 진정 효과를 나타내는 정서적인 영향과 관련이 있음을 확인할 수 있었다.

모차르트 음악에 의한 스트레스 완화작용은 대사 프로파일을 통해서도 확인되었다. 모든 음원군의 대사 프로파일이 무음군의 대사 프로파일과 유의한 차이를 나타냈는데 이는 무음군에서 보이는 스트레스에 의한 대사반응이 완화되었다는 것을 의미한다. 또한 이는 좀더 깊은 의미에서 음악을 듣는다는 의식적 행위가 다양한 신체반응을 일으키고 결과적으로 물질대사 수준까지 영향을 미쳤다는 것을 나타낸다. 여기서 어떤 음원이라도 상관없이 대사변화를 일으켰다는 것은 음원의 청취가 대사변화와 밀접한 상관관계를 가진다는 것을 의미한다. 세부 음원 종류에 따른 대사 프로파일의 변화는 각 그룹별로 특징적이면서도 상호간에 잘 구분되는 특징을 보였다. 이는 음악의 요소인 리듬,

선율, 그리고 원곡(화음)이 대사반응에 각각 다르게 영향을 미치며 신체의 대사반응은 이를 확실히 구분할 수 있다는 것을 의미한다. 뿐만 아니라 대사반응이 리듬, 선율의 각 군에서 보다 리듬+선율군에서 원곡과 더 가까운 쪽으로 이동한 것은 음악의 요소들이 대사반응에 미치는 영향은 요소별로 additive effect 를 가진다는 것을 보여준다. 또한 리듬+선율군과 원곡 간의 두 군의 비교에서는 대사반응의 차이가 유의하지 않았다는 것도 이를 뒷받침한다고 생각된다. 결과적으로 다양한 음악적 요소가 대사에 미치는 영향이 상이하므로 리듬, 선율과 화음을 모두 포함하는 원곡을 들었을 때 대사적 영향이 극대화될 것으로 생각된다.

스트레스에 의한 대사반응에 가장 큰 영향을 미친 원곡군에서 어떠한 대사변화가 나타났는지 대사체 수준에서도 확인하였다. 무음군과 correlation 이 높은 대사체는 glycine, hippurate, succinate 등이 확인되었고 원곡군에서 correlation 이 높은 대사체는 taurine, alanine, thymidine, urea 등이 확인되었다. Glycine 은 척수와 뇌관에서는 glycine receptor 에 작용하는 억제성 신경전달물질이나 뇌 신경세포의 NMDA receptor 에서는 glutamate 와 공동으로 작용하는 흥분성 신경전달물질이다.[12] 쥐에 glycine 을 과량 경구투여했을 때 과흥분상태에서 쥐가 사망했다는 보고는 glycine 에 의한 신경세포 흥분을 직접적으로 보여준다. 무음군에서 스트레스로 인한 glycine 증가는 뇌간에서는 억제 작용으로 신체 항상성의 균형을 깨고 대뇌에서는 신경세포의 과도한 흥분을 유도해 긴장 상태를 유지하게 한다고 생각된다. 원곡군에서 glycine 이 감소한 것은 이러한 중추신경계의 변동이 완화되었음을 의미하는 것으로 생각된다. Hippurate 는 urine 에서 발견되는 대표적 대사체 중의 하나로 장균총에 의해 생성되는 유기산의 배출형태이다. 장내 세균에 의해 생성되는 benzoic acid 는 장균총의 불균형을 측정하는 지표로 사용되며 hippurate 로 배출된다. 무음군에서 hippurate 가 증가한 것은 유발한 스트레스로 인해 장균총에 의한 장내 대사가 원활하지 못하였을 가능성을 제시하는 것으로 보여진다. 원곡군에서 이러한 유기산이 감소한 것은 스트레스에 의한 대사변화가 상쇄되었을 가능성이 있는 것으로 여겨진다. 원곡군에서는 항산화 작용을 하는 taurine 이 증가되었으며 alanine, thymidine, urea 등이 증가하여 신진대사 증가의 가능성을 관찰 할 수 있었다.

무음군에서 특징적으로 확인된 glycine 은 대표적인 neurotransmitter 이므로 음악이 brain 의 활성도에 미치는 영향을 확인하였다. fMRI 로 brain connectivity 를 측정하였을 때 무음군에서 원곡이군 대비 brain 활성도가 현저히 감소되어 있는 것을 확인하였다. 무음군에서 확인된 glycine 에 의해 흥분성 신경이 자극되어 긴장 상태가 유지되므로 뇌의 신경 network 는 오히려 활성도를 잃는 결과를 얻었다. 이는 극도의 긴장 상태에서 전체적이고 복합적인 사고를 하기 어려운 것과 같다고 생각된다. 그러나 음원군에서는 이러한 대사변화가 반전되어 신경 전달이 활발하게 유지되는 것을 관찰하였다.

이러한 결과는 음악의 요소 변화가 크지 않고 안정적인 구조를 가진 모차르트 음악이 진정적인 효과를 가져오며, 이러한 효과는 음악을 구성하는 여러 요소가 통합적으로 작용할 때 증가함을 제시하는 것이라 생각된다. 이러한 정서적인 영향이 뇌의 대사를 변화시키고 스트레스와 같은 신체의 불균형 상태를 완화시키는 결과로 나타났다고 생각된다. 모차르트의 음악과 비틀즈 혹은 뉴에이지 음악과의 비교에서 모차르트 음악이 더 좋은 효과를 보인 것을 고려할 때 [8, 11] 이러한 생리적 변화들은 일반적인 음악이라기 보다는 모차르트 음악의 효과라는 추론도 가능할 것이고 이에 대해서는 추후 더 연구가 필요할 것이다. 결론적으로 말하면 모차르트 음악에 대한 정서적인 반응이 뇌에 긴장완화와 활성도 증가를 야기하고 뇌의 이러한 반응은 스트레스 완화와 그에 따른 신진대사 변화로 이어진다고 할 수 있을 것이다.

References

1. S. Koelsch and W. A. Siebel, *Trends. Cogn. Sci.* **9**, 578 (2005).
2. V. Menon and D. J. Levitin, *Neuroimage* **28**, 175 (2005).
3. I. Peretz and M. Coltheart, *Nat. Neurosci.* **6**, 688 (2003).
4. P. N. Juslin and D. Vastfjall, *Behav. Brain. Sci.* **31**, 559 (2008).
5. J. T. W, C. Labbe and D. Grandjean, *Neuropsychologia* **96**, 96 (2017).
6. F. H. Rauscher, G. L. Shaw, and K. N. Ky, *Nature* **365**, 611 (1993).
7. M. Bodner, L. T. Muftuler, O. Nalcioglu, and G. L. Shaw, *Neurol. Res.* **23**, 683 (2001).
8. L. C. Gruhlke, M. C. Patricio, and D. M. Moreira, *Acta. Cardiol.* **70**, 703 (2015).
9. D. E. Brackney and J. L. Brooks, *J. Sch. Nurs.* **34**, 28 (2018).
10. M. B. Zimmermann, K. Diers, L. Strunz, N. Scherbaum, and C. Mette, *Front. Psychol.* **10**, 1104 (2019).
11. J. C. Smith and C. A. Joyce, *J. Music Ther.* **41**, 215 (2004).
12. F. Zafra, I. Ibanez, D. Bartolome-Martin, D. Piniella, M. Arribas-Blazquez, and C. Gimenez, *Adv. Neurobiol.* **16**, 55 (2017).